Total Absorption Spectroscopy of Mo-106 and Tc-106

A Dissertation Presented for the

Doctor of Philosophy

Degree

The University of Tennessee, Knoxville

Michael Paul Cooper

May 2023

This PhD is dedicated to my father, Kenneth Cooper, who always believed in me and encouraged me to give it my all.

Acknowledgments

I would like to thank God and my family for all of the help and support I've been given during my time at UT. I would like to thank Dr. Grzywacz for his mentoring and thoroughness, encouraging me to be a better researcher than I was prior to working for him. I would like to thank the staff at ORNL who answered questions, in particular, Dr. Peng Shuai, for his encouragement to pursue a GPU based approach. I've had many professors throughout my 11 years at UT who have provided valuable instruction and support, which I'm thankful for. A special thank you to Drs. Skutnik and Heilbronn, who have helped me throughout my time at UT, through multiple classes, thoughtful questions and answers sessions, and sometimes life advice in general.

Abstract

Total absorption spectroscopy is a method of gamma-ray spectroscopy that has gained prominence in the past several decades, as nuclear data revisions are performed on older nuclear data, which is often incomplete. A strong understanding of underlying nuclear data, particularly fission and beta decay data, is essential for nuclear reactors and nuclear fuel decay heat. This PhD work involves the analysis of fission fragments ^{106}Mo [Mo-106] and ^{106}Tc [Tc-106]. These neutron rich isotopes contribute upwards of 6% of the cumulative fission yield of ^{241}Pu [Pu-241] fission, and 4% of ^{239}Pu [Pu-239] fission. Prior data for these two fission fragments only encompassed a fraction of the Q value energy, causing uncertainty as to the impact of these isotopes on nuclear decay heating within nuclear reactor fuel. Experiments were conducted at Argonne National Laboratory using the Modular Total Absorption Spectrometer in 2019-2020 yielding decay data for these isotopes. This data was analyzed, with key nuclear physics parameters determined. The analysis consists of spectral deconvolution using the Expectation-Maximization method deployed on GPU processors. The deconvolution process determined the beta feeding intensities which are used to construct updated decay schemes. The updated beta feeding intensities are used to determine the log-ft values, nuclear matrix elements, and calculated beta energy spectra. Comparisons to literature sources were conducted. In the case of ^{106}Mo [Mo-106], comparison to theory has good agreement with an oblate deformation shape. ^{106}Tc [Tc-106] has been compared to previous work by Algora et al, and is in strong agreement for total gamma and beta energies well within uncertainty. Updated decay schemes were used to determine the impacts to nuclear fuel decay heat using the ORNL SCALE code.

Table of Contents

Chapter 1

Overview of Research Relevance

The study of beta decay properties of fission fragments of actinide nuclei is an area of research that is important to nuclear physics and nuclear energy applications. From a nuclear energy perspective, these nuclei help determine nuclear fuel decay heat. Because of the inherent experimental difficulties, the nuclear decay data for fission fragments is often incomplete. The two isotopes that are the focus of this research are ^{106}Mo and ^{106}Tc. These two isotopes contribute a significant amount of decay heat for nuclear fuel in the 0 to 100 second time scale post shutdown, and the data for both of these isotopes is deemed incomplete [1, 2]. The cumulative fission yields for these isotopes are significant, with values as high as 6.04% for e.g. ^{241}Pu. The cumulative fission yields for ^{106}Mo and ^{106}Tc are shown in table 1.1. Both isotopes have Q values significantly higher than their currently known highest populated levels in their daughter nuclei. Known decay schemes were constructed based on the data from high energy resolution gamma-ray measurements.

Previous studies for these isotopes used high energy resolution spectroscopy to determine the gamma ray energies and nuclear levels. However, this method suffers from the high degree of fragmentation of deexcitation patterns which results from high level densities. This is known as the pandemonium effect [3]. Total absorption spectroscopy (TAS) methods were developed in the 1970s to be capable of reconstructing beta feeding intensities and also

Table 1.1: This table lists the cumulative fission yields for ^{106}Mo and ^{106}Tc. The difference for fast versus thermal neutron induced fission is small with the exception of ^{238}U. The highest percent yields occur from the heavier mass plutonium isotopes.

Cumulative Fission Yields				
Fission Source	^{106}Mo Thermal	^{106}Mo Fast	^{106}Tc Thermal	^{106}Tc Fast
U-235	0.38%	0.43%	0.41%	0.47%
U-238	0	2.30%	0	2.52%
Pu-239	1.92%	2.01%	3.89%	3.94%
Pu-241	4.25%	4.48%	5.84%	6.04%

implemented to study neutron rich nuclei [4, 5]. TAS measurements have greatly improved over the past 50 years, and these improvements involved improved detectors, and more evolved detector simulations and data analysis methods. This research uses the TAS method to investigate properties of ^{106}Mo and ^{106}Tc decay. The device used to obtain nuclear decay data on ^{106}Mo and ^{106}Tc is the Modular Total Absorption Spectrometer (MTAS). MTAS has a very high gamma ray detection efficiency, and is segmented to allow for more insight to nuclear gamma ray cascade properties. MTAS will be discussed in further detail in a later section. To produce sufficient quantities of pure ^{106}Mo and ^{106}Tc isotope beams, the CARIBU facility at Argonne National Laboratory (ANL) was chosen [6]. The CARIBU facility uses a ^{252}Cf fission source to produce and extract separated isotopes of interest.

Using the data obtained with MTAS from ANL, the goal of this research is to deduce the beta feeding intensities for levels in ^{106}Mo and ^{106}Tc daughter nuclei, as well as analyzing their impact to decay heat and associated anti-neutrino spectra. This data deconvolution is being performed with the Expectation-Maximization (EM) method, and coded with PyOpenCL for GPU processing [7]. Before performing the deconvolution procedure using the EM method, the data must first be unpacked and sorted which is done with the Pixie Acquisition and Analysis Software Suite (PAASS) framework, and exported to ROOT. Then, the data must be cleaned of contaminants, and potential new levels identified. Once the beta feeding and gamma ray intensities are obtained, this information is then going to be included into a local version of the Oak Ridge National Laboratory (ORNL) SCALE reactor physics code to determine the impacts to decay heat [8].

Chapter 2

Current State of Nuclear Data for ^{106}Mo and ^{106}Tc

A significant portion of nuclear data for fission products is incomplete, and experiments were often performed before TAS measurements were implemented. As a result, many of the nuclear engineering and physics codes such as MCNP and SCALE are using data which is incomplete and potentially incorrect. The applications that these codes have range from reactor decay heat to stockpile stewardship, highlighting the importance of quality input data.

When a nucleus undergoes fission, it usually splits into two dissimilar sized fragments. The isotopic fission distributions are broad as shown in figure 2.1, which uses ^{239}Pu as a representative example. ^{239}Pu fission fragments are predominately neutron rich mid-shell nuclei, which are often very deformed. These fragments usually decay through beta decay, often populating excited neutron bound or unbound nuclear states. The decay energy is shared between the kinetic energy of the electron and antineutrino, and the excitation energy of the daughter nucleus. The population of the excited states present in the daughter nucleus can be reconstructed using gamma and neutron energy measurements using nuclear

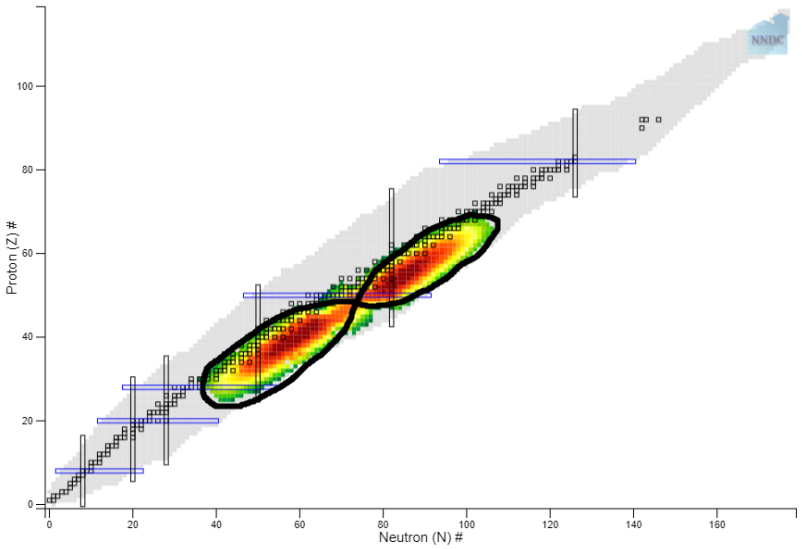

(a) ^{239}Pu fission fragment distribution.

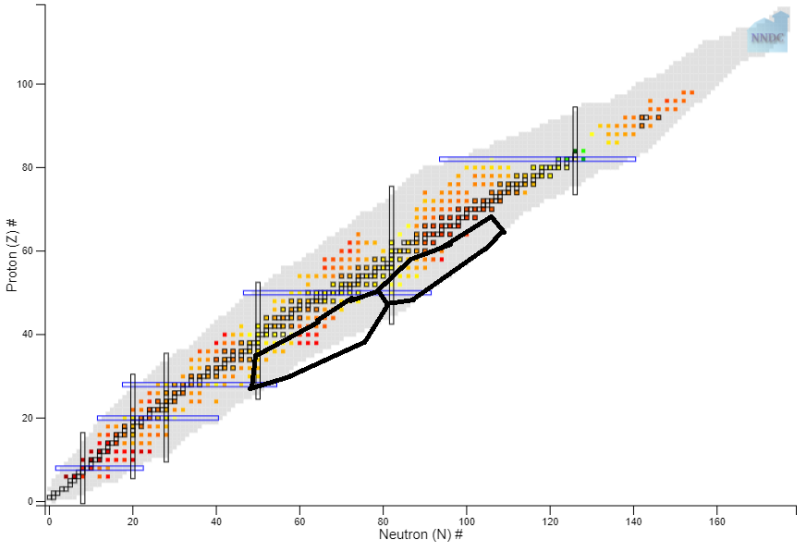

(b) Quadrupole deformation (β_2) values.

Figure 2.1: (a) This subfigure shows the fractional fission yield of ^{239}Pu. As is typical in asymetric fission, there are two dissimilar mass peaks, with mass distributions around these peaks. (b) This subfigure shows the quadrupole deformation parameter β_2. Fission fragments are often highly deformed.

spectroscopy.

The isotopes which are being studied as the focus of this PhD research are ^{106}Mo and ^{106}Tc. The necessity to study these isotopes is due to the incompleteness of the NNDC data for them, as well as their impact on reactor decay heat [9, 10, 11, 12]. Figures 2.2 and 2.3 show the current decay schemes constructed based on high resolution data for ^{106}Mo and ^{106}Tc, respectively. The decay schemes for ^{106}Mo and ^{106}Tc have the highest beta-fed levels assigned far below the Q_β value, and it is noted in the ENSDF file for ^{106}Mo that it is likely incomplete. The presence of a large gap between the Q_β value and the highest known nuclear level implies that there is missing data, as this energy region would be highly susceptible to the pandemonium effect. These high energy states are weakly fed, and therefore easy to miss for high energy resolution, low efficiency, spectroscopy measurements.

Previous ^{106}Mo data came from Jokinen et al and was obtained at the University of Jyvaskyla, Finland using the IGISOL separation method [9, 13]. That data was produced using proton-induced fission of ^{238}U and online mass separation. For gamma ray detection, both arrangements used HPGe detectors. Their first setup used pulsed proton beams to impact the uranium target, allowing for control of the long lived activities produced along the same mass chain. This seteup was used to identify gamma-ray transitions and half-lives. The second setup used a continuous beam, and used the transport tape to remove long-lived activities. The second setup aimed to measure the full energy of the coincident beta particles using a ΔE-E telescope, and collect gamma-gamma coincidences. The results of this experiment were assigned level spin parities of 1^+ for the majority of excited states, and 2^+ for the ground state of ^{106}Tc. The reasoning of a 2^+ ground state of ^{106}Tc was based on the difference in total betas detected minus betas that fed to excited states from the 0^+ ground state of even-even ^{106}Mo. The ground state was observed to have negligible feeding [9].

Previous ^{106}Tc data came from Summerer et al and were obtained at the University of Mainz, Germany. That data was produced using the ^{239}Pu (n,f) reaction, with thermal neutrons coming from a TRIGA reactor at Mainz. The fission products were separated online with solvent extraction and centrifuges. Ge(Li) detectors were used to detect gamma and gamma-gamma coincidences during the 40 hour run. The technetium isotopes were mixed. The isotopic identification of gamma rays was achieved through the data analysis, with the analysis requiring the use of coincidence gating of prominent known characteristic gamma ray transitions to separate the isotopes. The results of this experiment produced a level scheme for ^{106}Tc using gamma intensity budgets, along with I^{π} assignments partially based on analogy to other ruthenium isotopes. The analysis performed assumed no ground state feeding, and that the level scheme would be similar to the states in ^{104}Ru and ^{102}Ru. For calculating logft values, they use $Q_{\beta} = 6950$ keV, which is larger than the current ENSDF value of 6547 keV [11]. This is shown in figures 2.2 and 2.3.

From an engineering application perspective, the decay of fission fragments results in about 7% of total reactor power. There are many isotopes contributing to this energy release known as decay heat, with their contributions based on the isotopic yields from fission and their decay energies. A large decay energy may not matter if the total yield for an isotope is negligible. However, ^{106}Mo and ^{106}Tc have non-negligible fission yields, and both have large Q values. ^{106}Mo accounts for 0.1% of decay heat of nuclear fuel at shutdown, and 0.2% of decay heat during reactor operations, and ^{106}Tc accounts for roughly 1% of decay heat both during operations and immediately after shutdown. These values were calculated using SCALE 6.2 with current NNDC data, to scope the impact of ^{106}Mo and ^{106}Tc on decay heat. The specifics of these calculations will be described in a later section dedicated to SCALE calculations and analysis.

Of particular note is the distinction between gamma and beta decay energy. If feeding is shifted from low lying states to higher energy states, then the decay heat will shift from beta

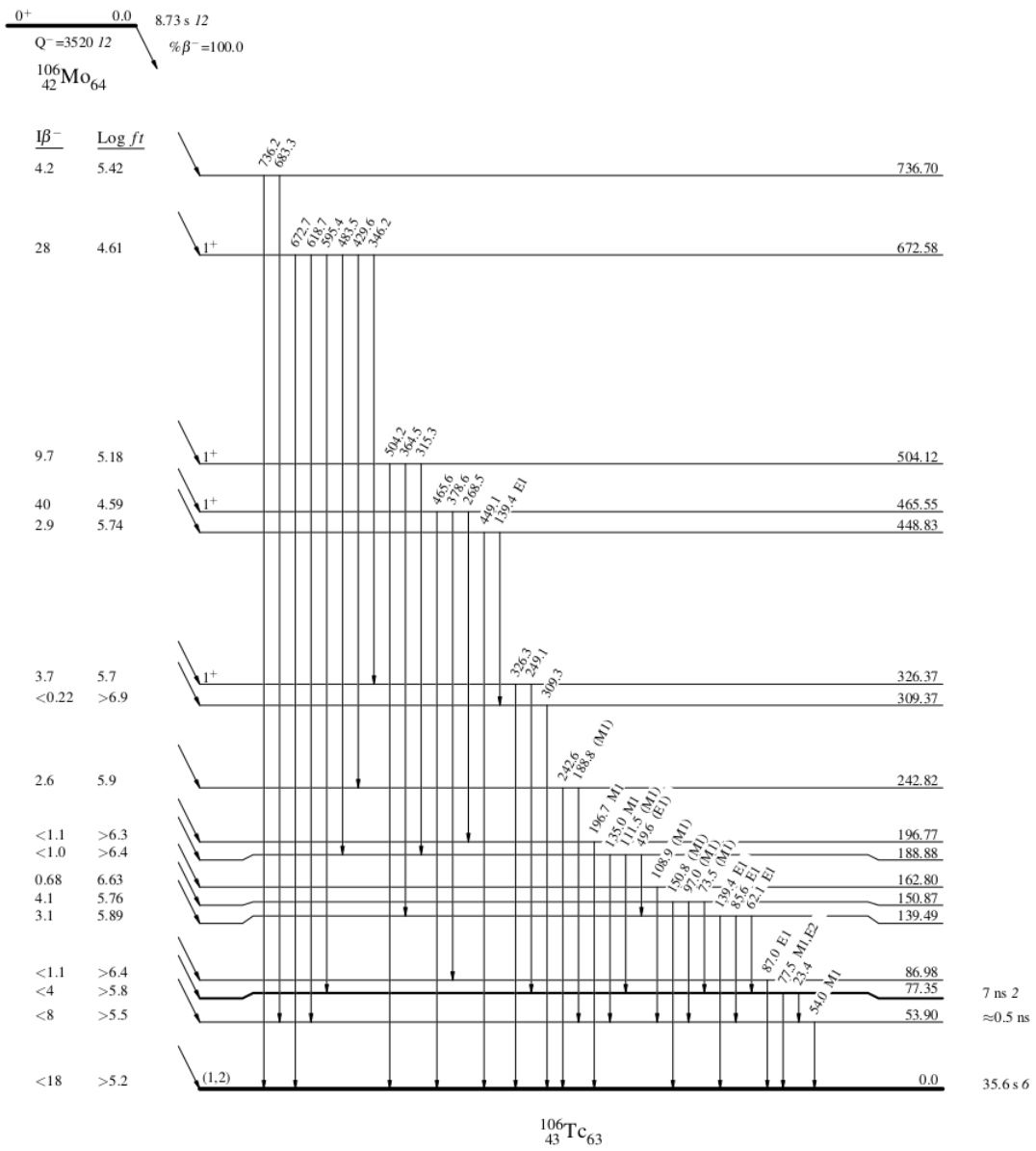

Figure 2.2: This figure shows the current ^{106}Mo decay scheme from the ENSDF archive [9, 12]. The current highest known level is 736.7 KeV, far below the Q_β value of 3520 KeV.

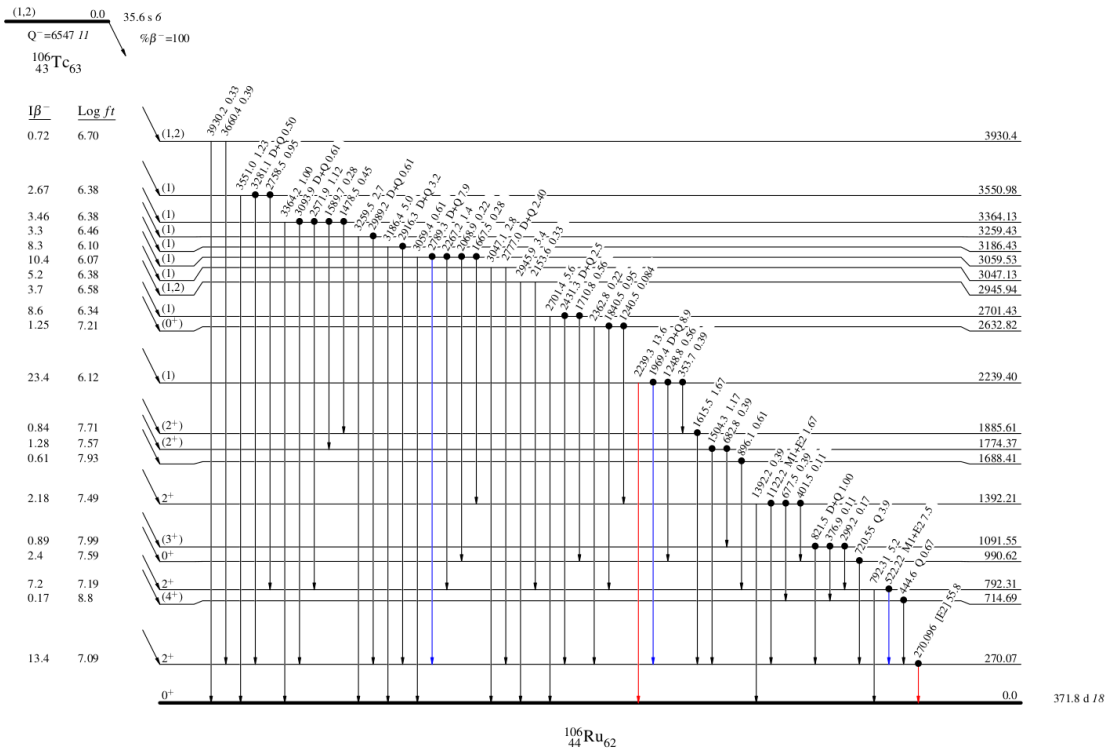

Figure 2.3: This figure shows the current ^{106}Tc decay scheme from the ENSDF archive [11, 10]. The current highest known level is 3930 KeV, which is more than 2 MeV below the Q_β value of 6547 KeV.

heating to gamma heating. This is important for nuclear fuel, as beta particles will mostly heat the fuel rod centerline, whereas gamma rays will penetrate fuel rods and surrounding water further. An example of this effect is shown in figure 2.1 for ^{84}Br, ^{85}Br and ^{86}Br, which comes from previous MTAS work performed by Goetz [14]. For this particular set of isotopes, average gamma ray energy increased by a significant amount.

Table 2.1: This table shows the percent of β feeding to levels above 1.7 MeV for ^{84}Br, ^{85}Br and ^{86}Br, for both experimental work by Goetz, and former ENSDF values. It can be seen that the average gamma ray energy increases [14].

Isotope	Experiment (%)	ENSDF (%)	Δ(%)
^{84}Br	62.29	54.55	+7.74
^{85}Br	4.95	2.76	+2.19
^{86}Br	75.53	73.34	+2.19

Chapter 3

Beta Decay of Neutron Rich Nuclei Using High Resolution and Total Absorption Gamma Spectroscopy

Gamma ray spectroscopy involves the measurement of photon energy deposited in media such as scintillator or semiconductor detectors. MTAS is a large segmented NaI(Tl) scintillator detector. Scintillator detectors work on the principle that certain materials when exposed to radiation will emit light of particular wavelengths. For an inorganic scintillator such as sodium iodide, the crystal's electrons are elevated to the conduction band, which is located several eV above the valence band, when exposed to radiation. This is shown schematically in figure 3.1 from the textbook by N. Tsoulfanidis [15]. The electron/hole pairs created will then travel to the activator material, which is thallium in the case of NaI(Tl). The electrons deexcite, releasing light. For a NaI(Tl) detector, this light is around 410 nm in wavelength. An appropriate photomultiplier is matched to the NaI(Tl) detector to ensure maximum efficiency. The light emission and subsequent electrical signal is proportional to the energy of the incoming gamma ray, and can therefore be used for spectroscopy. Typically sodium iodides have inferior resolution compared to semi-conductor detectors and some other scintillators, however, they can be made into large crystals that have high

counting efficiency. Scintillators generally will require more energy to create signals than semi-conductors, there will be non-uniformity in light deposition on the PMT, as well as non-uniformities in the crystal and PMT themselves [16]. For more about the physics of scintillator resolution, the reader is encouraged to review the paper by Morton et al. These For a more in depth description of scintillator materials, the reader is encouraged to review the excellent textbooks by Knoll and Tsoulfanidis [17, 15].

Gamma ray spectroscopy is a key technique for obtaining information about nuclear excited states. Most neutron rich nuclei, including fission fragments, decay via β^- emission. This β decay often does not go directly to the ground state of the daughter nucleus, and as such, a cascade of gamma rays from intermediate levels results. Much emphasis is placed on high energy resolution spectroscopy using detectors such as high purity germanium (HPGe) detectors. While having a high energy resolution, the efficiencies of detectors using this approach are usually low due to the relatively small crystal sizes. HPGe crystal sizes are typically on the order of 10s to 100s of cubic centimeters.

Most fission products have very complicated decay schemes. Typically the parent nucleus has a large beta decay energy (Q_β), allowing for many excited states in the daughter nucleus to be populated. These intermediate levels in the daughter nucleus will decay through gamma ray cascades, making for a potentially complex total decay scheme. Many of these high energy gammas will have low intensity, which can result in low detection efficiency instruments missing them. At higher excitation energies, nuclear level densities increase, resulting in a further fragmentation of level population and decay cascade patterns. This means that a significant amount (if not the majority) of the gamma-ray decay energy would be missed by using solely high resolution spectroscopy. This is well documented as the "pandemonium effect" in Hardy's work from 1977 [3]. Figure 2.3 shows an example of a nucleus, ^{106}Tc studied in this work, which has this type of decay scheme.

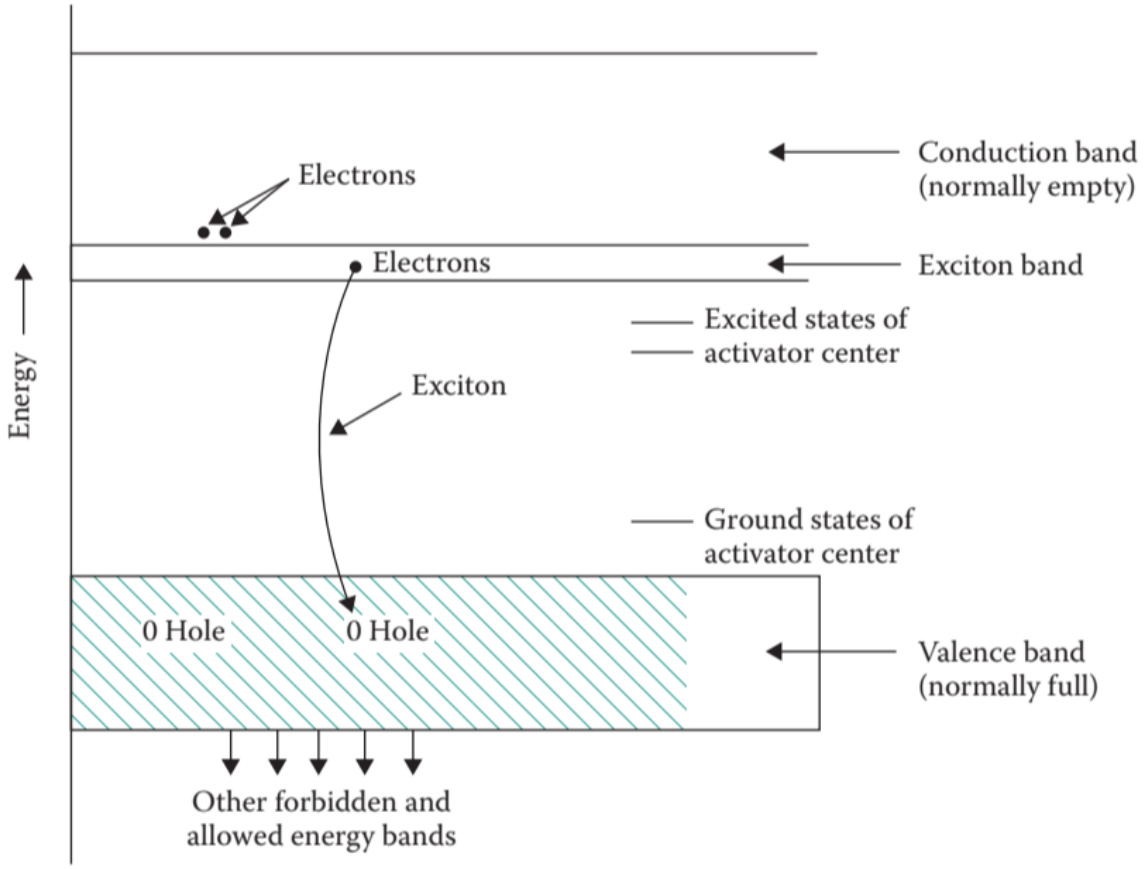

Figure 3.1: Allowed and forbidden energy bands of inorganic scintillator crystal [15].

One method of handling this fragmentation of levels, and determining the low intensity feedings to these levels, is by using what is termed Total Absorption Spectroscopy (TAS). TAS involves attempting to capture as much of the emitted radiation as possible. In this sense, it can be compared to a calorimeter. By summing up all of the emitted gamma-ray radiation, it is possible to determine the nuclear level which was fed.

Typically, TAS detectors aim for a high solid angle coverage. This can be accomplished by bringing the sample inside the detector, providing near 4π coverage. Another consideration is that the emitted gamma-rays should completely interact inside the detector, producing a full photopeak. This can be accomplished by using detector volumes that are large and thick, ensuring high total efficiency and minimal escape radiation.

It will be discussed later how segmenting TAS detectors provides additional insight into nuclear level schemes and structure.

Chapter 4

Experimental Methods

This section will discuss the experimental methods employed to determine the beta feeding of ^{106}Mo and ^{106}Tc. Data for these isotopes was gathered during the late February - early March 2020 campaign at Argonne National Laboratory (ANL).

4.1 Modular Total Absorption Spectrometer (MTAS)

MTAS is a segmented sodium iodide (NaI) detector, which is operated by Oak Ridge National Laboratory, in collaboration with the University of Tennessee, Louisiana State University, and the University of Warsaw. MTAS is capable of measurements which can establish excitation energies of levels populated in beta decay. MTAS has a total detection efficiency of over 75% for up to 3 MeV gamma rays, and over 98% efficiency for partial energy deposition [18, 19]. This efficiency curve is shown in figure 4.1. A picture of MTAS at Argonne National Laboratory is shown in 4.2.

MTAS is divided into a center module, and 3 "rings" of detectors. Each ring is composed of 6 hexagonal NaI bars, with photomultipliers on each end. The center module has 6 PMTs on each end, and a hole through the middle to bring the source into MTAS. This is illustrated

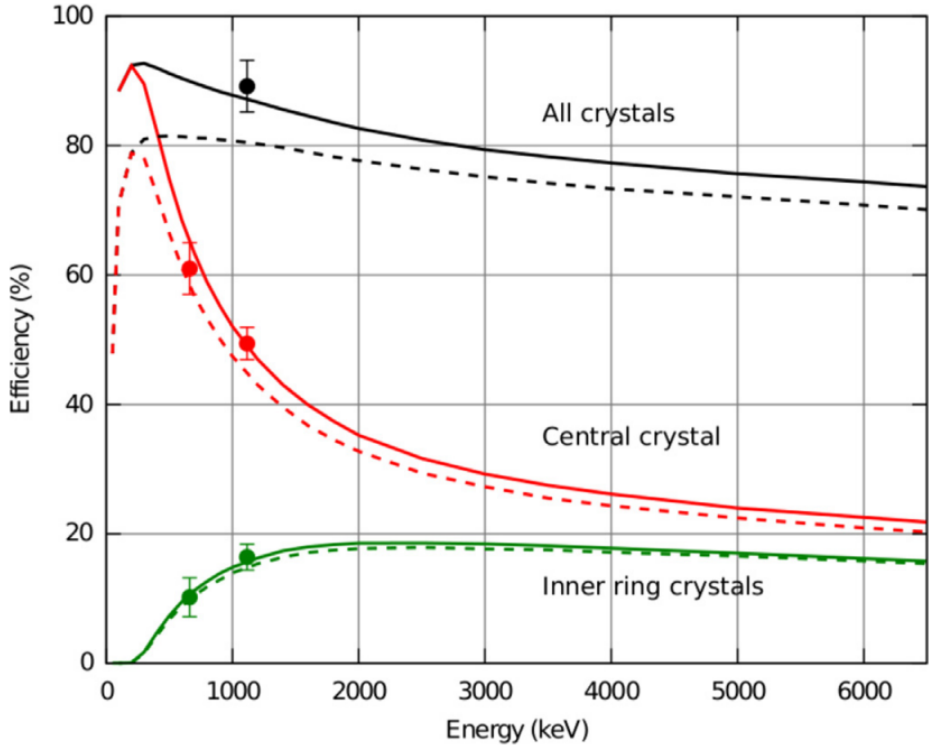

Figure 4.1: Figure showing MTAS's detection efficiencies for a range of energies. Solid lines are without auxillary detectors; dashed are with auxillary detectors. For this figure, lines are from GEANT4 simulation, and experimental data points are marked with error bars. The efficiencies for all modules, only center, and only inner are shown [19].

Figure 4.2: Picture of MTAS at Argonne National Laboratory. MTAS is located behind the yellow lead shielding blankets. In the front of the picture on aluminum framing is the Moving Tape Collector (MTC). To the right of the MTC are the switchboard and Pixie digitization modules, along with other NIM modules. Below the MTC a roughing pump can be seen, which along with the turbo pump mounted at the MTC, ensure that the MTAS center tube is operating in vacuum.

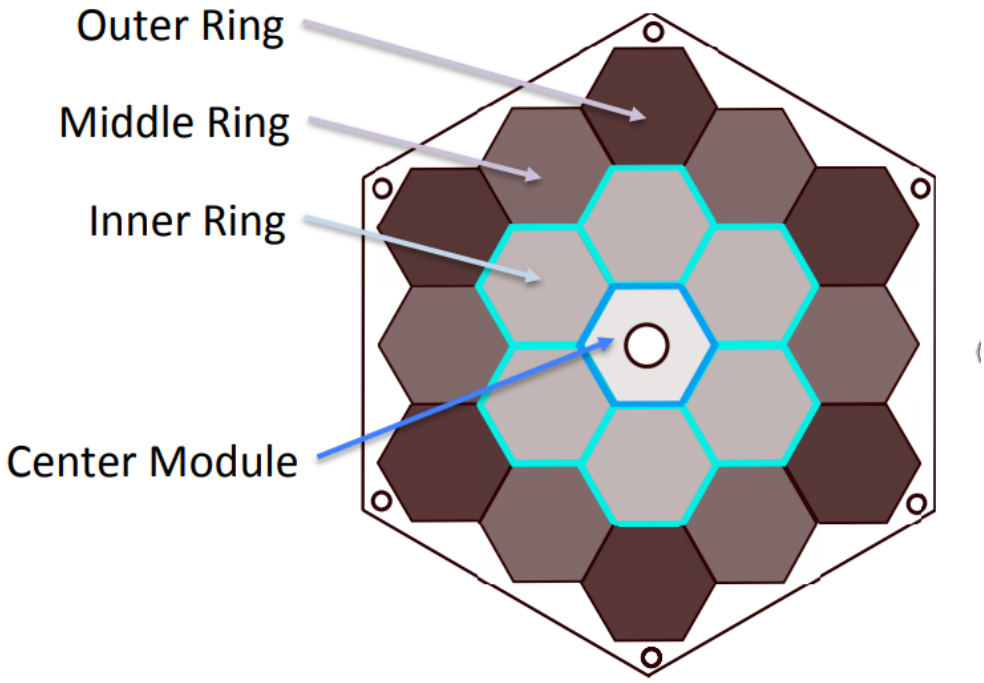

Figure 4.3: Figure showing the ring structure and segmentation of MTAS [18, 20]. The perpendicular distance to center determines which ring the module belongs to. The cavity within the central module is visible.

in Figure 4.3. In total, MTAS currently has 48 PMTs.

It is possible to determine the properties of gamma cascades de-exciting β-fed levels by utilizing MTAS's segmentation. In the case of ^{106}Tc, the 2239 KeV sum peak is interpreted as a level in the total MTAS spectra, which is obtained by summing all MTAS modules. The 270 KeV gamma-ray corresponding to the 270 keV level that the 2239 KeV level decays to will show up in the central spectra, but will be greatly reduced in the total spectra, since it would be included with the 2239 KeV sum peak. The central spectra and total sum spectra are shown in figures 4.4 and 4.5. By creating a 2D histogram comprised of central vs total histograms, it is possible to assign gamma rays to a specific β-fed level. This is shown in figure 4.6. The horizontal lines are individual gammas which belong to the level that they intersect on the y axis.

MTAS is equipped with 2 internal silicon detectors, each having 7 strips of silicon. These silicon strips provide 96% solid angle coverage, along with a 90% trigger efficiency, allowing for beta particle coincidence gating of the NaI gamma spectra, strongly reducing background counts [19]. These silicon strips also allow for making sure that a radioactive spot on the collection tape is properly centered in MTAS for measurement.

When conducting experiments at radioactive beamline facilities, one of the challenges is how to get the radioactive ions into the measurement device. At ISOL facilities such as CARIBU and ISOLDE, it is typical to implant the beam onto a tape transport system. MTAS is designed to allow a collection tape to be moved into and out of the device through a cavity which runs through the central module in vacuum. This Moving Tape Collector (MTC) was constructed at LSU for the MTAS collaboration. The MTC is shown schematically in figure 4.7. By utilizing the tape drive to pull the ion deposition point on the tape into MTAS, this allows for near 4π geometric efficiency. In addition, the tape drive provides the ability to control the implantation time on the tape, and control over

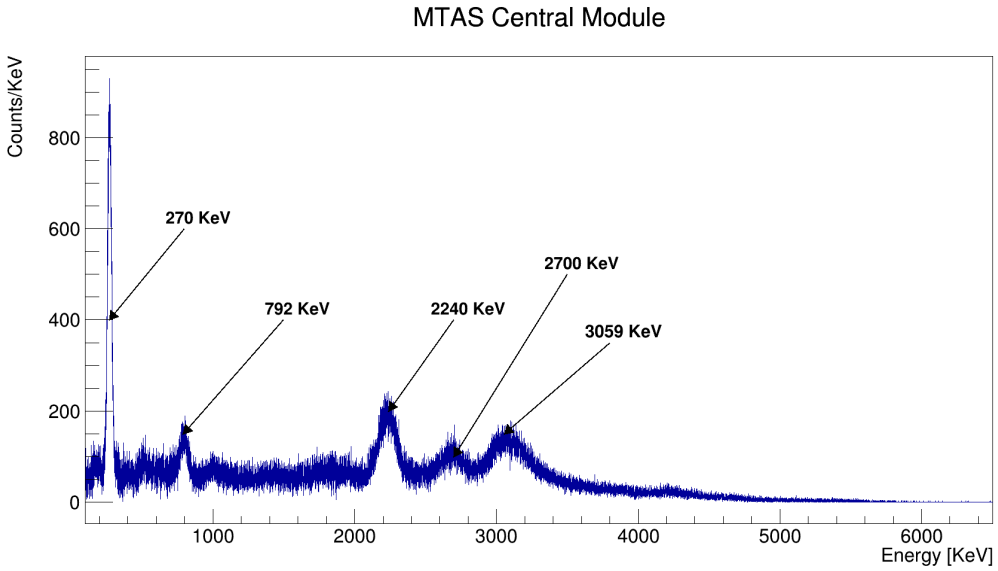

Figure 4.4: 1D histogram of the MTAS central codule. The 270 keV and 792 keV levels are visible, however the 2239 level among others have high enough energy to mostly escape the central module.

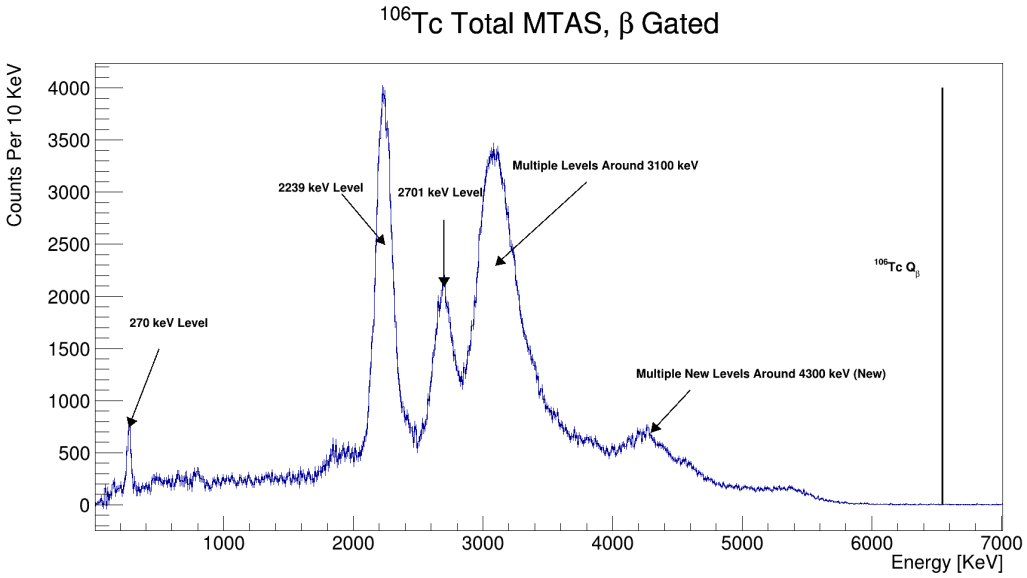

Figure 4.5: 1D histogram of the MTAS total sum gamma spectrum. In this figure the levels at 2239 keV, 2700 keV, and several around 3000 keV can be seen as summed photopeaks.

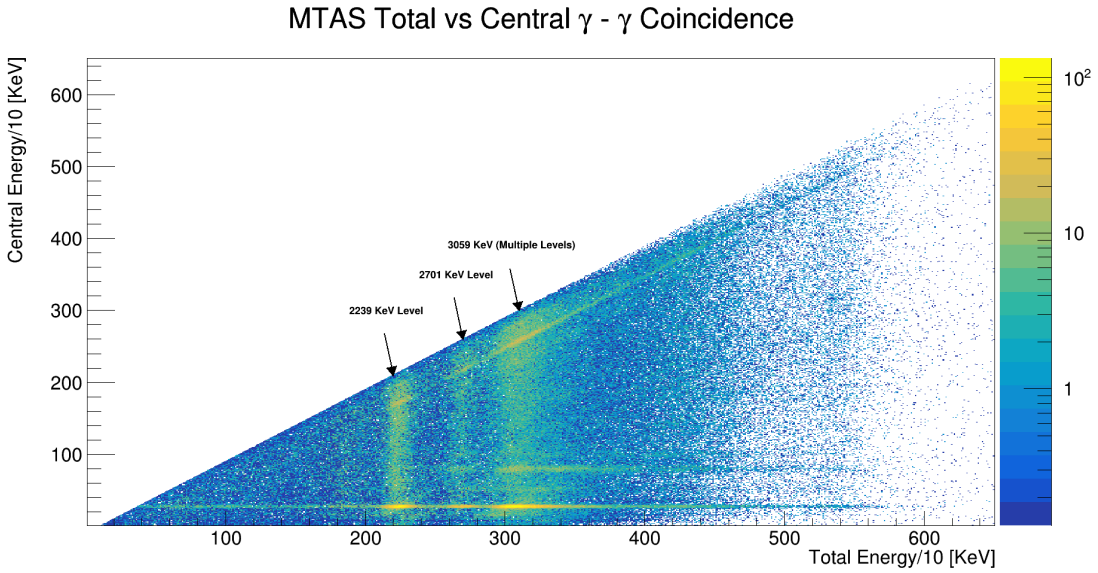

Figure 4.6: This figure shows a 2D $\gamma - \gamma$ coincidence histogram using experimental data with a beta gate. The intersection points of gammas along the y axis with the x axis indicate that the individual gamma ray from the y axis is part of the corresponding level on the x axis.

the amount of time the sample is inside of MTAS. This allows for discrimination of isotopes based on half-lives. For maximum source activity for a symmetric collect/measure cycle, one would usually collect on the tape about two times the desired isotope's half-life [21]. If it is desired to observe the daughter nucleus instead of the parent nucleus, then the tape drive can be set to allow the sample to remain in MTAS for greater than five times the parent isotope's half-life, such that the majority of decays will be from the daughter nucleus. This is a very powerful capability.

4.2 Data Digitization

Data output from MTAS, as well as all other detectors and logic signals, is digitized using XIA Pixie-16 modules, revision D. These modules feature onboard pulse shaping and discrimination using trapezoidal filters with adjustable parameters. The pulse trigger and shaping trapezoidal filters both feature adjustable rise time and flat top time, as well as thresholds. A picture of a Pixie-16 module is shown in 4.8 [22].

Pixie-16 modules can output digitized data into what is termed "list mode event data" using adjustable First In First Out (FIFO) settings. This list mode data can contain event ID numbers, raw energy sums, and timestamps, as well as other information. This output is well formatted, and can be parsed into appropriate C++ and ROOT structures using the UTK code PAASS, which will be discussed later.

4.3 CARIBU Functionality

Argonne National Laboratory is home to the Argonne Tandem Linac Accelerator System (ATLAS) facility, which houses the Californium Rare Isotope Breeder Upgrade (CARIBU) fission fragment source [6]. CARIBU is capable of generating a wide range of fission

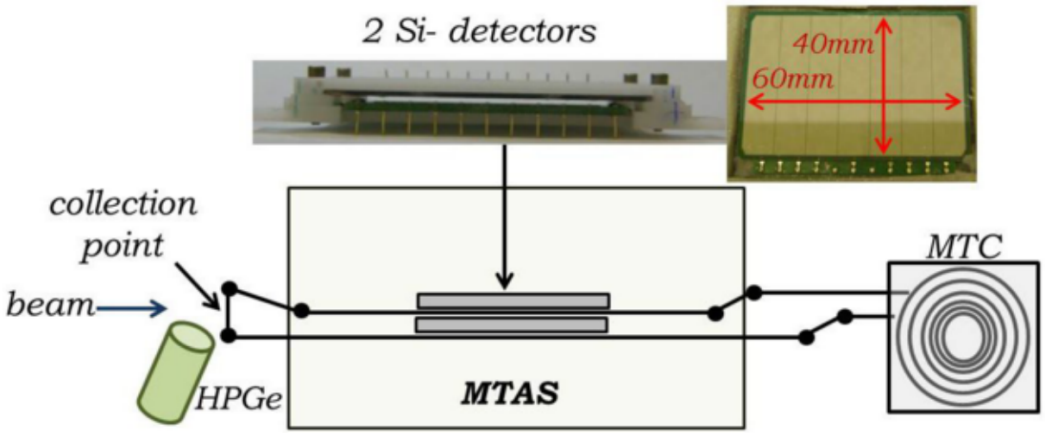

Figure 4.7: This figure shows a schematic of the tape drive used by MTAS. Note, the plastic implant detector would be located just behind the implant point. [24]

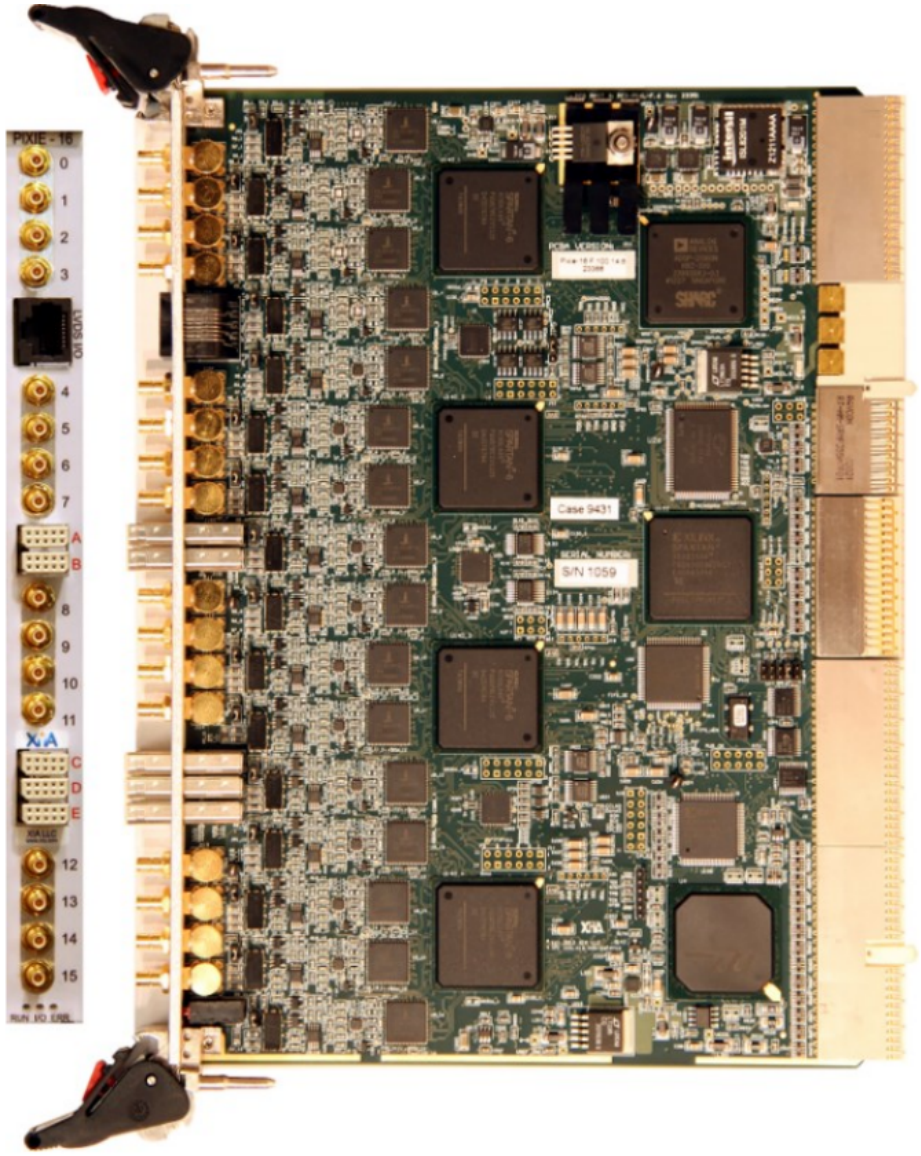

Figure 4.8: This photograph shows a Pixie-16 module, with all of the front and side view connections [22].

fragments, including the refractory elements and mass 106 chain. CARIBU works by allowing an approximately one curie ^{252}Cf source to decay in a helium gas catcher [6]. The fission fragments are transported to a radiofrequency cooler, which turns $\approx 50\%$ of the fragments into 1+ or 2+ ions in a beam with a very low energy spread. This beam can then be either sent to stations for low energy nuclear physics research, or injected into ATLAS accelerators. The beam can also be further purified with MRTOF. For the purpose of this research, the rates of unaccelerated ^{106}Mo and ^{106}Tc beams were considered acceptable for MTAS to measure [23]. The rates published by ANL were listed as $4.6 \cdot 10^4$ for ^{106}Mo, and $2.9 \cdot 10^4$ for ^{106}Tc. The rate for ^{106}Tc is slightly deceptive, as there will be decay of ^{106}Mo bolstering its rate if a mixed beam is used.

4.4 Experiment Preparation at ANL

Mass 106 measurements were carried out from February 21 to March 3, 2020, by a joint team consisting of members from ORNL, UT Knoxville, LSU, and Warsaw. To prepare for the experiment, the first step was to power up MTAS and gain match the photomultipliers. This is done by adjusting the voltage to MTAS module by module, such that naturally occuring 1461 KeV gamma rays are calibrated to the 1461 channel of Pixie output. This provides a rough linear calibration for online identification of ion beam components and contamination using known gammas. Offset adjustments sets the 0 channel to 0 keV.

The tape drive for MTAS, pictured in figure 4.2, was tested to ensure that it was working properly. The tape drive allows for implanting the ion beam onto a thin piece of tape, which is then pulled into MTAS, with timings controlled based on the decay properties of the nucleus being studied. Once the radioactive spot has been in the middle of MTAS for approximately five half-lives, it is then transported out of MTAS to a collection container. There are roughly 100 transports each of 3 feet of tape (300 feet total) which then recycles

unless the tape is changed out [21].

One of the newer implementations to the experimental set-up was the addition of the plastic implant detector directly behind the tape implantation spot at the front of MTAS. As the ion beam is electomagnetically guided, the plastic implant detector helps to determine if the beam is properly aligned to the entrance of MTAS. This consists of ANL using electrostatic deflectors to steer the beam, while trying to maximize detection rate on the plastic implant detector. The ion beam purity was high partly due to the multi-reflective time-of-flight system, however, because of the (β, n) branch of ^{106}Nb, there was contamination of mass 105 daughters on the order of 4.5%. The plastic implant detector also enables construction of beta-gamma coincidences for the HPGe detectors observing the implantation spot.

The next step was to prepare and calibrate the HPGe detectors monitoring the collected beam implant spot. The calibration was done with ^{60}Co and ^{137}Cs sources . The HPGe detectors assist with identification of contaminants, and can be beta gated with the plastic implant detector. When ions implanted onto the tape decay before being pulled into MTAS, the plastic implant detector will detect beta particles, and can be used as a gate, purifying the γ-spectra of the HPGe detectors.

^{106}Mo Experiment

For the ^{106}Mo experiment, the observed decay rate was $\approx$ 40 counts per second in the total MTAS spectrum, with a beta gate applied. Due to MTAS's very high efficiency (see fig 4.1), the true rate of ion implantation is close to the count rate of the total MTAS spectrum. Data was collected for 18 hours and 20 minutes, starting at 2:30 PM on February 28, and ending at 8:50 AM February 29. The tape cycle selected for ^{106}Mo was 16 seconds of implantation, 2 seconds of tape transport into MTAS, and 40 seconds of measurement. This was chosen to

maximize ^{106}Mo counts, while minimizing ^{106}Nb and ^{106}Tc counts, as they have half-lives of 1.02 seconds and 35.6 seconds, respectively, as shown in fig 4.9. The majority of the ^{106}Nb would have decayed away during transport and the first few seconds of measurement, and 40 seconds of measurement allows for only around one half-life of ^{106}Tc decays to grow in.

^{106}Tc Experiment

For the ^{106}Tc experiment, the MRTOF gate on mass 106 was widened, to allow for a mixed beam of ^{106}Mo and ^{106}Tc, since the ^{106}Mo would quickly decay to ^{106}Tc. The beam rate was considerably higher than the previous pure ^{106}Mo experiment, at $\approx$ 450 counts per second in the beta-gated total MTAS spectrum. Data was collected for 17 hours and 50 minutes, starting at 3:40 PM on February 29, and ending at 9:30 AM on March 1. The tape cycle selected for ^{106}Tc was 60 seconds of implantation, 2 seconds of tape transport, and 180 seconds of measurement. This tape cycle allows for the majority of ^{106}Mo to decay away, leaving only ^{106}Tc and her daughter nuclei. Both the ^{106}Tc and ^{106}Mo experiments went very smoothly, without any major interruptions.

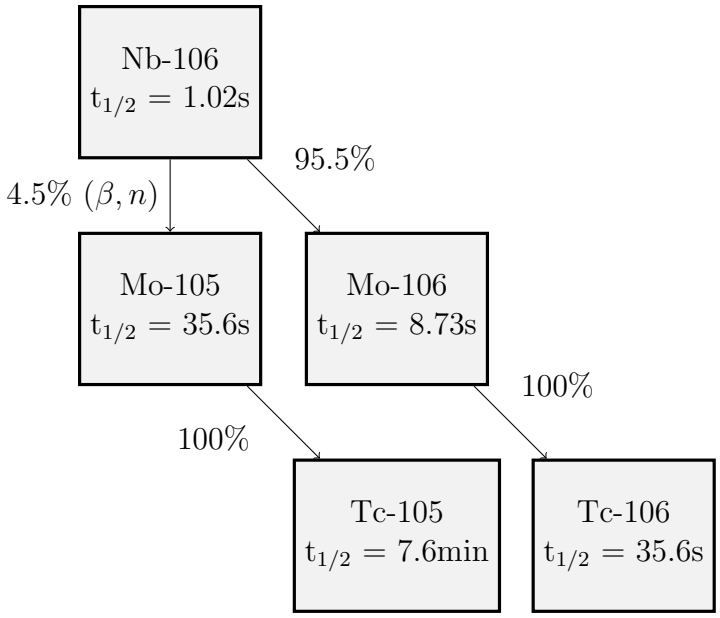

Figure 4.9: Schematic showing Nb-106 decay including the (β,n) branch.

Chapter 5

Data Analysis Methods

To extract information from the large quantity of data ($\sim$ 18 GB) that was collected at Argonne, multiple stages of data analysis methods were employed. The first was to convert the native data acquisition format from what are termed "large data files", or LDFs, into C++ data structures and histograms. This was done by using the PAASS code developed by the UT nuclear physics group. The code is modular, with the detector drivers and conversion from LDF format to C++ structures already having been implemented prior to this work [25]. A processor for MTAS data was written in C++ for PAASS, to sort the channel data into appropriate histograms. An older standalone MTAS processor existed and is still in some usage by the ORNL team, but it was incompatable with the more modern PAASS framework. An advantage of this update was the direct implementation of ROOT structures, allowing for easier manipulation of data.

5.1 MTAS Data Calibration

Originally, MTAS data was processed with the aforementioned C++ processor, turning the raw detector data into histograms. The MTAS data was sorted into its corresponding rings, and then calibrated using a linear interpolation scheme. MTAS was gain matched at the

experiment such that the bin numbers of energy spectra roughly correspond to keV per channel, but NaI is known to have a nonlinear response when used across a wide energy range, and as such, further calibration was required. This calibration used the 1461 KeV ^{40}K peak which is a common background peak present in nature. In addition to natural ^{40}K present in nature, multiple containers of KCl salt were placed around MTAS inside the lead shielding to produce a stronger ^{40}K source peak. The calibration also used either the 270 KeV ^{106}Tc peak, 465 KeV ^{106}Mo peak, or the ^{208}Tl 2614 KeV peak. Which second peak is used for the interpolation depends on whether the channel being calibrated is located in the center or outer rings of MTAS, as the 2614 KeV peak will not interact enough in the center module to use effectively.

The implemented method is follows the above method, but is implemented into ROOT. Minimally processed data is output into ROOT structures, and then calibrated and analyzed with PyROOT [26]. PyROOT allows for better management of statistics and plotting. The calibration process is the same for both methods.

A total MTAS histogram showcasing this energy calibration can be seen in figure 5.1 (a) (note that this subfigure is not beta gated).

5.1.1 Silicon Detectors

As mentioned before, MTAS is equipped with 14 silicon strip detectors for beta particle detection. These strips form nearly 4π detection, with 7 strips on top and 7 on bottom of the detector. The collection tape slides between the top and bottom of the detector, with minimal spacing. The silicon strips allow for the beta gating of the MTAS spectra, as well as positioning the implanted ions on tape in the center of MTAS. The data from the silicon strips in MTAS was treated with several processing methods, due to the silicons sometimes being noisy. Energy thresholds were placed at 700 and 30000 units (note that these units do

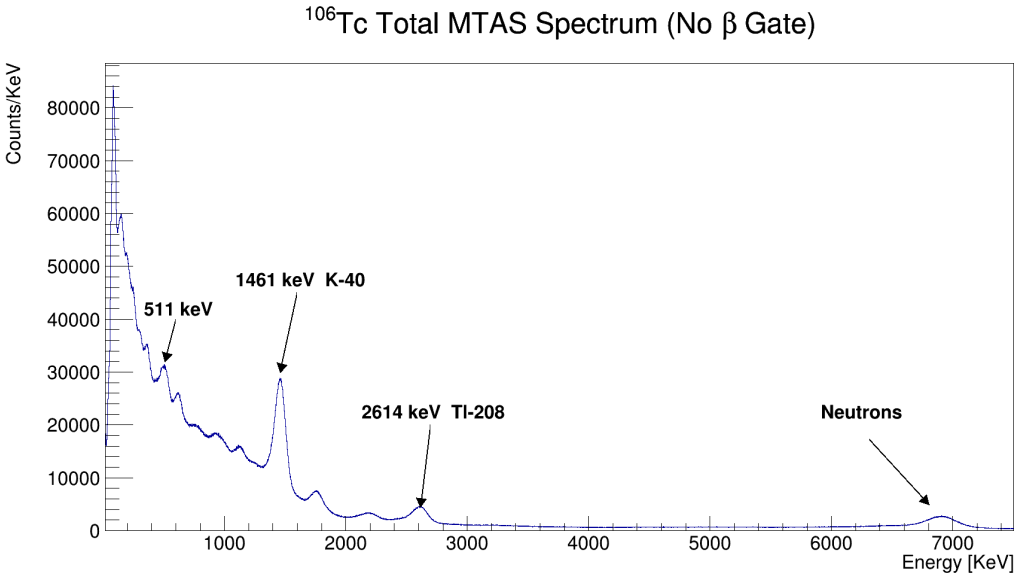

(a) Non-β-gated ^{106}Tc spectrum.

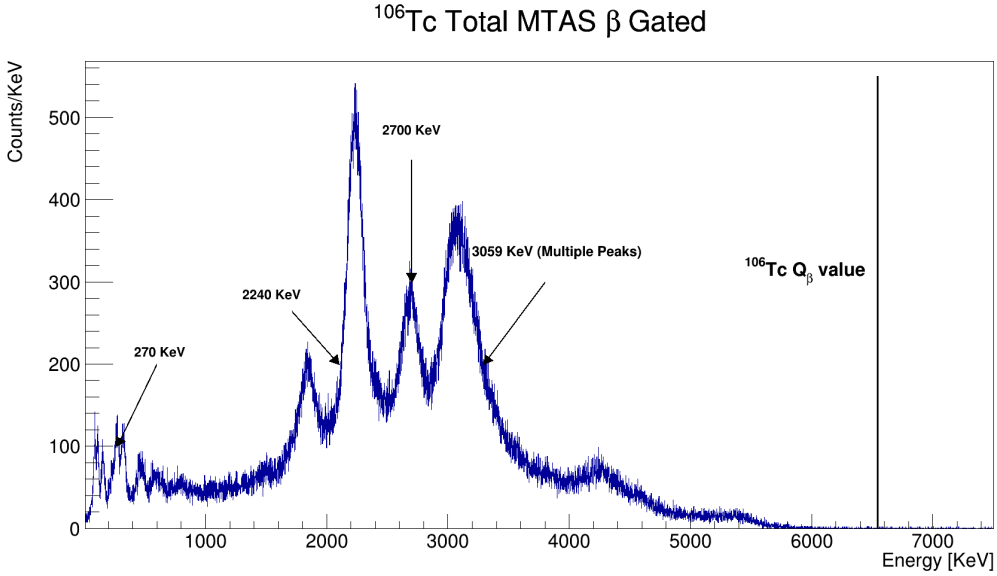

(b) β-gated ^{106}Tc spectrum.

Figure 5.1: (a) Experimental MTAS data, with the calibration gammas indicated. Both ^{40}K and ^{208}Tl are present in natural background radiation, and the ^{40}K gamma is artificially increased by putting KCl salt in close proximity to MTAS. (b) Experimental MTAS data with a beta gate applied. Note that this spectra still has contaminants included, but the background is reduced to near zero due to the beta gate.

not necessarily correspond to keV). The dual thresholds allow for counting only true beta signals. Walk corrections were looked into, and fitted parameters were developed, but were determined to not be necessary for beta gating the MTAS spectra sufficiently.

An example of applying a beta gate to the total MTAS spectra is provided in subfigure 5.1 (b).

5.2 Mass Contamination Effects in MTAS

One of the issues present with the mass 106 data is contamination. The primary source of contamination is from the (β, n) branch of the ^{106}Nb decay and hydrogenic atoms extracted from CARIBU. While the probability for this branch to occur is low (4.5%), it is enough to introduce decays of the A=105 mass chain into the spectra. ^{105}Mo has a similar halflife to ^{106}Tc at 35.6 seconds, making time gates alone not viable. ^{105}Ru has a large beta feeding to a 724 keV level, which is noticeable in the ^{105}Tc data (see figure 5.2). In all, the ^{106}Tc and ^{106}Mo data are contaminated by ^{105}Mo, ^{105}Tc, and ^{105}Ru. Due to time gates set to maximize ^{106}Mo statistics, ^{106}Mo also has ^{106}Tc daughter activity. To reiterate the decay scheme, the reader is directed again to fig 4.9.

The strategy for obtaining pure spectra is to start analysis with the longest lived isotopes, and consecutively subtract the contaminants until the desired pure spectra are obtained. For the ^{106}Tc, the first step is setting a time gate of 10 half-lives of ^{106}Mo to eliminate the parent from the spectra. Next, the ^{105}Tc spectra has a time gate of 10 half-lives of ^{105}Tc applied, to obtain a pure ^{105}Ru spectra. This is subtracted from a ^{105}Tc spectra that has a ten ^{105}Mo half-life gate applied, resulting in a pure ^{105}Tc spectra. This pure ^{105}Tc spectra is then subtracted from the ^{105}Mo spectra. At this point, pure spectra have been obtained of ^{105}Tc and ^{105}Mo, and by subtracting these from the 10 half-life gated ^{106}Tc, a pure spectrum of ^{106}Tc is obtained. Now that pure spectra of everything except ^{106}Mo has been obtained, it is easy to subtract off contaminants and get a relatively pure ^{106}Mo spectrum. An example

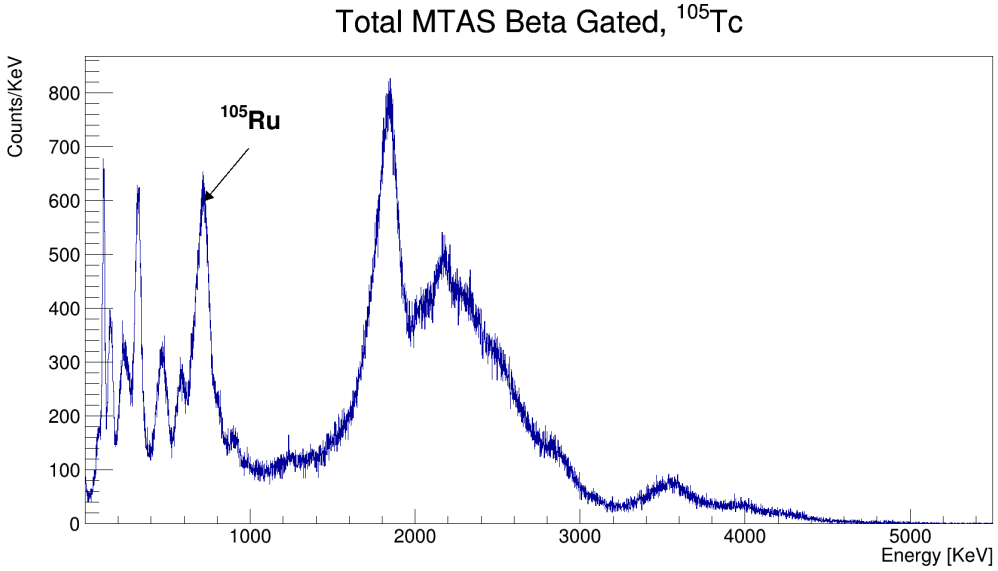

Figure 5.2: Experimental MTAS ^{105}Ru data with a beta gate applied. Of note is the large level feeding of ^{105}Ru at 724 keV. This is present in all of the A=105 data, and must be subtracted.

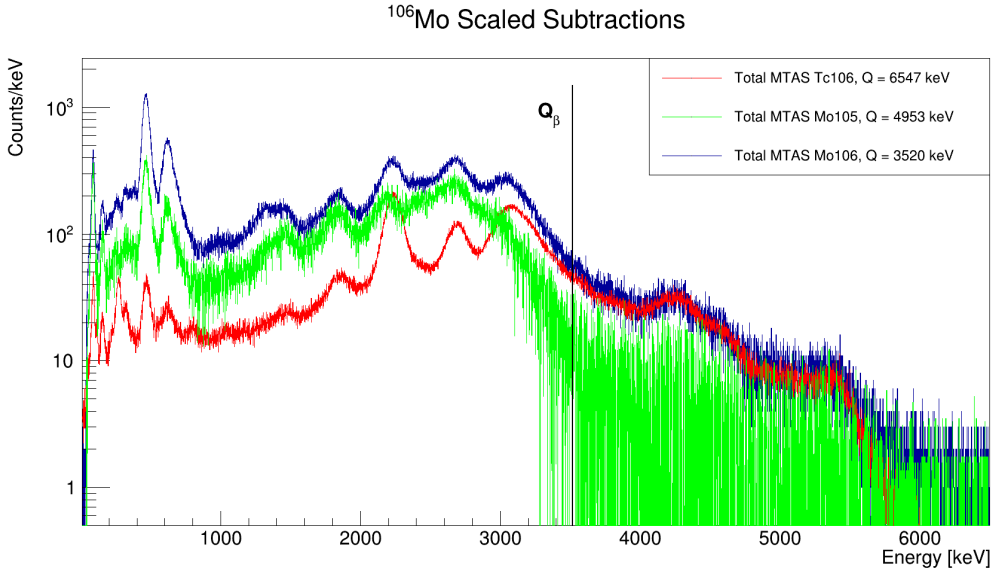

Figure 5.3: Experimental MTAS data for ^{106}Mo, along with scaled contaminants that are present in the raw data. Most of the contamination for ^{106}Mo is from the daughter ^{106}Tc, but there is a slight amount of ^{105}Mo contamination due to the 4.5% (β, n) channel from ^{106}Nb. The scaling of the contaminants is roughly what needs to be subtracted from the ^{106}Mo spectra.

of ^{106}Mo and its contaminants is shown in 5.3.

Cleaned ^{106}Tc and ^{106}Mo spectra are shown in figures 5.4 and 5.5, respectively. Comparisons to previous ENSDF data are shown in figure 5.6 and figure 5.7. Looking at figures 5.6 and 5.7, it is easy to see the pandemonium effect at play. Both spectra greatly overestimate the beta feeding intensities to low energy levels, while missing higher energy levels.

For ^{106}Mo, a rather large level at around 1330 keV is missed in the previous NNDC data for ^{106}Mo, as well as many pseudolevels at higher energies. The low energy levels below 200 keV are almost never directly fed, and are instead fed through cascade with higher energy levels, in contrast to the previous data. The peak around 600 keV is in fact due to the constructive interference of multiple gaussian peaks. The reason that the previous data is shifted to the right of the new data is due to the old data completely missing the peaks at 595,618, and 634 keV. The individual gamma rays were seen in the older data, but due to TAS being able to see nuclear levels far more clearly, the aforementioned peaks are indeed levels. These new levels cause feeding to shift from the assumed 672 and 736 keV levels to lower levels. These levels can be verified by $\gamma - \gamma$ coincidence.

For ^{106}Tc, the main issue with the older data is overfeeding to the levels below 2 MeV, notably the 270 keV level. By using $\gamma - \gamma$ coincidences and the ability of TAS to clearly distinguish levels, it can be seen that the 270 keV level is almost never fed, but is part of gamma-ray cascades for nearly all other levels.

5.3 HPGe Data

At the Argonne experiment, 2 HPGe detectors were used to identify/confirm beam composition. The ability to see individual gamma ray peaks is very useful in identifying potential contaminants. It is also useful to compare to NNDC data, to check that gamma

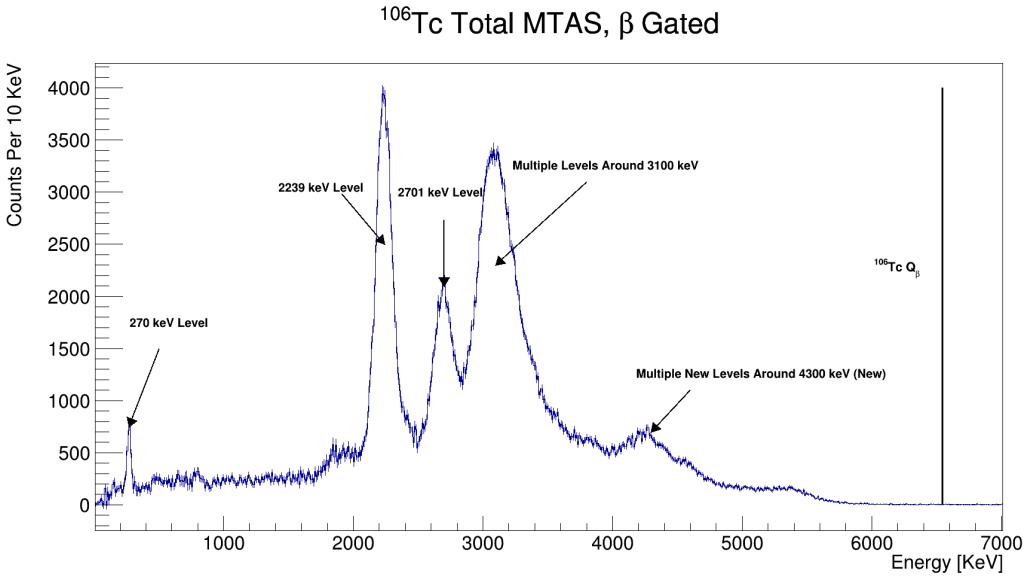

Figure 5.4: Experimental MTAS data for ^{106}Tc, cleaned of contaminants, and beta gated.

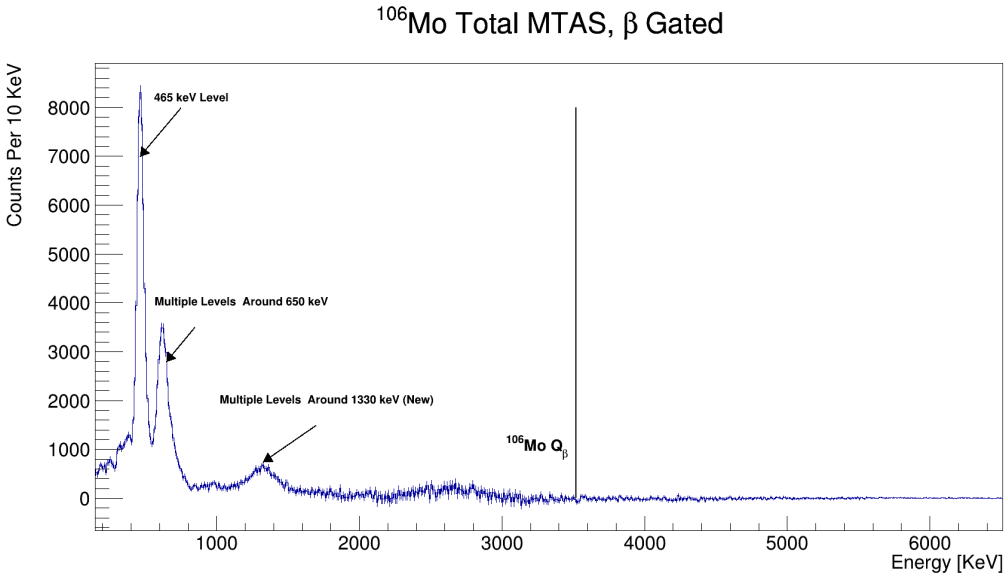

Figure 5.5: Experimental MTAS data for ^{106}Mo, cleaned of contaminants, and beta gated.

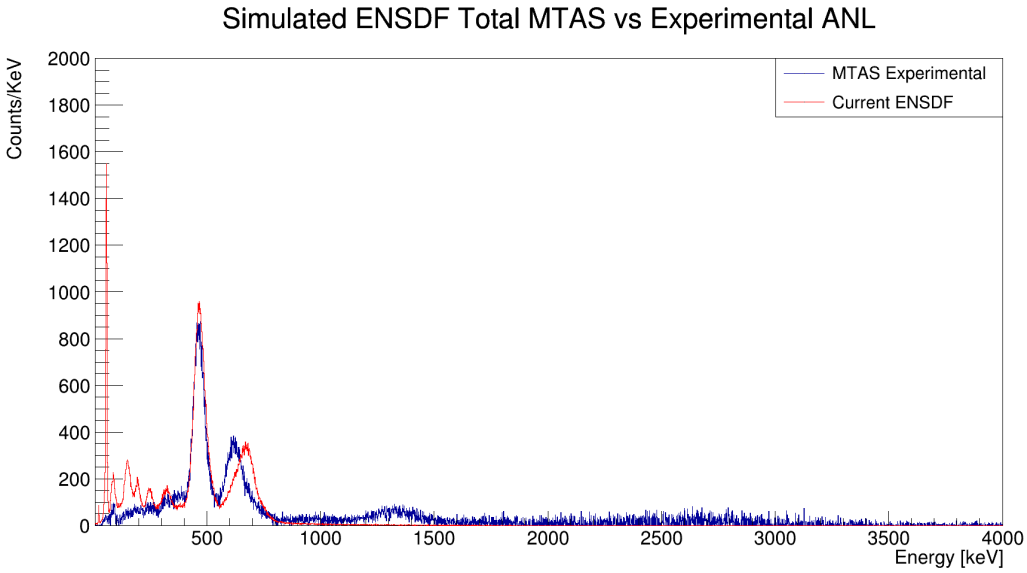

Figure 5.6: Experimental MTAS data for ^{106}Mo, cleaned of contaminants, and beta gated, compared to previous NNDC data, simulated with GEANT4.

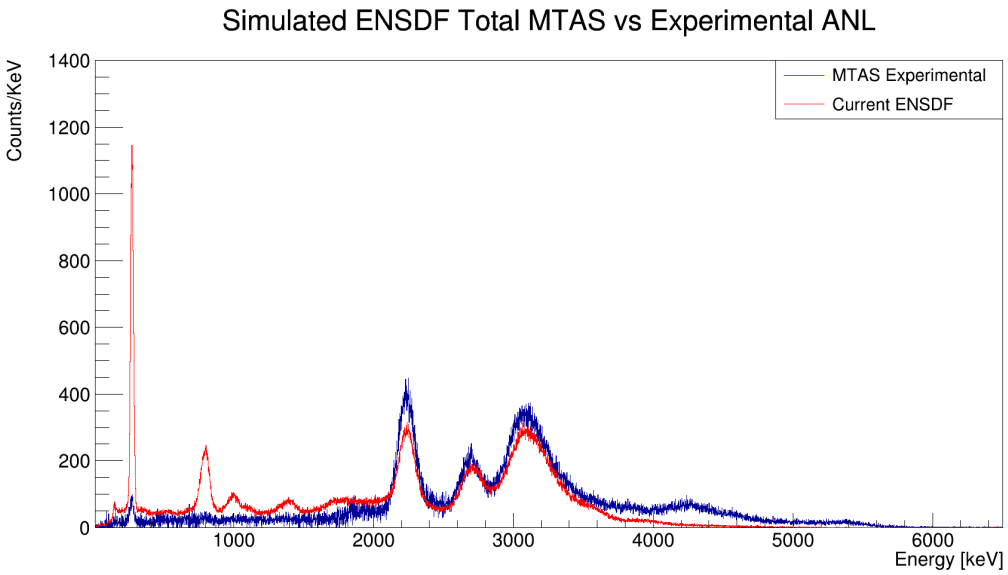

Figure 5.7: Experimental MTAS data for ^{106}Tc, cleaned of contaminants, and beta gated, compared to previous NNDC data, simulated with GEANT4

rays previously attributed to ^{106}Tc and Mo are indeed present. If sufficient statistics are present, it may be possible to do gamma-gamma coincidences with the HPGe data using the scintillator detector, however, the total efficiency of the HPGe detectors likely prohibits this. The beta gated ^{106}Mo HPGe spectrum is shown in 5.8.

5.4 GEANT4 Simulations

A GEANT4 model of MTAS was developed by A. Fijalkowska [27]. This GEANT4 model accounts for the modular design of MTAS, as well as non-linear light collection [28, 20, 19]. The GEANT4 model performs physics calculations simulating the radiation transport and light interaction within MTAS. Comparisons between experimental and GEANT4 data as part of the validation of the GEANT4 model can be seen in work by B. Rasco in figure 5.9.

This GEANT4 model is used to perform deconvolution of the individual decay paths present in the MTAS experimental data. More details on how this is done will be discussed in a further section. The GEANT4 model outputs data in a convenient ROOT format which can be tied together easily with other data.

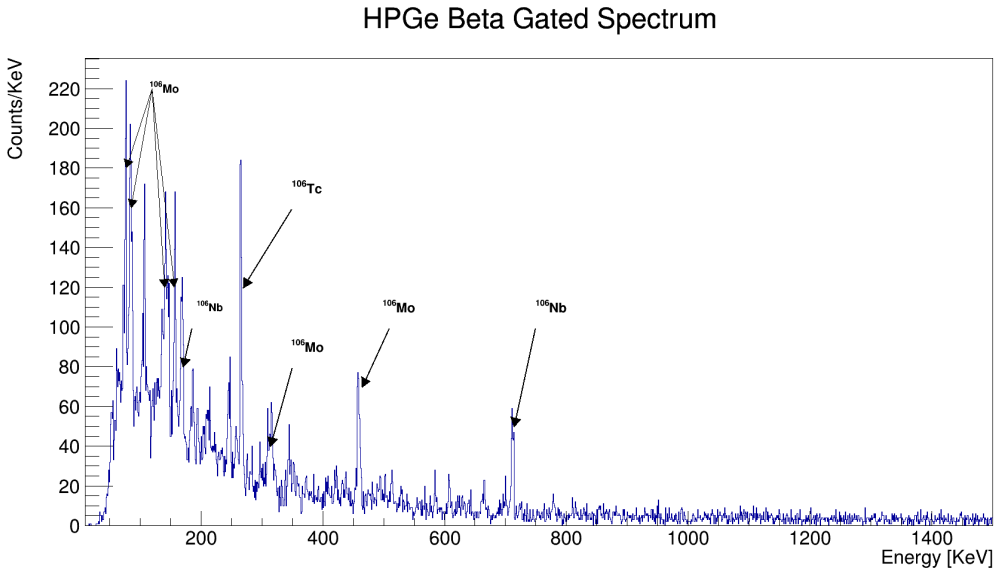

Figure 5.8: ROOT histogram showcasing experimental HPGe data for ^{106}Mo, with prominant peaks at 465 keV and 736 keV. Also of note is the presence of ^{106}Nb, implying a chance for ^{106}Nb data extraction.

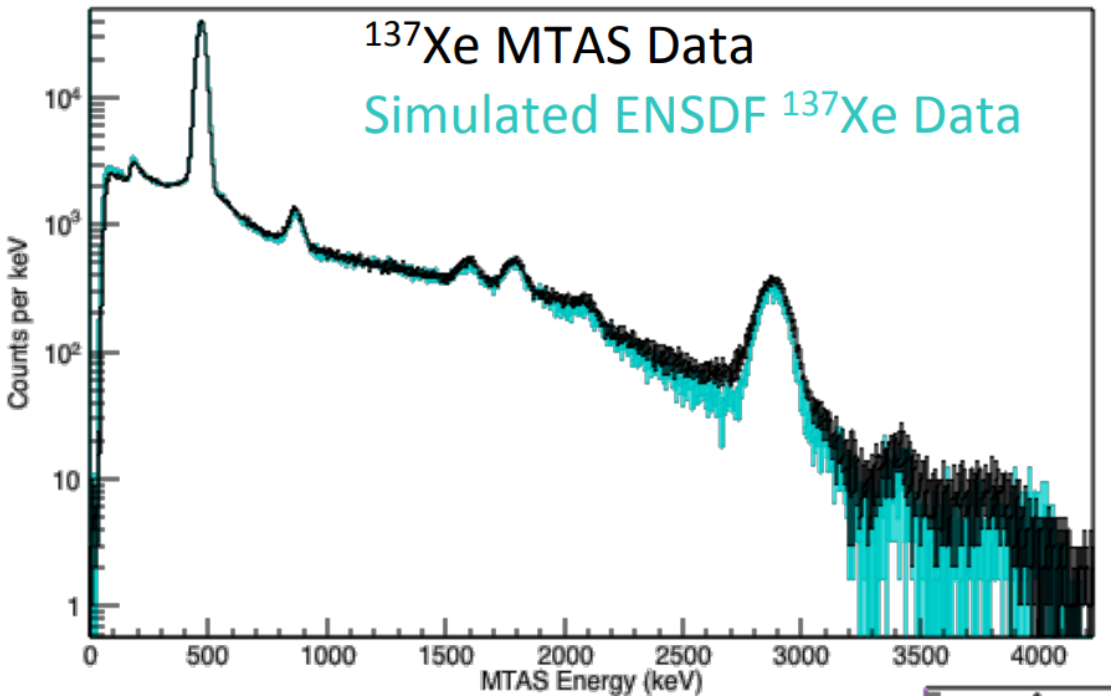

Figure 5.9: Figure showing MTAS experimental data which mirrors GEANT4 when using NNDC data for a well known isotope. [18]

Chapter 6

Extraction of Nuclear Physics Information

Now that the experimental data has been cleaned and prepared, it is possible to extract values for important physics parameters. Among the information which can be determined by the combination of experimental data and GEANT4 simulations are beta feeding intensities for ^{106}Mo and ^{106}Tc, nuclear matrix elements for Gamow-Teller decay, and expected beta energy spectra. These will be discussed below.

6.1 Beta Feeding Intensities

A primary goal of the experiments at Argonne, as well as the focus of this PhD, is to determine the beta feeding intensities of ^{106}Tc and ^{106}Mo. These values strongly affect reactor decay heat, and are currently only possible to truly determine with TAS data.

As mentioned before, beta decay schemes for neutron rich highly deformed nuclei are often very fragmented. Many decay paths can exist, of which some will have very low feeding intensities. The sum of these intensities must add to unity, as shown in eq (6.1).

$$I = \Sigma_i^m I_i = 1 \tag{6.1}$$

Deconvolution of TAS data is by definition a mathematically ill posed problem, as while solutions may exist, they are non-unique in most cases [29]. The general premise is that TAS experimental data linearly corresponds to the detector response function and the beta feeding intensities. However, due to the non-uniqueness of the deconvolution, creative approaches must be taken to solving the inverse problem. This has been thoroughly investigated by J. Tain and D. Cano-Ott [30], using methods by L. Lucy [31]. There are several possible deconvolution algorithms for TAS data, however, the one chosen for this research is the Expectation-Maximization method, as this is the method employed at ORNL.

Expectation-Maximization Method

To determine the beta feeding intensities, comparison between experimental and GEANT4 simulation data is done using the EM method. The EM method is iterative, and compares the differences between the GEANT4 individual decay paths and experimental data in a Bayesian approach, updating the decay path probabilities each iteration. The derivations and mathematics shown here are largely based on work by L. B. Lucy, J. Tain and D. Cano-Ott, as well as work by P. Shuai using MTAS [30, 31, 32].

For reference, a GEANT4 response function is a GEANT4 simulation of a single decay path, from the fed level, through cascade, to ground. Each branch of the cascade is simulated separately, to allow for the determination of path intensities. An example of this is shown in figure 6.1. In total, there are 566 response vectors, merged into one matrix R. Essentially, the observed experimental data is a convolution of many individual decay paths, forming a new distribution. What is observed, however, is this new distribution, requiring a deconvolution procedure to uncover the underlying individual decay path strengths.

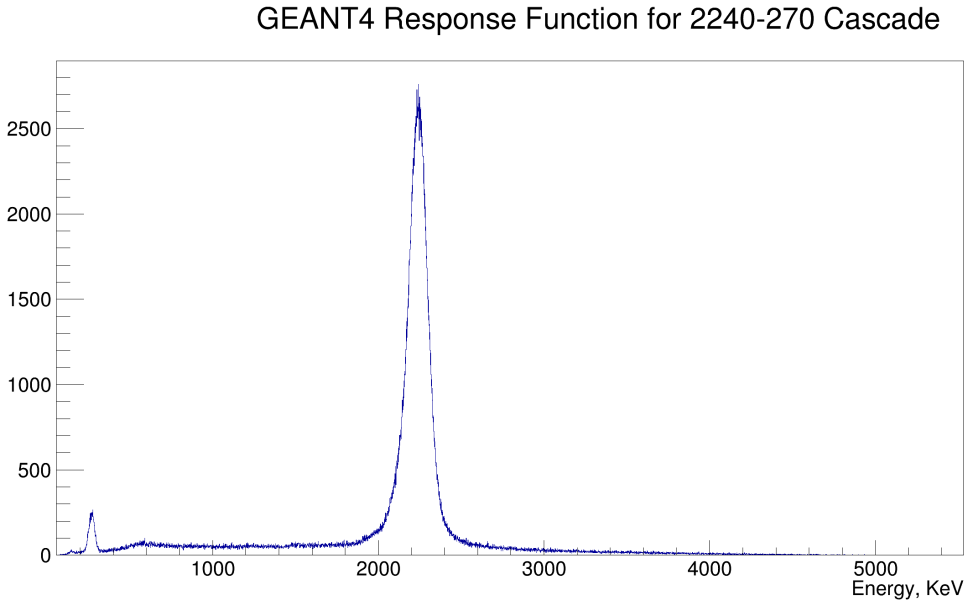

Figure 6.1: This ROOT Canvas shows a single response function for ^{106}Tc. This response function represents a ^{106}Tc decay to the 2239 KeV level, then gamma emission to the 270 KeV level, then gamma emission to ground. This is one of many possible paths for the decay of the 2239 KeV level.

We can start by assuming that a gamma ray of a particular energy y' is generated by our radioactive nucleus. This gamma ray will be detected with an energy of not y', but x', which accounts for the gamma ray's interaction with MTAS. X' is what MTAS will register as the gamma ray energy. This can be represented by the GEANT4 simulation, as it will take material and light physics effects into account. The GEANT4 representation of radiation interaction within MTAS has been validated by previous work from B. C. Rasco [18]. If we consider this to be the conditional probability that a gamma ray with energy y' will be detected as a gamma ray with energy x', then the GEANT4 response function represents the conditional probability density $P(x|y)$, using Bayesian terms. $P(x|y)$ in this case would the probability of a particular decay path given the current spectrum resulting from assumed x values.

Setting this scenario into Bayesian format, we then have a distribution which is observed, $\phi(x)$, a distribution which is composed of true decay paths $\psi(y)$, and a relation between the two with the kernel $P(x|y)$, our GEANT4 response function matrix. Then, equation 6.2 shows our integral equation representing $\phi(x)$.

$$\phi(x) = \int \psi(y)P(x|y)dy \tag{6.2}$$

If we let $Q(y|x)$ be the inverse probability, and assume x' = x, following the mathematics outlined in ref [31] we can arrive at the following equation 6.3.

$$Q(y|x) = \frac{\psi(y)P(x|y)}{\int \psi(y)P(x|y)dy} \tag{6.3}$$

Now, we can discretize equation 6.3. Based on work by J. L. Tain and D. Cano-Ott, we can assume that $\psi(y) = P(f_j)$, the probability of beta feeding to level j, and $P(x|y) =$

$P(d_i|f_j)$, which is the probability that measured data bin d_i is due to f_j [30]. This results in equations 6.4 and 6.5.

$$P(f_j|d_i) = \frac{P(d_i|f_j)P(f_j)}{\sum_{j=1}^{m} P(d_i|f_j)P(f_j)} \tag{6.4}$$

$$f_j^{(s+1)} = \frac{1}{\sum_{z=1}^{n} R_{zj}} \sum_{i=1}^{n} \frac{R_{ij} f_j^{(s)} d_i}{\sum_{k=1}^{m} R_{ik} f_k^{(s)}} \tag{6.5}$$

The f_j values are normalized using the following eq, where I_j is the beta feeding intensity I_β for decay path j.

$$I_j = \frac{f_j}{\sum_{j=0}^{m} f_j} \tag{6.6}$$

These I_j's are the feeding intensities to the levels of the nucleus of interest. To determine the correct feeding intensities, one would typically iterate over eq 6.5 several hundred times, to possibly several thousand times for highly fragmented decay schemes. This algorithm is proven to always converge given a sensible first guess (i.e., initialize values to be positive). This convergence is shown in the paper by Lucy et al [31].

This method can be extended to 2D by adding another loop around the summation. This is done by flattening the 2D matrix into a 1D matrix. The mathematics are the same for a 2D and 1D scenario assuming that the 2D matrix is flattened to 1D. It is also possible to fit the 2D and 1D spectra simultaneously, as long as the normalizations are correct. An example of this is shown in eq 6.7 and is based on ref [33].

$$f_a^{(s+1)} = \frac{\sum_{i=1}^{N} \frac{R_{ia} f_a^{(s)} d_i}{\sum_{k=1}^{m} R_{ik} f_k^{(s)}} + \sum_{i=1}^{N} \sum_{j=1}^{N} \frac{R_{ija}^{2D} f_a^{(s)} d_{ij}^{2D}}{\sum_{k=1}^{M} R_{ijk}^{2D} f_k^{(s)}}}{\sum_{k=1}^{N} R_{ka} + \sum_{k=1}^{N} \sum_{l=1}^{N} R_{kla}^{2D}} \tag{6.7}$$

This deconvolution algorithm has been implemented into a GPU based code using PyOpenCL. Since the MTAS experimental data d_i, the GEANT4 response matrix R_{ij}, and scale factor vector f_j can all be viewed as matrices, this deconvolution can benefit greatly from parallelization.

By using a 2D central versus total MTAS histogram, and doing deconvolution on a 2D spectra, it is possible to better identify the gamma intensities in cascade from the levels. This is required, as the 1D solution on its own is non-unique, meaning that there are multiple gamma cascades that could result in the same total MTAS spectrum, using different initial conditions. For example, it is possible to get a 2239 keV sum peak by either first decaying to the 270 keV level, or by directly going to the ground state. By applying an additional condition to satisfy, namely the 2D spectrum, it is possible to get more precise gamma cascade information.

6.2 Nuclear Matrix Element Calculations

As both ^{106}Mo and ^{106}Tc are neutron rich fission fragments with large Q_β values, an assumption going into this analysis is that they will primarily decay via allowed Gamow-Teller transitions. This involves a spin change of at most 1, and no parity change for the beta decay. The beta decay is assumed to be followed by a cascade of E1, M1, and E2 gamma-ray transitions.

The formalism of beta decay uses Fermi's Golden Rule, shown in eq (6.8).

$$\lambda = \frac{2\pi}{\hbar}|V_{fi}|^2\rho(E_f) \tag{6.8}$$

Eq (6.8) states that the decay constant λ is dependent on the matrix element $|V_{fi}|^2$, and the density of nuclear states. Following the mathematics outlined in Krane [34], one can arrive at the following equation (6.9).

$$ft_{1/2} = \frac{0.693 \cdot 2\pi^3\hbar^7}{g^2 {m_e}^5 c^4 |M_{fi}|^2} \tag{6.9}$$

$ft_{1/2}$, which is the Fermi function multiplied by the half-life, is known as the comparative half-life value of beta decay, and can be used to compare half-lives among isotopes, as it takes into account the differing nuclear charge Z. The value of $ft_{\frac{1}{2}}$ for an isotope can be useful in determining whether a decay is superallowed, allowed, or forbidden, and if forbidden, the extent of forbiddenness. These basic selection rules are shown in table 6.1.

Working with the assumption that ΔJ = 1, the type of beta decay expected for ^{106}Mo and ^{106}Tc is Gamow-Teller. If the type of beta decay is assumed to be 100% Gamow-Teller, then it is possible to set $|M_{fi}|^2 = |M_{GT}|^2$, as $|M_{fi}|^2 = |M_F|^2 + |M_{GT}|^2$, and $|M_F|^2 = 0$ for neutron-rich nuclei. To determine this nuclear matrix element, it is necessary to calculate ft values for the individual beta decay paths.

To calculate ft values, the log-ft code from NNDC was used [35]. This code uses the Q value, beta feeding intensities, and half-life to calculate the Fermi function values and partial half-lives. Once these ft values are obtained, it is possible to use eq 6.9 to determine the nuclear matrix elements. These B(GT) values will be compared to a paper by Sarrigueren and Pereira to analyze the deformation shape of ^{106}Mo [36].

Table 6.1: This table lists the basic selection rules for beta decay. The two isotopes being studied for this research, ^{106}Mo and ^{106}Tc, are both expected to be allowed Gamow-Teller decays, with $\Delta J = 1$. This table is a recreation of table 5-3 from Wong [37].

Basic Beta Decay Selection Rules				
Class	Total Angular Momentum ΔJ	Isospin ΔT	Parity Change	log-ft
Superallowed	$0^+ \rightarrow 0^+$	0	No	3.1-3.6
Allowed	0,1	0,1	No	2.9-10
1st Forbidden	0,1,2	0,1	Yes	5-19
2nd Forbidden	1,2,3	0,1	No	10-18
3rd Forbidden	2,3,4	0,1	Yes	17-22
4th Forbidden	3,4,5	0,1	No	22-24

6.3 Beta Energy Spectrum

Beta decay is a three-body decay, composed of the daughter nucleus, the beta particle (electron), and an anti-neutrino, to conserve lepton number. As such, the decay will not result in the beta particle having a definite energy in the same manner that gamma-rays do. Instead, the beta particle energy will have a distribution corresponding to a split of energy between the beta particle and the anti-neutrino.

In addition to the sharing of energy, another factor to consider for the beta spectrum is the fact that electrons are charged particles, emitting from a charged nuclear core. The physics regarding this electromagnetic force are accounted for by the Fermi function. The Fermi function, which is the same function as mentioned earlier in ft value calculations, is shown in eq 6.10, and is based on the paper by Hayen and Severijns et al [38].

$$F_0(Z,W) = 4(2pR)^{2(\gamma-1)}e^{\pi y}\frac{|\Gamma(\gamma+iy)|^2}{(\gamma(1+2\gamma))^2} \tag{6.10}$$

$$\gamma = (1-(\alpha Z))^{0.5} \tag{6.11}$$

$$y = \pm\frac{\alpha ZW}{p} \tag{6.12}$$

For this formulation of the Fermi function, alpha is the fine structure constant, Z is the nuclear charge, p is momentum, and R is the nuclear radius. This function as mentioned before accounts for the majority of the nuclear charge effects for beta decay. There are many corrective terms which can be applied, but they are generally of magnitude order 10^{-1} or smaller.

The code used for the beta energy spectra calculations of this research was created by Hayen and Severijns and is based on their paper mentioned earlier [39]. This code accounts

for multiple corrections to the beta spectra, including the finite size of the nucleus, radiative corrections, shape factor, atomic exchange, and atomic mismatch, among others.

The approach for calculating the beta spectra of ^{106}Mo and ^{106}Tc is to calculate the beta energy spectrum for each of the possible levels in each isotope. Then, the weighting for each spectrum is the beta feeding intensity for that level. Adding up each possible weighted level will result in the composite beta spectrum for the isotope.

Chapter 7

SCALE Evaluations of Impacts of Nuclear Data Revisions

One of the goals of this PhD is to determine the impacts of the updated beta feeding intensities on decay heat for nuclear fuel. During reactor operation, nuclei are constantly created and destroyed via neutron capture, fission, beta decay, and alpha decay. Once a reactor is shut down, the nuclear fuel will continue to decay, resulting in approximately 7% of the full power being emitted as decay heat. Which isotopes contribute to decay heat depends on time since shutdown, as short lived isotopes will decay off rapidly, and leave mostly actinides and long lived fission products. However, for emergency scenarios, these short lived isotopes are important, as they can produce a lot of decay heat, and the nuclear fuel must be actively cooled, typically with a borated water coolant as is implemented in current pressurized water reactors (PWR) in the US. ^{106}Mo and ^{106}Tc fall into the category of important short lived isotopes, due to their 8.73 and 35.6 second half lives, respectively, as well as their significant cumulative fission yields (see table 1.1).

7.1 SCALE Decay Heat Calculations

To calculate the change in the decay heat, it must be noted that decay heat primarily exists in 2 forms: gamma and beta. Beta heating will primarily heat up the center of the fuel rods, while gamma heating can escape to the surrounding fuel, fuel encapsulation, water, and lead shields. Thus, a change in decay heating from beta to gamma is what will be analyzed, along with the change to usable decay heat. From a nuclear engineering perspective, usable decay heat is decay heat with neutrino/antineutrino energy subtracted, as neutrinos rarely interact with matter. To calculate the change in decay heating, the ORNL SCALE code is being used, and in particular, the ORIGEN package which handles spent fuel decay, and the Couple package which handles changes to nuclear data, making appropriate libraries [8]. The following assumptions are being made for the nuclear fuel scenario.

Enriched Uranium Fuel

- For PWR scenarios, the reactor specific power is 20 MW for the first cycle, 19 MW for the second, and 18 MW for the third.
- Coolant density is 0.723 g/cm^3.
- The nuclear fuel is in the reactor for 3 18-month cycles.
- The nuclear fuel is based on the Westinghouse 17x17 design.
- There is a 40 day downtime between each power uptime cycle.
- Uranium enrichment is allowed to be 2.5, 3.0, 3.5, 4.0, 4.5, 5.0%.
- Resulting burnup is $\approx$ 30 GWD/MTHM (Gigawatt days per metric ton heavy metal).

Mixed Oxide Fuel

- For MOX fuel, the specific power if 40 MW for the first, second, and third cycles.

- Coolant density is 0.723g/cm^3.
- The nuclear fuel is in the reactor for 3 18-month cycles.
- The nuclear fuel is based on the Westinghouse 17x17 design.
- There is a 40 day downtime between each power uptime cycle.
- Plutonium percentage of MOX fuel is 10%. This is based on an equivalence of $\approx$ 5% U-235 enrichment. The plutonium percentage, along with the plutonium isotopics, is based on a paper by the IAEA [40].
- Resulting burnup is $\approx$ 65 GWD/MTHM.

The method for evaluating the variation in decay heat as a result of changes to underlying nuclear data is as follows.

Using the calculated beta spectra mentioned earlier, an average beta energy can be determined for the decay of ^{106}Mo and ^{106}Tc. This is done by weighting the average beta energy of each level of each isotope by its beta feeding intensity, then summing for each isotope. This average beta energy is combined with the average gamma energy, determined using a similar method as before, by weighting each gamma energy sum by the feeding to the appropriate level. This is necessary to calculate the net usable decay energy. For the purpose of SCALE calculations, neutrinos do not contribute to decay heat, and are not included in the average decay energy in SCALE.

Once the average decay energies are calculated, these values are put into the ORIGEN decay data file, to be compiled with COUPLE. However, a copy of the original values is saved, so that the effects on decay heat can be evaluated before new data is implemented, when new data for one isotope at a time is implemented, and when both isotopes' data are implemented. The specific values that need modified in the ORIGEN decay data file are the

gamma fraction of usable energy, and the total usable energy entries. These entries are defined in ref [8].

Chapter 8

Results

This chapter will first go through the fitting of the experimental MTAS data, showing the results of the GPU based deconvolution procedure which provide the beta feeding intensities. After this, using the beta feeding intensities, the extraction of physics parameters such as the nuclear matrix elements and beta spectra will be provided. Finally, updated SCALE calculations will highlight the impact of the data revisions, as well as the need to evaluate other nuclei of interest for nuclear engineering applications.

8.1 Deconvolution and Beta Feeding Intensities

The process of deconvolution starts with determining how many decay paths are necessary, and which gamma ray cascades are plausible. This is guided by the two-dimensional histograms for the experimental data showing correlations between gamma-rays detected in the central module and the the total sum of energies detected in MTAS. Low energy gamma rays seen in the cascade from a high energy level will show up in the central module, whereas the total level energy will appear in the total MTAS spectrum. High energy gamma-rays tend to occur in the inner, middle, and outer rings. By performing 2D to 1D projections, it is possible to identify which gamma rays belong to which level in which cascade, statistics

permitting. For very high energy levels with low feeding, it is not always possible to identify all gamma rays belonging to those levels. However, this method works the majority of the time. An example 2D histogram showing the central versus total spectrum for ^{106}Tc is shown in 4.6 earlier in this dissertation.

Table 8.1 lists the levels which are fit for the ^{106}Tc deconvolution. For energies above 3500 keV, pseudolevels are placed every 50 keV after the 3550 level, and every 100 keV after the 5000 keV level. This is due to lack of statistics at the higher energy levels. There are levels in this area, but due to both lack of statistics in the area and the pandemonium effect (many tightly spaced levels) the use of pseudolevels is necessary. Where it is possible to use the 2D spectra to identify levels (such as for the 4300 keV region), specific level energies are used.

Table 8.2 lists the levels which are fit for the ^{106}Mo deconvolution. Again, due to a lack of statistics at higher energies, pseudolevels are placed every 40 keV after the 1318 keV level, and every 25 keV after the 1892 level. The reasoning for lowering the bin width at higher energies is solely due to a lack of statistics at higher energy levels.

Now that the levels which are being fit have been described, it is possible to discuss the results of the deconvolution procedure. This discussion will start with ^{106}Tc, as it was the first data set worked on.

8.1.1 ^{106}Tc Fitting Results

For the ^{106}Tc deconvolution, there appears to be strong feeding to the 2239 keV, 2700 keV, 3000-3300 keV, and 4300 keV regions. This is seen in the experimental data shown in figure 4.6. This is in contrast to the current NNDC data showing a very high amount of feeding to the 270 keV level, and moderate feeding to the levels below 2239 keV. By applying the EM method to the GEANT4 data and experimental ^{106}Tc data, this research has managed

Table 8.1: Table listing the levels which were fit for ^{106}Tc as part of this PhD research. Most of these levels have multiple different gamma cascades possible, for a total of 601 decay paths fit, including ground state feeding.

^{106}Tc Fit Levels (keV)				
0	270.07	714.69	792.31	990.62
1091.55	1392.21	1688.41	1774.37	1885.61
2239.4	2632.82	2701.43	2945.94	3047.13
3059.53	3186.43	3259.43	3364.13	3550.98
3700.1	3800.1	3850.1	3900.1	3930.4
4000.1	4050.1	4100.1	4150.1	4200.1
4276.1	4350.1	4400.1	4450.1	4500.1
4585.1	4650.1	4700.1	4750.1	4800.1
4850.1	4900.1	4950.1	5000.1	5100.1
5200.1	5300.1	5400.1	5500.1	5600.1
5700.1				

Table 8.2: Table listing the levels which were fit for ^{106}Mo as part of this PhD research. Most of these levels have multiple different gamma cascades possible, for a total of 720 decay paths fit, including ground state feeding.

^{106}Mo Fit Levels (keV)				
0	53.9	77.35	86.98	139.49
150.87	162.8	188.88	196.77	242.82
309.37	326.37	448.83	465.55	504.12
595.0	618.0	634.0	672.58	736.7
814.0	960.0	1050.0	1260.0	1318.0
1380.0	1420.0	1460.0	1500.0	1540.0
1580.0	1620.0	1660.0	1700.0	1740.0
1780.0	1820.0	1860.0	1892.0	1925.0
1950.0	1975.0	2000.0	2025.0	2050.0
2075.0	2100.0	2125.0	2150.0	2175.0
2200.0	2225.0	2250.0	2275.0	2300.0
2325.0	2350.0	2375.0	2400.0	2425.0
2450.0	2475.0	2500.0	2525.0	2550.0
2575.0	2600.0	2625.0	2650.0	2675.0
2700.0	2725.0	2750.0	2775.0	2800.0
2825.0	2850.0	2875.0	2900.0	2925.0
2950.0	2975.0	3000.0		

to determine likely beta feeding intensities to the levels seen in the experimental data. The resulting composite fit is shown in figure 8.1. The composite fit is made up of the GEANT4 individual decay paths weighted by their beta feeding intensities, and added together to make a composite histogram. This is then scaled to the experimental data to maintain normalization. Figure 8.2 shows the individual path contributions on the same plot as the composite fit histogram. This is typically useful to visually see which components are contributing the most to a particular peak, however with 601 decay paths, for some peaks there are many paths that contribute.

As can be seen in figure 8.1, the overall fit quality for the ^{106}Tc data is very good. All major peaks and minor peaks are fit properly, and there are no anomalies. An interesting note is that most of the feeding is to higher energy levels, but most of the levels decay down to the 270 keV level before going to the ground state. This explains why high energy resolution data from previous experiments assumed a large feeding to the 270 keV level. This is typical of a deformed fission fragment nuclei, as the pandemonium effect will cause high energy resolution experiments to miss the many higher energy peaks. As such, the experiments would see the 270 keV level without the higher level cascading to the 270 keV level. This has large implications for nuclear decay heat, as will be discussed in the SCALE results subsection.

The beta feeding intensities are listed in table 8.3. Note that there is no observed ground state feeding, implying that it is a forbidden transition.

One way to verify the quality of the ^{106}Tc fit, is to look at how well projections on the 2D coincidence spectra are fit. This is shown in figure 8.3. This figure shows that not only is the total MTAS spectrum properly fit, but that the cascades which go through the 270 keV level are also fit .

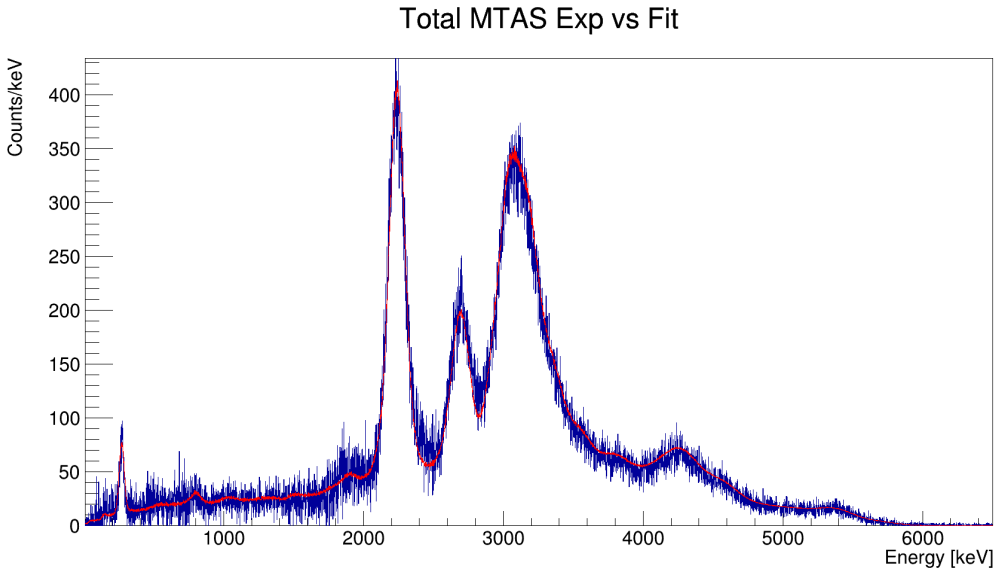

Figure 8.1: Experimental MTAS data for ^{106}Tc as well as the fit from the deconvolution procedure. The fit is shown in red, and the experimental data in blue.

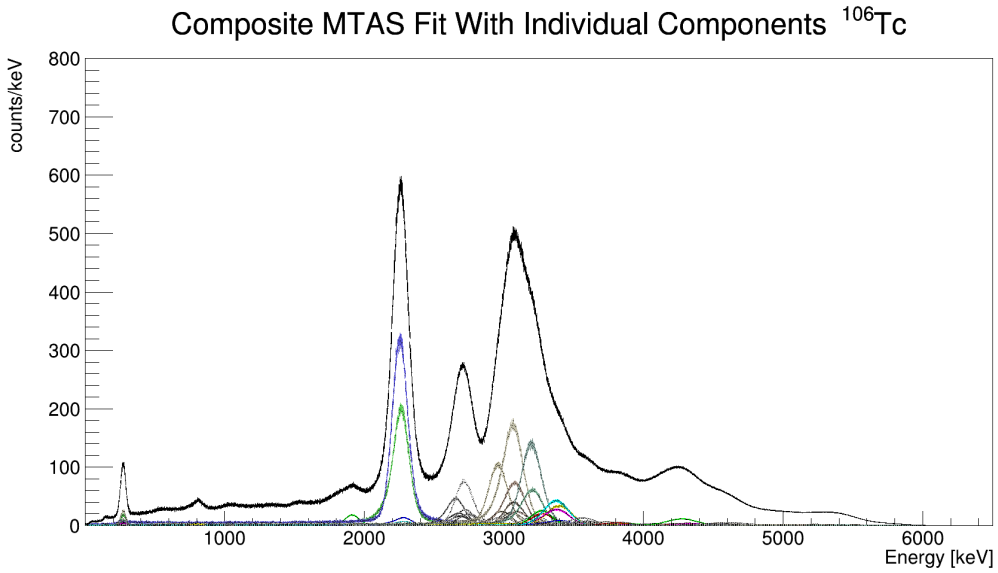

Figure 8.2: Individual decay path components of fit, along with the composite histogram (black). 601 decay paths were fit for ^{106}Tc. Only decay paths with beta feeding intensities greater than 1% are shown here.

Table 8.3: This table lists the beta feeding intensities determined from the deconvolution procedure for ^{106}Tc. For I_β of 0, the log-ft values are listed as undefined. Uncertainties on I_β values are calculated using summation in quadrature of error sources including GEANT4 error, energy calibration, and statistical uncertainty.

Energy keV	I_β	Log-ft	Energy keV	I_β	Log-ft
0	0	Undef	4050.1	0.674±0.023	6.522
270.07	0	Undef	4100.1	0.718±0.15	6.458
714.69	0	Undef	4150.1	0.754±0.089	6.399
792.31	0	Undef	4200.1	1.26±0.032	6.138
990.62	0	Undef	4276.1	2.551±0.022	5.772
1091.55	0	Undef	4350.1	1.396±0.15	5.974
1392.21	0	Undef	4400.1	0.888±0.079	6.129
1688.41	0	Undef	4450.1	0.42±0.043	6.412
1774.37	0.083 ± 0.047	8.654	4500.1	1.248±0.10	5.895
1885.61	0.546 ± 0.31	7.790	4585.1	1.238±0.11	5.823
2239.4	20.147 ± 0.013	6.071	4650.1	0.898±0.25	5.903
2632.82	1.784 ± 0.064	6.940	4700.1	0.339±0.060	6.279
2701.43	8.488 ± 0.31	6.229	4750.1	0.306±0.054	6.275
2945.94	3.939 ± 0.69	6.438	4800.1	0.312±0.014	6.217
3047.13	6.265 ± 0.36	6.182	4850.1	0.367±0.024	6.095
3059.53	8.978 ± 0.51	6.019	4900.1	0.078±0.0064	6.716
3186.43	11.796 ± 0.38	5.831	4950.1	0.445±0.023	5.906
3259.43	2.647 ± 0.35	6.438	5000.1	0.449±0.042	5.847
3364.13	7.199 ± 0.94	5.943	5100.1	0.736±0.090	5.517
3550.98	4.113 ± 0.26	6.073	5200.1	0.441±0.030	5.618
3700.1	1.525 ± 0.25	6.409	5300.1	0.465±0.029	5.464
3800.1	1.548 ± 0.019	6.337	5400.1	1.455±0.14	4.829
3850.1	0.858 ± 0.18	6.559	5500.1	0.371±0.10	5.272
3900.1	0.436 ± 0.029	6.819	5600.1	0.037±0.010	6.109
3930.4	0.462 ± 0.010	6.772	5700.1	0.612±0.17	4.711
4000.1	0.728 ± 0.018	6.525			

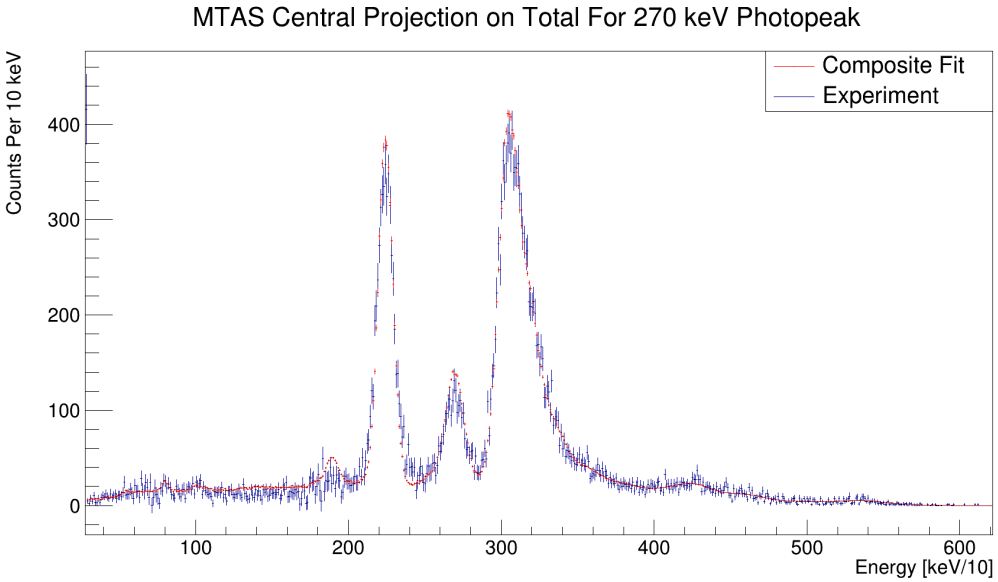

Figure 8.3: 2D experimental MTAS data for ^{106}Tc projected onto the total MTAS spectrum for the 270 keV peak, and compares it to the 2D fit projection for the same region. This shows that the 270 keV peak is correctly fit even for the 2D data, as the levels which the 270 keV peak is in cascade with are properly fit.

8.1.2 ^{106}Mo Fitting Results

For the ^{106}Mo deconvolution, there appears to be strong feeding to the 465 keV, 500-750 keV, and 1300-1400 keV regions. There is a slight but not insignificant amount of beta feeding in the post 2000 keV region, up until around 3200 keV. This is seen in the experimental data shown in figure 5.5. These post 2 MeV levels can be verified by looking at the central versus total coincidence spectra, with the post 2 MeV levels often decaying to known lower energy levels before going to ground. When comparing this data to current NNDC data, new levels are identified at 595, 618, 634 keV, as well as all levels after 736 keV. NNDC data notes that the current decay scheme is incomplete, as the Q_β is much higher than 736 keV [9]. Also of note, is that the current data evaluation puts the 595 and 618 keV gamma rays as individual gamma rays in cascade from the 672 keV level, and the 634 keV gamma ray is unassigned. This PhD research indicates that theses gamma rays are not individual gamma rays in cascade from the 672 keV level, but are in fact their own levels. This can be verified using the MTAS coincidence spectra. Figure 8.5 shows the individual path contributions on the same plot as the composite fit histogram.

Again, the quality of the fit can be verified using the projections of the 2D spectra. Figure 8.6 shows that not only is the total MTAS spectrum properly fit, but that the cascades which go through the 150 keV level are also fit .

8.1.3 ^{106}Tc Level Scheme

The updated level scheme is shown in figure 11.1. This PhD research has identified multiple new levels, as well as many pseudolevels where there are physical levels, but the level spacing is too tight to clearly identify a single photopeak. The most clearly defined new level is 4276, for which a clear photopeak exists. However, all of the level feeding post 3930 is new. Also of note, this research indicates that the 270 keV level is almost never directly fed, in

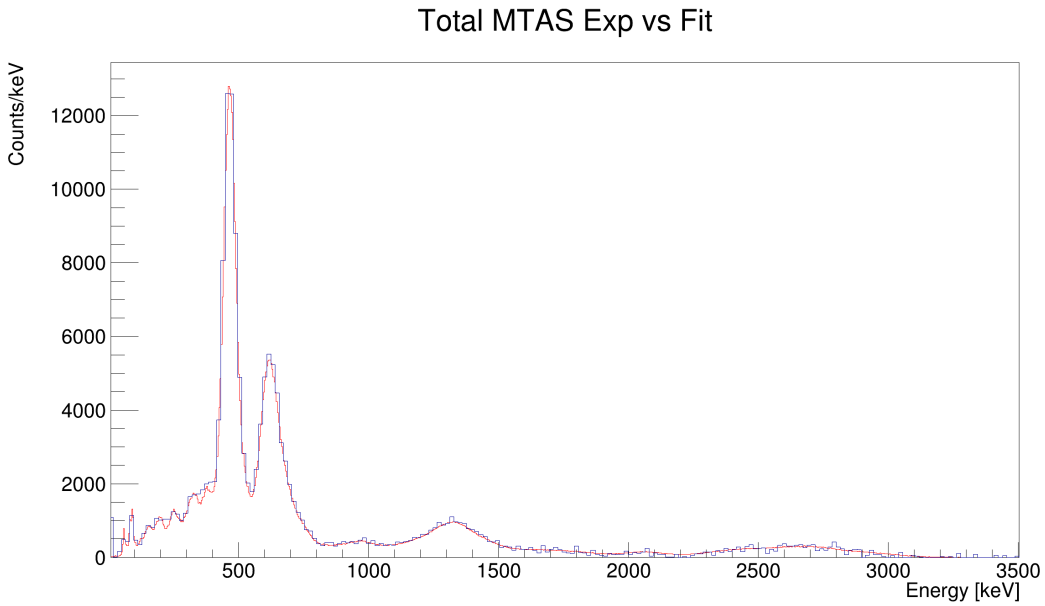

Figure 8.4: This figure shows the experimental MTAS data for ^{106}Mo as well as the fit from the deconvolution procedure. The fit is shown in red, and the experimental data in blue.

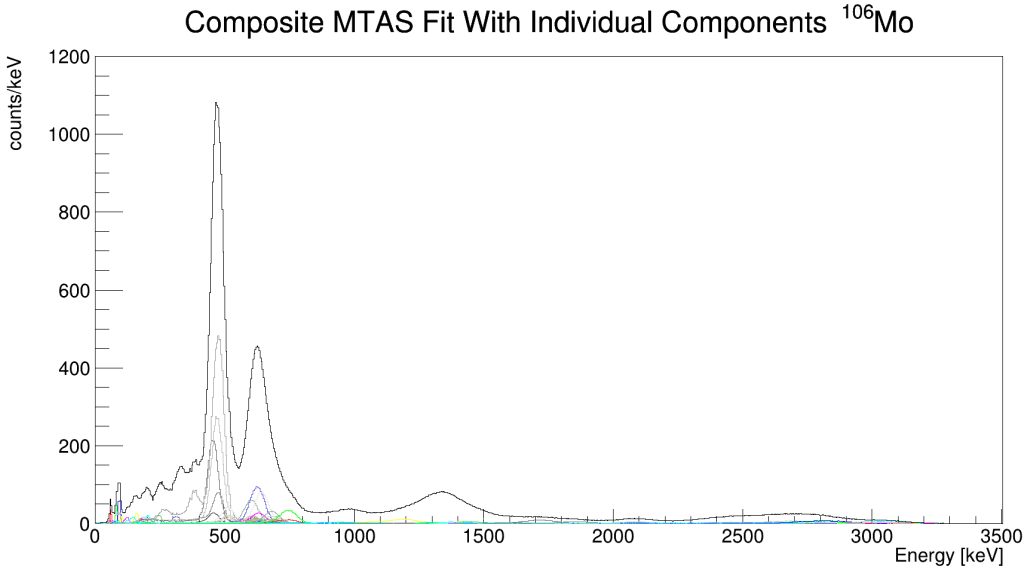

Figure 8.5: Individual decay path components of fit, along with the composite histogram (black). 719 decay paths were fit for ^{106}Mo.

Table 8.4: This table lists the beta feeding intensities determined from the deconvolution procedure for ^{106}Mo. For I_β of 0, the log-ft values are listed as undefined. Uncertainties on I_β values are calculated using summation in quadrature of error sources including GEANT4 error, energy calibration, and statistical uncertainty.

Energy	I_β	Log-ft	Energy	I_β	Log-ft
0	0	Undef	2000.0	0	Undef
53.9	0.21 ± 0.022	7.121	2025.0	0.22 ± 0.21	5.584
77.35	0.29 ± 0.031	6.965	2050.0	0.93 ± 0.67	4.938
86.98	0.42 ± 0.012	6.800	2075.0	0.006 ± 0.0056	7.098
139.49	0.094 ± 0.0033	7.423	2100.0	0.003 ± 0.0030	7.369
150.87	0.51 ± 0.013	6.683	2125.0	0	Undef
162.8	0	Undef	2150.0	0	Undef
188.88	1.1 ± 0.026	6.322	2175.0	0	Undef
196.77	0	Undef	2200.0	0	Undef
242.82	0.37 ± 0.015	6.775	2225.0	0	Undef
309.37	0.4 ± 0.023	6.701	2250.0	0	Undef
326.37	1.4 ± 0.082	6.146	2275.0	0.002 ± 0.0033	7.324
448.83	7.4 ± 0.27	5.345	2300.0	0.002 ± 0.0033	7.291
465.55	28.0 ± 0.59	4.761	2325.0	0.38 ± 0.083	4.978
504.12	4.0 ± 1.03	5.576	2350.0	0	Undef
595.0	6.5 ± 0.35	5.312	2375.0	0.5 ± 0.13	4.789
618.0	6.8 ± 0.36	5.283	2400.0	0.008 ± 0.0070	6.547
634.0	5.2 ± 0.13	5.386	2425.0	0.012 ± 0.0060	6.334
672.58	6.3 ± 0.93	5.281	2450.0	0.93 ± 0.092	4.407
736.7	2.1 ± 0.33	5.707	2475.0	0.39 ± 0.19	4.747
814.0	0.17 ± 0.07	6.749	2500.0	0.23 ± 0.093	4.928
960.0	2.7 ± 0.096	5.458	2525.0	0.31 ± 0.22	4.763

Table 8.4: Table 8.4 continued

1050.0	0.32 ± 0.023	6.307	2550.0	0.055 ± 0.024	5.476
1260.0	0.93 ± 0.35	5.687	2575.0	0.041 ± 0.023	5.561
1318.0	6.2 ± 0.18	4.820	2600.0	1.1 ± 0.74	4.100
1380.0	0.96 ± 0.13	5.576	2625.0	0.2 ± 0.062	4.784
1420.0	0.53 ± 0.053	5.800	2650.0	1.5 ± 1.07	3.872
1460.0	1.4 ± 0.10	5.358	2675.0	0.034 ± 0.041	5.464
1500.0	0.12 ± 0.053	6.382	2700.0	0.36 ± 0.040	4.395
1540.0	0.18 ± 0.0061	6.160	2725.0	0.031 ± 0.026	5.408
1580.0	0.59 ± 0.11	5.617	2750.0	0.19 ± 0.0075	4.568
1620.0	0.066 ± 0.049	6.530	2775.0	3.0 ± 0.36	3.327
1660.0	0.032 ± 0.0024	6.807	2800.0	0.11 ± 0.017	4.715
1700.0	0.89 ± 0.052	5.323	2825.0	0.021 ± 0.014	5.367
1740.0	0.088 ± 0.026	6.291	2850.0	0.002 ± 0.0089	6.332
1780.0	0.1 ± 0.020	6.191	2875.0	0.007 ± 0.049	5.730
1820.0	0.58 ± 0.014	5.392	2900.0	0	Undef
1860.0	0	Undef	2925.0	0	Undef
1892.0	0	Undef	2950.0	0	Undef
1925.0	0	Undef	2975.0	0.001 ± 0.00019	6.319
1950.0	0	Undef	3000.0	2.6 ± 0.50	2.835
1975.0	0	Undef			

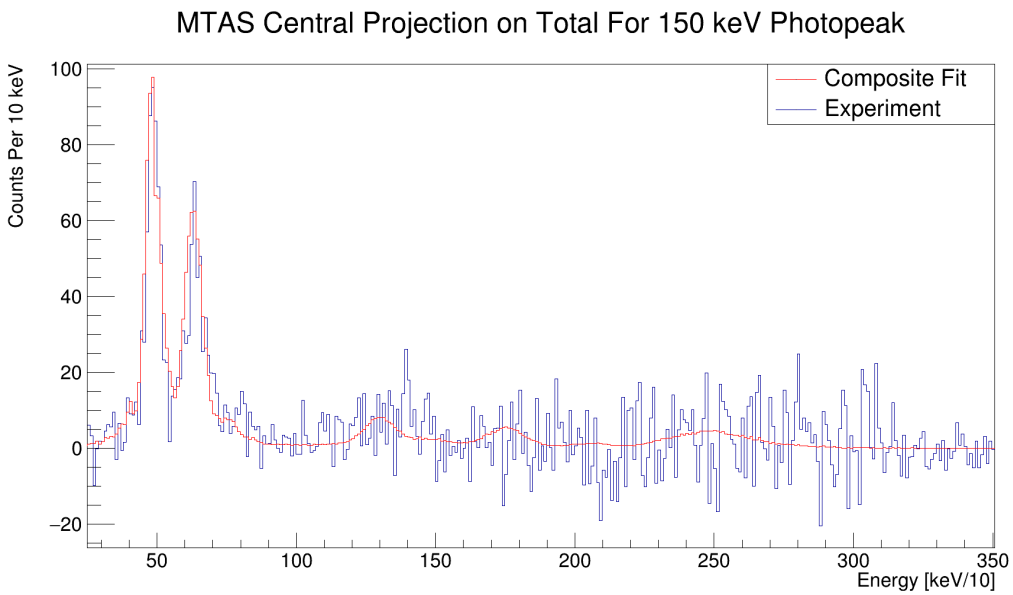

Figure 8.6: This figure shows the 2D experimental MTAS data for ^{106}Mo projected onto the total MTAS spectrum for the 150 keV peak, and compares it to the 2D fit projection for the same region. This shows that the 150 keV peak is correctly fit even for the 2D data, as the levels which the 150 keV peak is in cascade with are properly fit.

contrast to current NNDC data. This is not surprising, as the older high energy resolution data would be missing many of the higher energy gamma rays which cascade through the 270 keV level, artificially inflating the 270 keV level to look like a directly fed level. A complete NNDC style decay scheme is located in Appendix A.

8.1.4 ^{106}Mo Level Scheme

The updated level scheme is shown in figure 11.10. This PhD research has identified multiple new levels, as well as many pseudolevels where there are physical levels, but the level spacing is too tight to clearly identify a single photopeak. The most clearly defined new level is 1318, for which a clear photopeak exists. However, all of the level feeding post 736 keV is new. A complete NNDC style decay scheme is located in Appendix B.

8.2 Deduced Nuclear Physics Parameters

One of the practical applications of this PhD research is the determination of important nuclear physics parameters. In this section, the calculated nuclear matrix elements will be presented. Both isotopes are assumed to have entirely Gamow-Teller beta decays, as mentioned in chapter 6. Again, as mentioned in chapter 6, equation 6.9 can be rearranged to solve for B_{GT}, using known experimental ft values. This rearranged equation is shown in equation 8.1. Assumed constant values are $D = 6145$ and $\lambda^2 = (\frac{g_a}{g_v})^2 = 1.612$ [34].

$$B_{GT} = \frac{D}{ft(\frac{g_a}{g_v})^2} \tag{8.1}$$

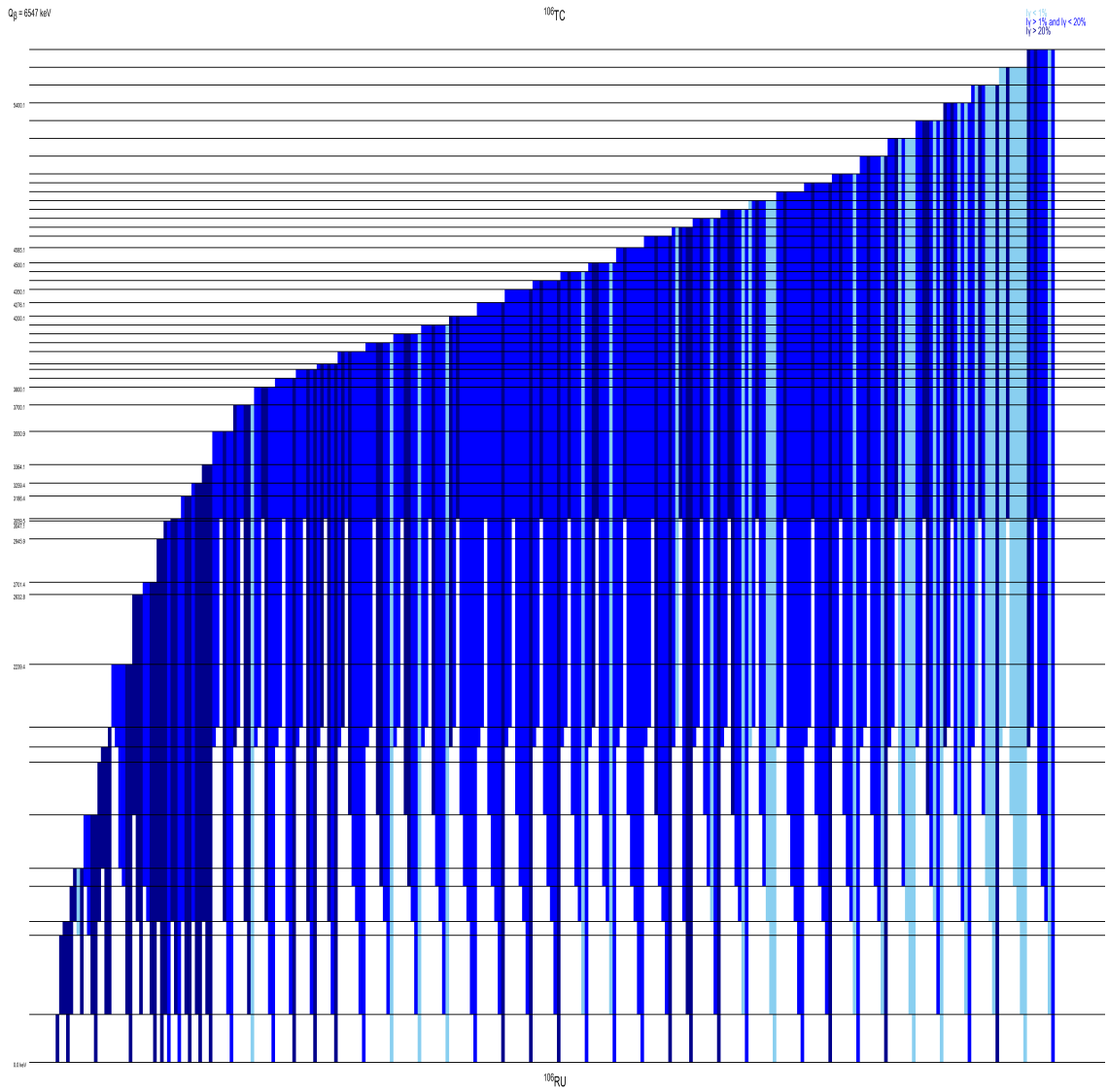

Figure 8.7: This figure shows the decay scheme of ^{106}Tc to ^{106}Ru. Note that all gammas being emitted from levels are normalized to 100%. This is due to how the decay path simulation in GEANT4 is performed.

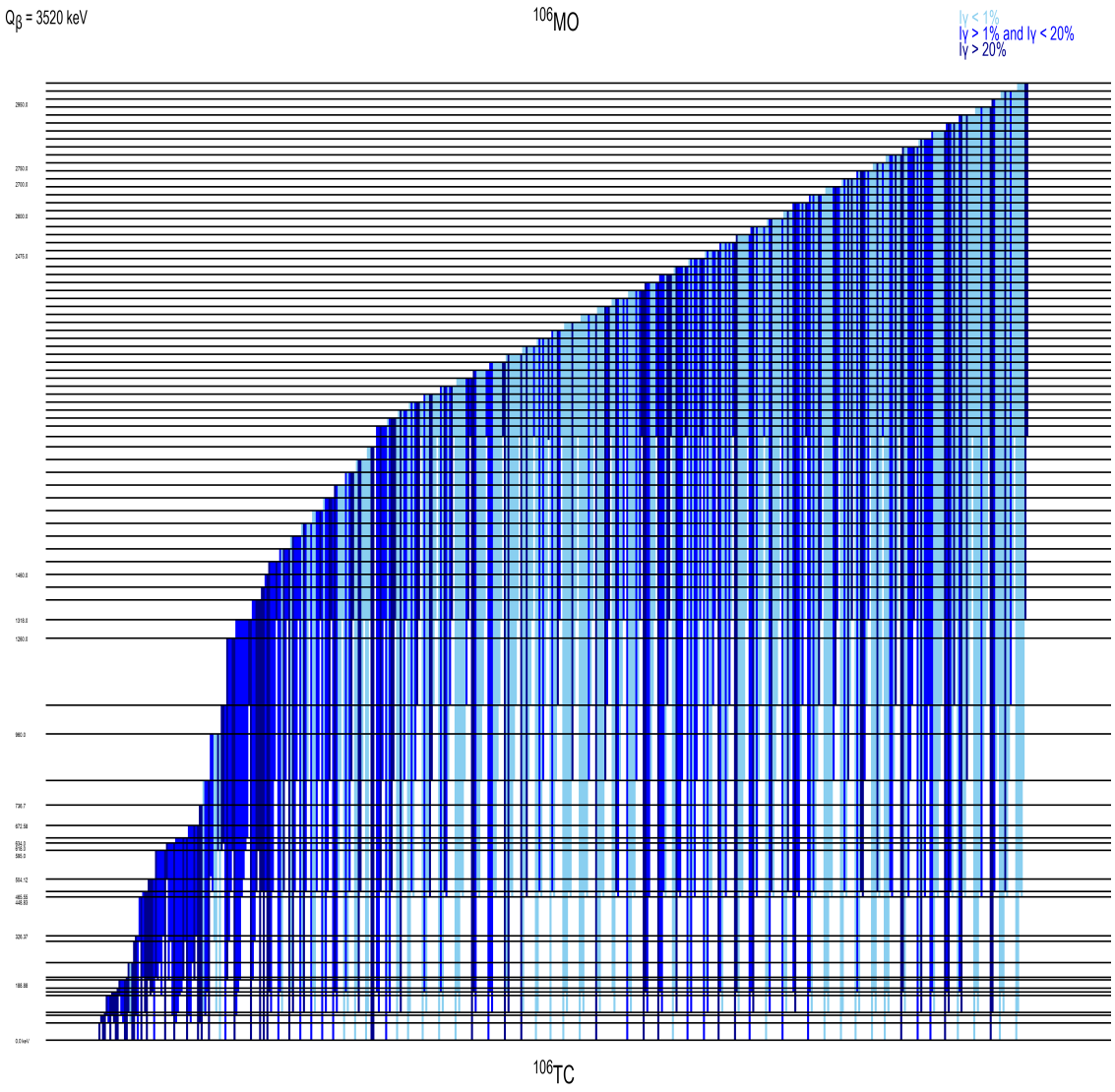

Figure 8.8: This figure shows the decay scheme of ^{106}Mo to ^{106}Tc. Note that all gammas being emitted from levels are normalized to 100%. This is due to how the decay path simulation in GEANT4 is performed.

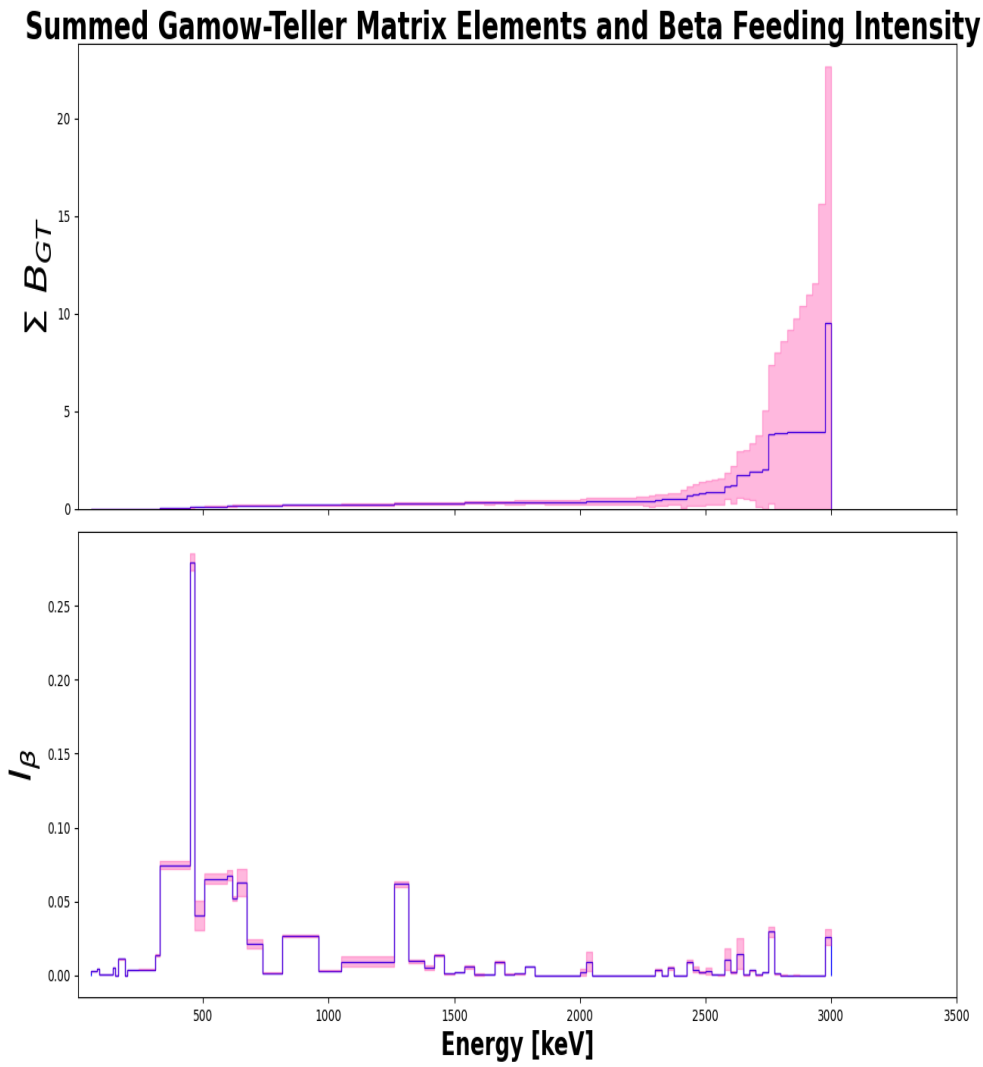

Figure 8.9: Summed Gamow-Teller strength distribution for ^{106}Mo, as well as the corresponding beta feeding intensity. Of note, is that even for small I_β, the existence of large Gamow-Teller strength is possible. In particular, the Gamow-Teller strength sees jumps in the 1300 keV region, and post 2000 keV. Note that nuclear physics parameters post 2500 keV suffer from very large uncertainties shown in table 8.4.

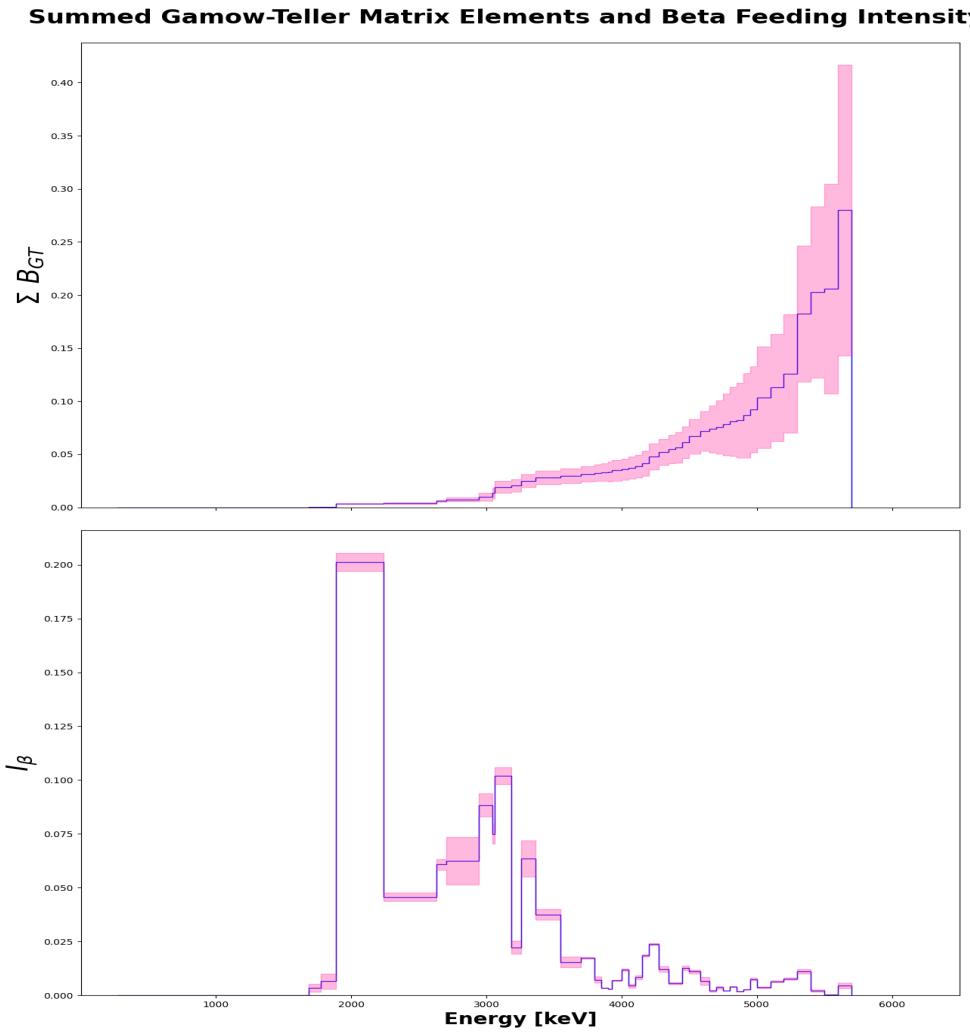

Figure 8.10: Summed Gamow-Teller strength distribution for ^{106}Tc, as well as the corresponding beta feeding intensity. Of note, is that even for small I_β, the existence of large Gamow-Teller strength is possible. In particular, the Gamow-Teller strength increases significantly after one of the most fed states at 2239 keV. The region post 5 MeV accounts for nearly half of the Gamow-Teller strength, while only accounting for several percent of overall I_β.

Using equation 8.1 and information from tables 8.3 and 8.4, it is possible to construct figures 8.9 and 8.10.

8.3 Beta Energy Spectra

The beta particle energy distributions were calculated for ^{106}Mo and ^{106}Tc using the code by Hayen and Severijns [39]. The calculated spectra will be shown below, as well as examples of the individual spectrum calculations for a single decay path.

As mentioned in chapter 6, the method for calculating the beta spectra for ^{106}Mo and ^{106}Tc is to calculate the beta decay spectra for each decay path of ^{106}Mo and ^{106}Tc, and then build a composite spectrum for each, which is composed of the weighted individual decay path spectra. As an example of a beta spectrum for an individual decay path, figure 8.11 is provided.

Once all of the paths are added to the composite histogram, the resulting spectra are figures 8.12 and 8.13. From these spectra the average beta energy for ^{106}Mo and ^{106}Tc can be determined. The bumpy shape comes from the fact that ^{106}Mo and ^{106}Tc decay to a vast number of levels, owing to their complex nuclear structure, as well as both isotopes having no ground state feeding.

8.4 SCALE Calculations

One of the primary motivations for this PhD research in addition to the nuclear physics considerations, is the application of new nuclear data improvements to nuclear engineering codes such as SCALE, which is frequently used for licensing and regulatory purposes for nuclear energy. This section will showcase the results of updates to the beta decay nuclear data

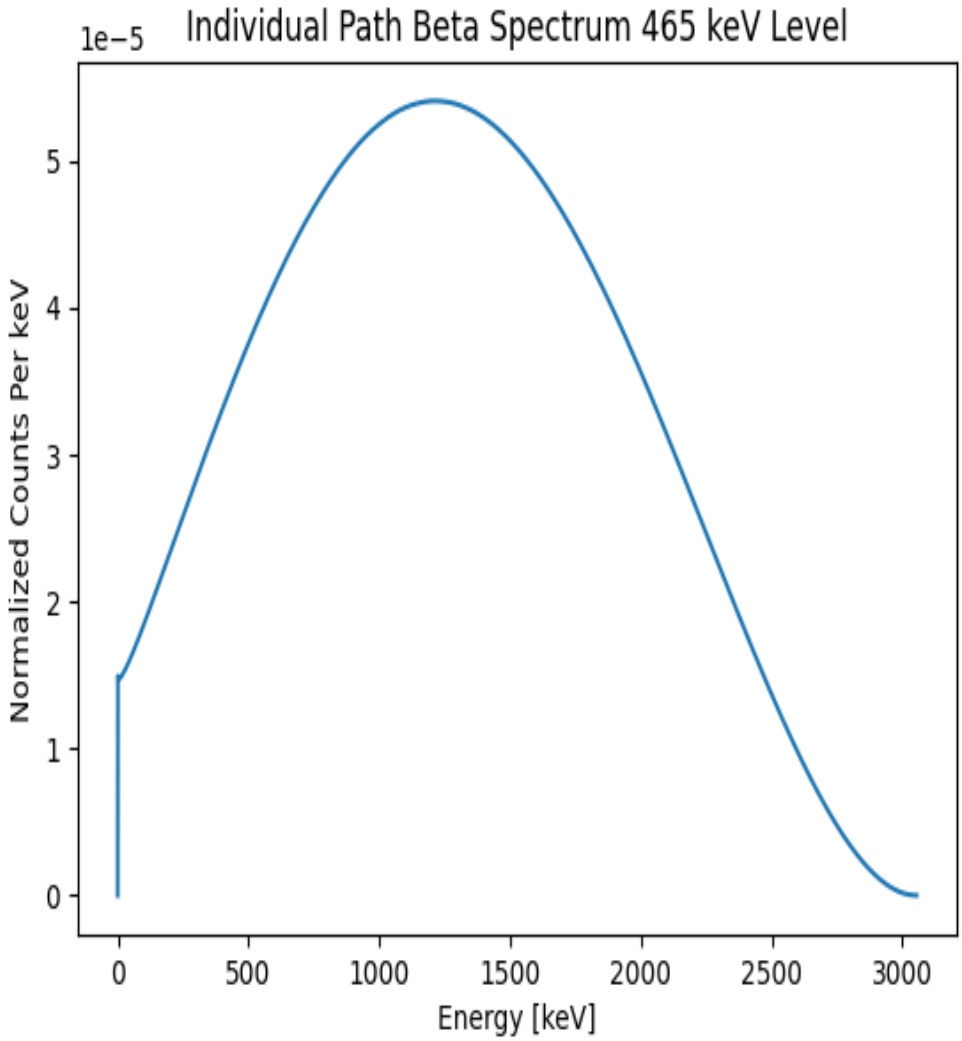

Figure 8.11: Beta energy spectrum for the 465 keV level of ^{106}Mo. The spectrum is smooth and continuous, with an average energy roughly $\frac{1}{3}$ of the max beta energy.

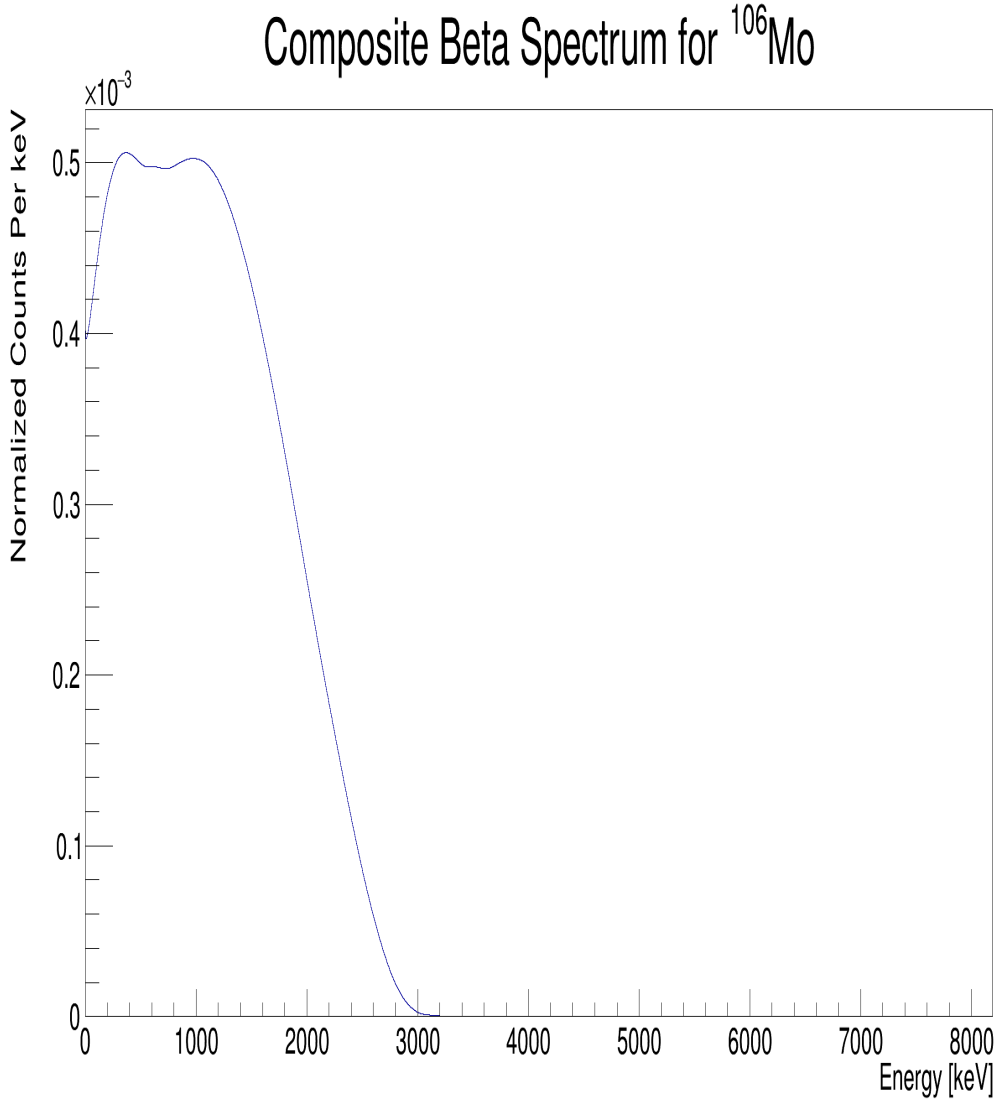

Figure 8.12: Composite beta energy spectrum for ^{106}Mo. The two larger bumps early on can be attributed to the large beta feedings of the 465 keV and 1318 keV levels.

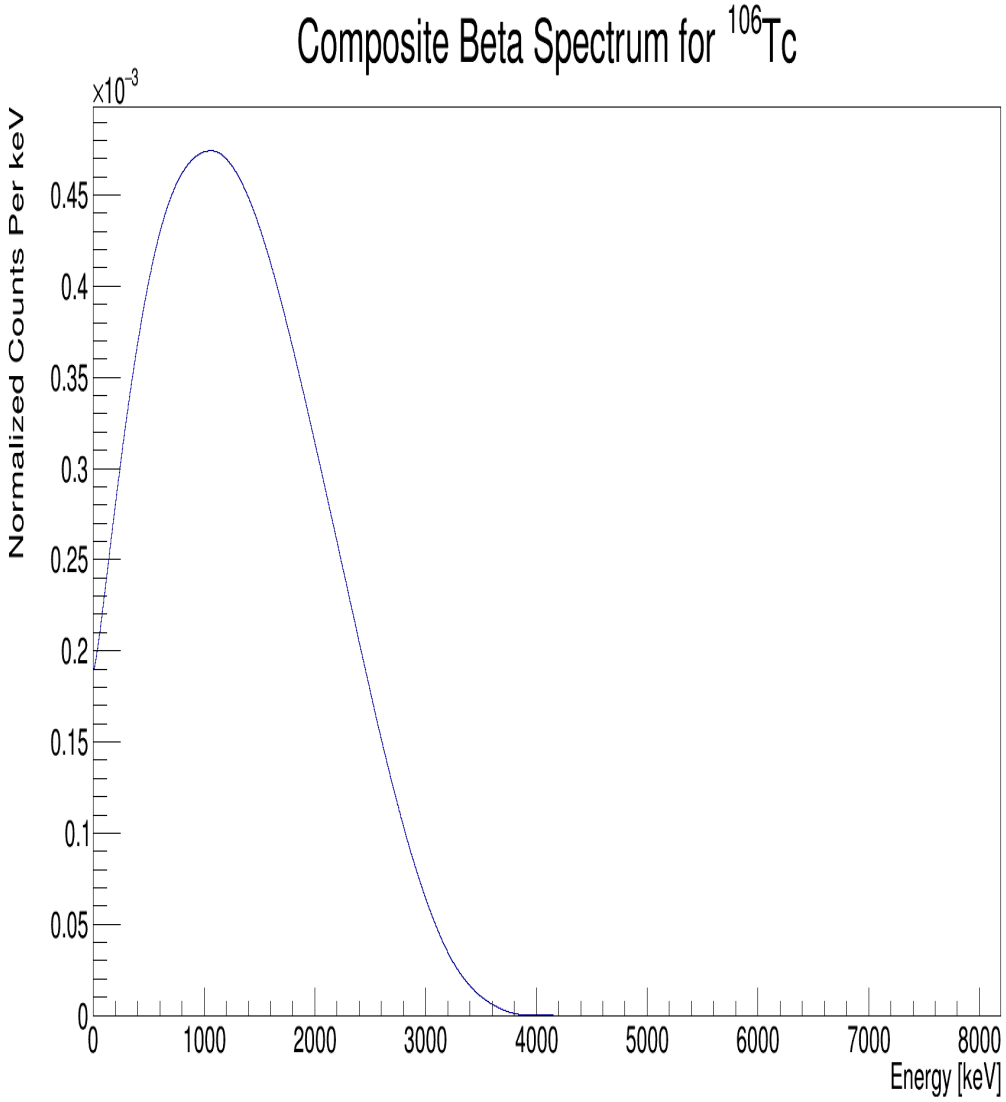

Figure 8.13: Composite beta energy spectrum for ^{106}Tc. The smoother bump of ^{106}Tc compared to ^{106}Mo is due to ^{106}Tc not having large gaps between fed levels, resulting in a smoother composite spectrum.

for ^{106}Mo and ^{106}Tc.

The most obvious changes due to adjustments to fission product data will occur in the post-shutdown spent nuclear fuel. As such, this research will focus on the region between 0 to 40 seconds for ^{106}Mo, and 0 to 80 seconds for ^{106}Tc. In addition to time since shutdown being a consideration, the fuel type also will make a difference, as the fission mass distribution will favor production of ^{106}Mo and ^{106}Tc more for plutonium fuel than for uranium fuel.

The first results that will be shown will be the changes to the distribution of gamma-ray heating as opposed to beta particle heating. As mentioned before, beta heating will not penetrate as far as gamma heating, creating a different scenario for heat dissipation and radiation shielding. Figure 8.14 and 8.15 show the percent of gamma ray heating for all isotopes that is due to ^{106}Mo and ^{106}Tc, respectively.

For a typical fuel enrichment of 4% ^{235}U, ^{106}Mo goes from accounting for $\approx 0.14\%$ of gamma-ray heating, to $\approx 0.25\%$ of gamma ray heating, a relative 79% increase immediately post-shutdown. This is largely due to the fact that prior nuclear data for ^{106}Mo only accounted for beta decay feeding up to the 736 keV level, and also overestimated feeding to the levels below 400 keV at the same time. In addition to this, prior data assumed ground state feeding, of which this research indicates there is a negligible amount. All of these factors combine to result in a massive relative increase in gamma-ray heating compared to prior data for ^{106}Mo.

Again using the scenario of 4% ^{235}U enrichment, for ^{106}Tc, the fraction of gamma-ray heating attributable to ^{106}Tc goes from $\approx 1.0\%$ to $\approx 1.4\%$ immediately after shutdown. This $\approx 40\%$ relative increase is largely due to two factors. The first is that the prior data only went to the 3930 keV level, and the second, is that the prior data significantly overestimated the amount of feeding to the 270 keV level, as well as overestimating the feeding to

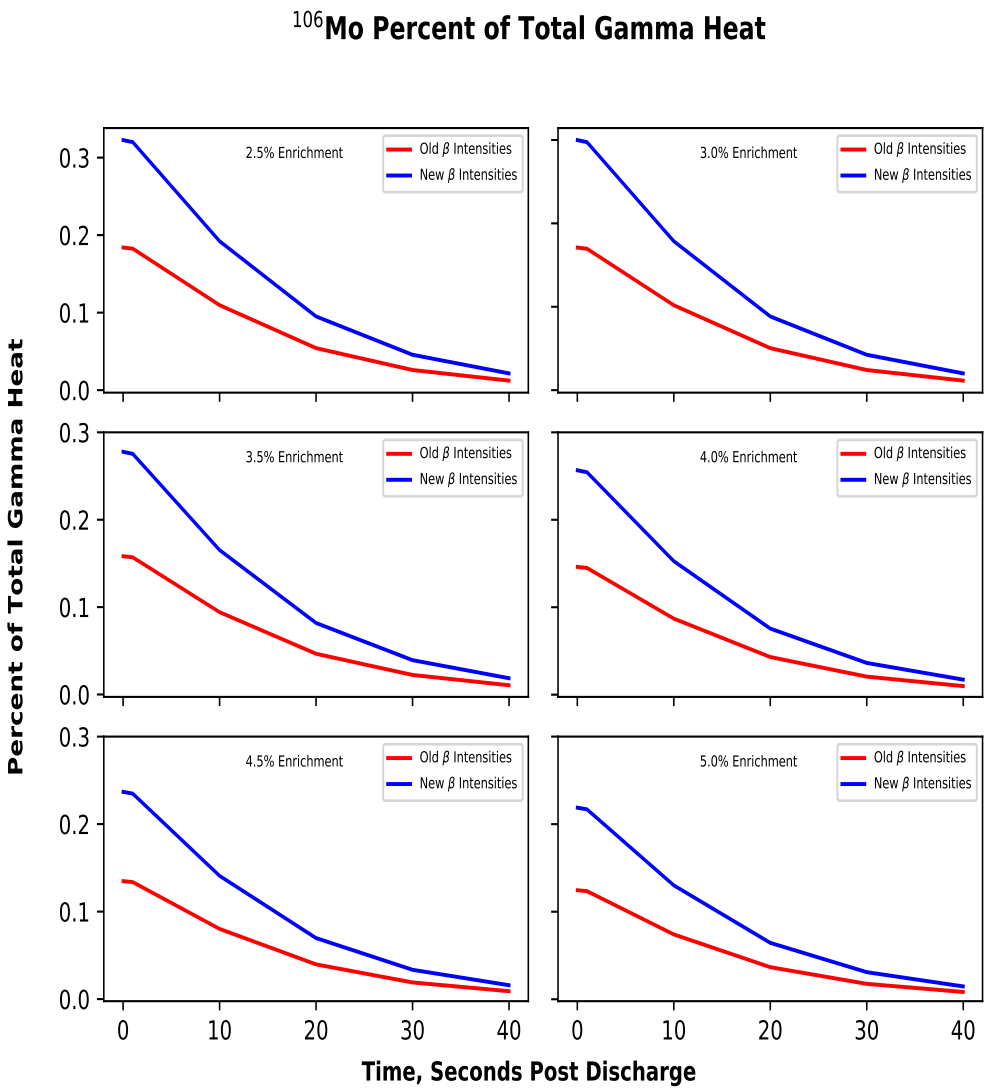

Figure 8.14: Change in the fraction of total gamma ray heating attributable to ^{106}Mo. As expected, the change is larger for lower ^{235}U enrichments, due to the larger amount of plutonium being bred ^{238}U and burned.

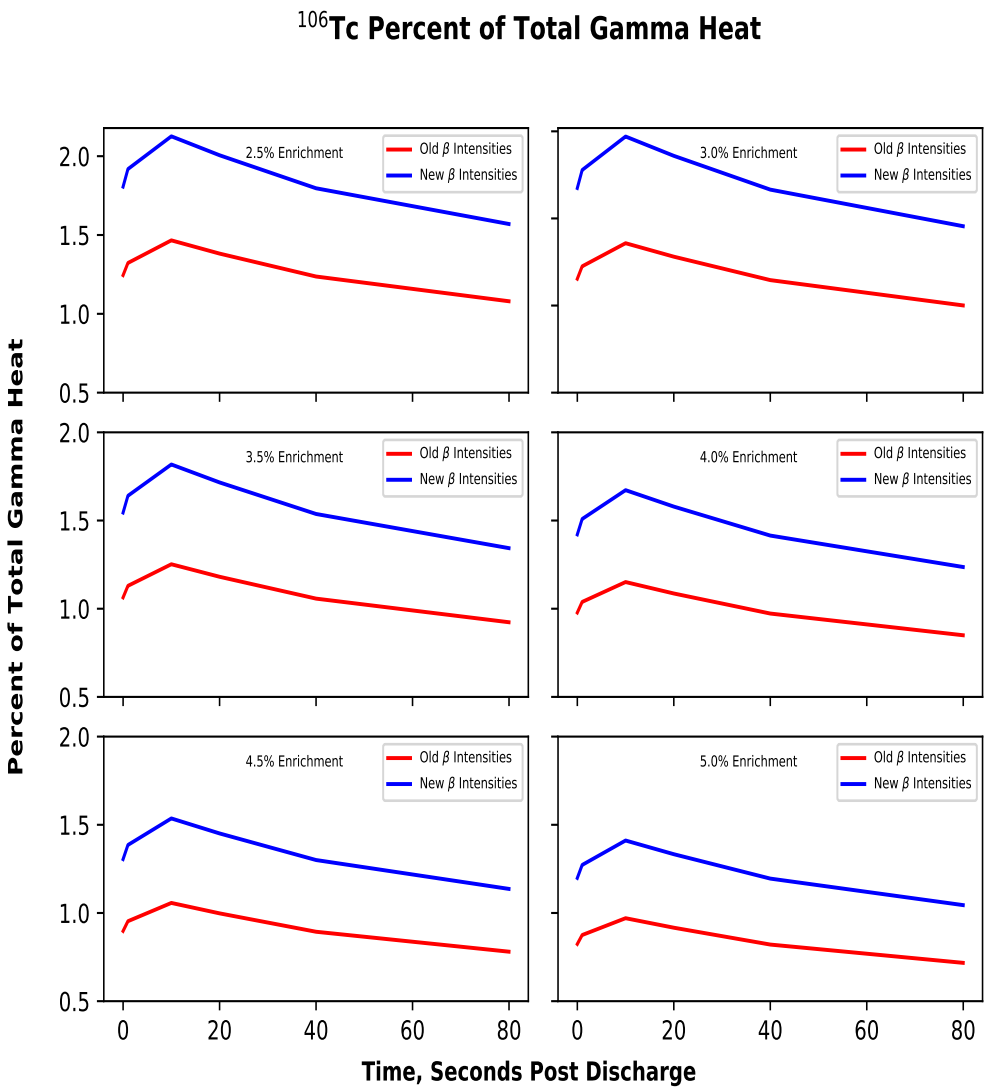

Figure 8.15: Change in the fraction of total gamma ray heating attributable to ^{106}Tc. As expected, the change is larger for lower ^{235}U enrichments, due to the larger amount of plutonium being bred from ^{238}U and burned.

all levels pre-2239 keV. The result of this is a large shift from beta heating to gamma heating.

Overall, gamma heating is increased by around 0.55% for 4% enriched ^{235}U fuel, as shown in figure 8.16. This figure highlights the importance of ^{106}Mo and ^{106}Tc for spent nuclear fuel decay heat, as well as emergency reactor shutdowns.

The next changes of note, are the changes to the overall decay heat. This occurs due to what is termed "usable decay heat". For the purposes of nuclear reactors and fuel, neutrinos and anti-neutrinos have nearly zero contribution to decay heat due to their incredibly small interaction cross sections. However, they do still carry away energy which is shared in a distribution with the beta particles and daughter nuclei. Therefore, if an isotope shifts energy to gamma-ray decay energy, it will also lower the amount of energy lost to the beta decay anti-neutrino. This serves to increase the overall effective decay heat, since the gamma-rays do not have to share energy. This is shown in figures 8.17 and 8.18.

For ^{106}Mo, there is a relative increase in its contribution to total nuclear decay heat of $\approx 8.2\%$, going from accounting for 0.253% to 0.274% of decay heat. For ^{106}Tc, the result is even more pronounced, with the relative increase in its contribution to total decay heat being $\approx 12.5\%$, going from accounting for 0.886% to 0.997% of decay heat. The combined change to decay heat is shown in figure 8.19, with the combination of the changes to ^{106}Mo and ^{106}Tc causing an increase in usable decay heat of $\approx 0.13\%$.

In lieu of presenting varying concentrations of ^{239}Pu in MOX fuel, an average value of 60% will be considered [40]. The resulting increases to gamma ray energy over time and total decay energy over time are presented in figure 8.20. These figures show that for MOX fuel there is an $\approx 1\%$ increase in overall gamma ray energy, and a $\approx 0.24\%$ increase in total decay energy at shutdown when considering the new ^{106}Mo and ^{106}Tc data.

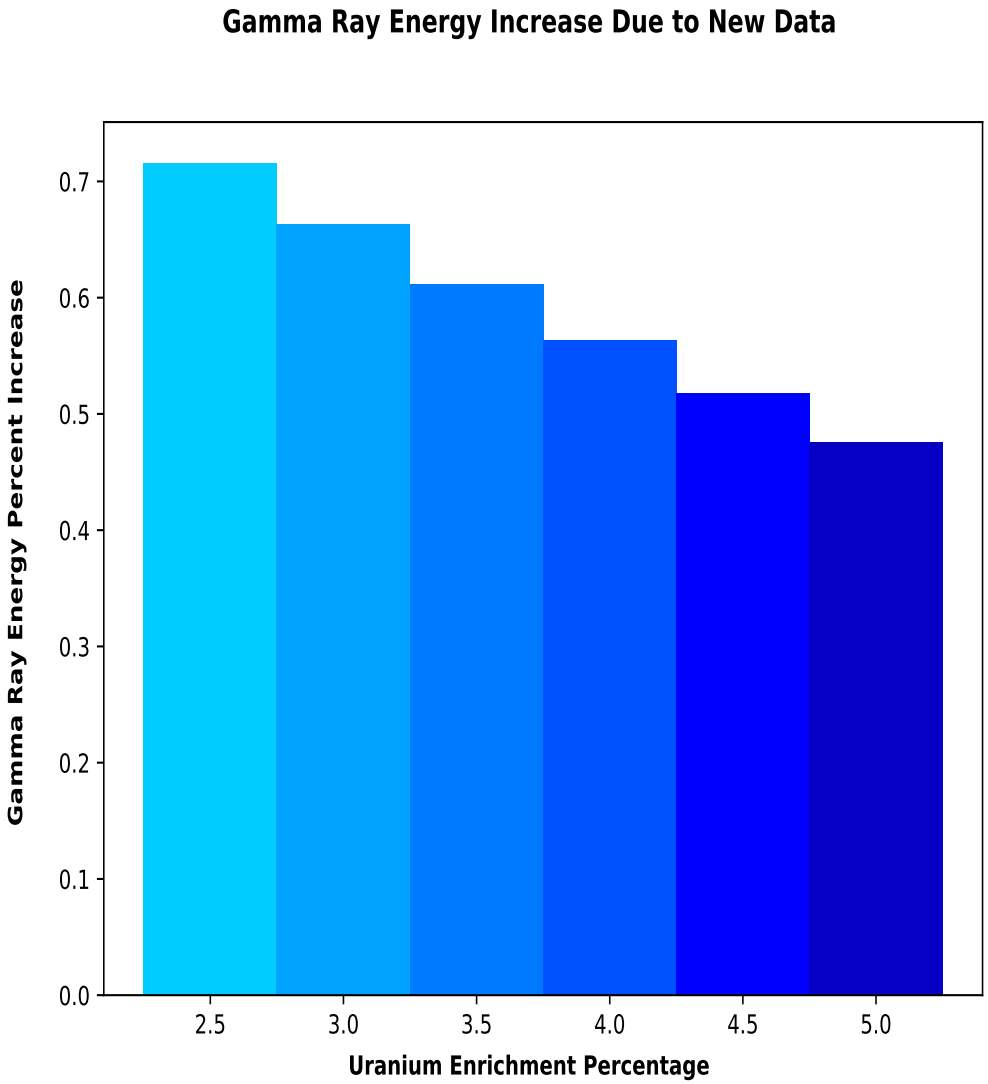

Figure 8.16: Change in the total decay heat that is attributable to ^{106}Mo and ^{106}Tc combined. As expected, the change is larger for lower enrichments, due to the larger amount of plutonium being bred and burned.

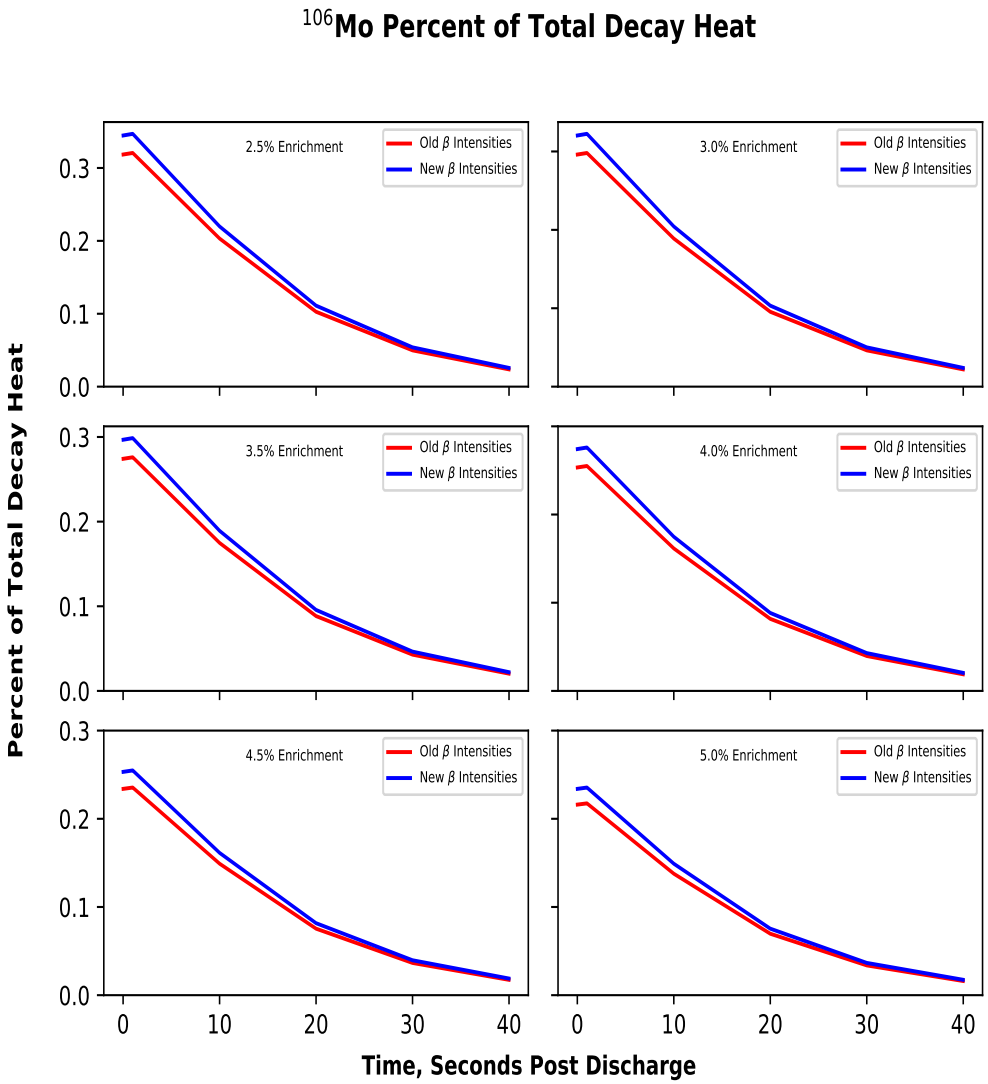

Figure 8.17: This figure shows the change in the fraction of total decay heat attributable to ^{106}Mo. As expected, the change is larger for lower enrichments, due to the larger amount of plutonium being bred and burned.

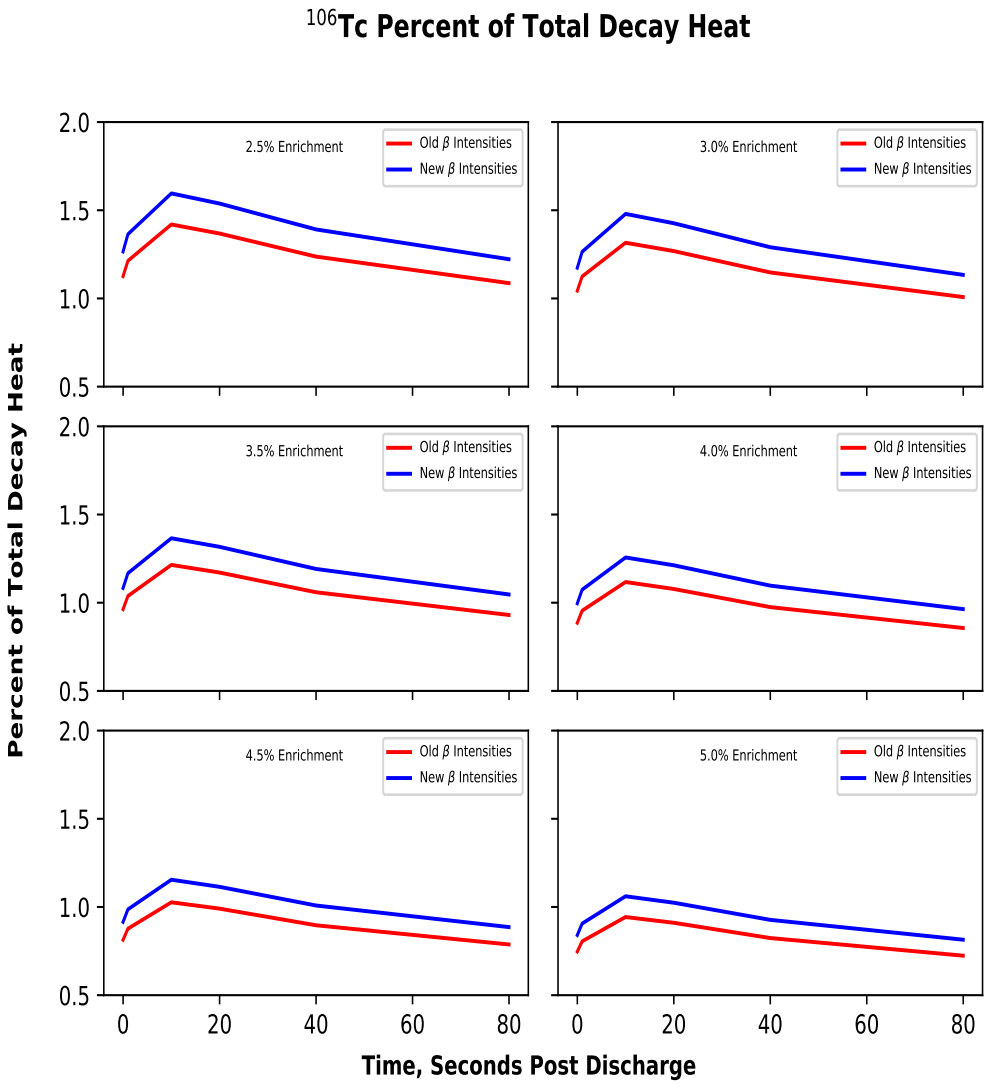

Figure 8.18: Change in the fraction of total decay heat attributable to ^{106}Tc. As expected, the change is larger for lower enrichments, due to the larger amount of plutonium being bred and burned.

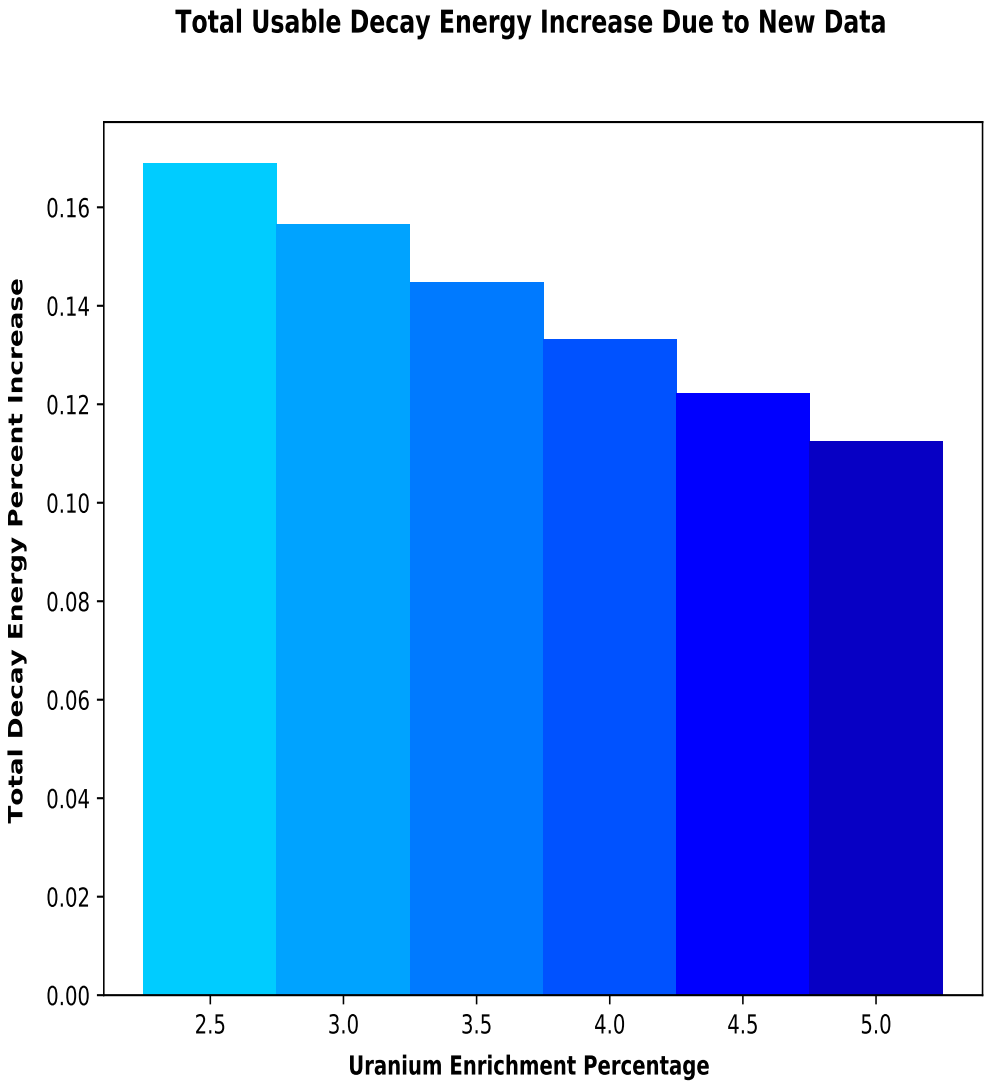

Figure 8.19: Change in the total decay heat that is attributable to ^{106}Mo and ^{106}Tc combined. As expected, the change is larger for lower enrichments, due to the larger amount of plutonium being bred and burned.

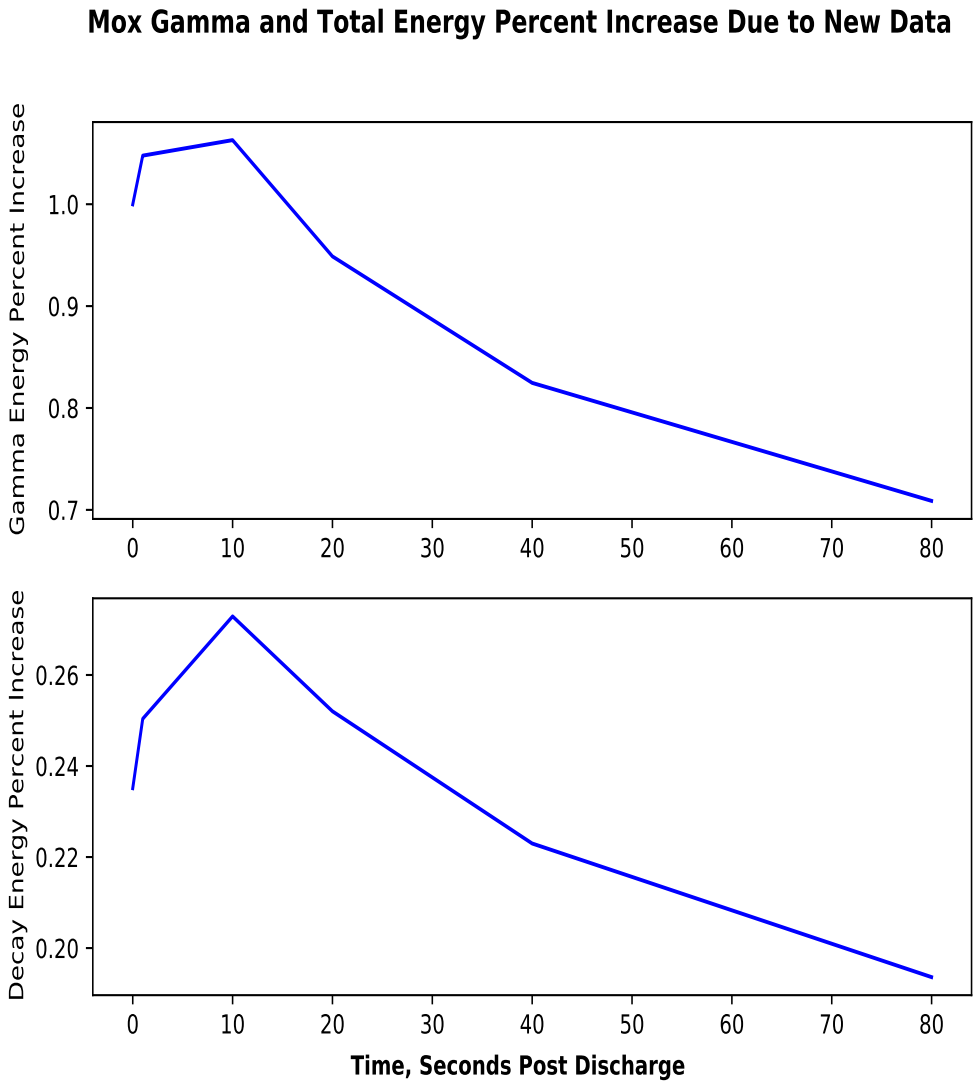

Figure 8.20: Change in the gamma and total decay heat that is attributable to ^{106}Mo and ^{106}Tc combined. The percent changes are larger for MOX fuel than for enriched uranium fuel, as there is more plutonium being burned.

Chapter 9

Discussion of Results

This section will discuss what the impacts of the results of this research are, as well as compare to previous works where possible. For ^{106}Mo, there exists previous theory work by P. Sarriguren and J. Pereira regarding ^{106}Mo shape deformation and Gamow-Teller strength [36]. For ^{106}Tc there is work by A. Algora et al regarding reactor decay heat, with one of the isotopes that they looked at being ^{106}Tc [41]. For this research's SCALE simulation results, the impact to the nuclear reactor community, and in particular, reactor/nuclear fuel simulation will be discussed.

9.1 Changes to Beta Feeding Intensities

The changes to beta feeding intensities will be broken down into changes to ^{106}Mo and ^{106}Tc. While there may be some overlap, ^{106}Mo's decay scheme was more incomplete with older data, and ^{106}Tc is produced more by fission of typical nuclear fuel, so the differences between the two warrant splitting them.

For ^{106}Mo, the beta feeding intensities largely shift from sub 400 keV feeding to an increase in the 465 keV level, and the establishment of a new level at 1318 keV, as well as

many tightly spaced pseudolevels above 2000 keV. These pseudolevels may have small feeding intensities, but they have large Gamow-Teller matrix elements. This information regarding Gamow-Teller strengths can be used to glean information about the nuclear structure of ^{106}Mo.

In addition to the effects of feeding shifts and new levels mentioned above, another discovery were the levels at 595, 618, and 634 keV. NNDC previously assigned the 595 and 618 keV levels to be individual gamma rays in cascade from the 672 and 736 keV levels, and the 634 was an unassigned gamma ray. Per fitting procedures outlined in this PhD research, the 595, 618, and 634 keV gamma rays are most likely levels, with their own cascades to lower energy levels. NNDC previously assigned large feedings to the 54 keV level, as well as ground state feeding, however, there appears to be no ground state feeding, and minimal feeding of the 54 keV level. Instead, this 54 keV level has other higher energy levels cascade through it. The net result is a large increase in average gamma ray energy, going from 515.6 keV to 910.4 keV, a 77% increase.

For ^{106}Tc, the beta feeding intensities shift from the 270 keV being significantly fed, and levels between 270 keV and 2239 keV being moderately fed in current NNDC data, to a lack of any significant direct beta feeding below 1700 keV. Instead, nearly all of the higher energy levels decay through the 270 keV level, as evidenced by the gamma-gamma coincidence spectra of MTAS experimental data. There are new levels around 4276 and 4585 keV, as well as many tightly spaced pseudolevels above 5000 keV. The average gamma energy is increased by $\approx 46\%$ compared to current NNDC values.

9.2 Comparison of ^{106}Mo Gamow-Teller Strength to Previous Work

As a comparison of this work, a brief presentation and discussion of work by P. Sarriguren will be conducted [36]. Work in Sarriguren's paper on β decay properties calculates theoretical shapes of Gamow-Teller strength for Mo and Zr isotopes, including ^{106}Mo, using quasiparticle random phase approximation (QRPA) methods. Calculations in that work account for effects such as quenching and nuclear deformation. Noted by Sarriguren is the existence of competition between shapes, with prolate, oblate, and spherical shapes competing and possibly coexisting [36].

The following figure 9.2 is directly from ref [36], and is presented to compare to this PhD research's calculations of Gamow-Teller strength distribution. Data analyzed as part of this PhD dissertation is overlaid in dark pink.

Comparing predictions from Sarriguren in figure 9.2, this PhD research's calculations of ^{106}Mo B_{GT} strength are indicative of an oblate deformation shape. The energies where spikes in Gamow-Teller strength occur coincide well with the energies predicted by Sarriguren. In particular, spikes occur around 465 and 1300 keV, which do not happen in the case of prolate deformation. This is a significant finding, as previous experimental data, which only measured beta decay fed levels up to 736 keV, seemed to indicate an oblate deformation shape, but was extremely limited by only observing levels far below the Q value. By utilizing TAS, beta decay feeding and corresponding B_{GT} strength for nuclear levels up to near Q_β have been observed. There is some disagreement on the scaling factor, however, this is possibly due to scaling factors already applied in work by Sarriguren. In his paper, he does not specify his scaling factors, and the nuclear lifetimes that he shows are more consistent with oblate deformation. While the match is not exact due to scaling, the end ΣB_{GT}

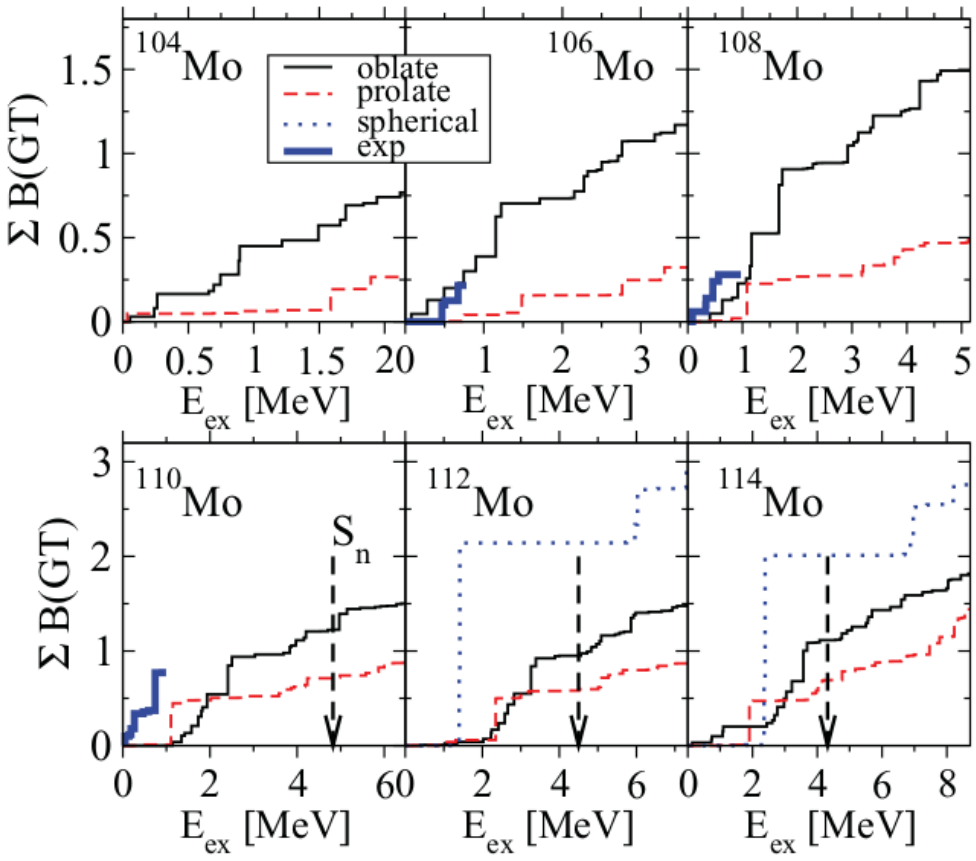

Figure 9.1: This figure shows work from Sarriguren regarding Mo isotopes and their Gamow-Teller strengths. The energy range selected by Sarriguren corresponds to the individual isotopes' Q_β values [36]. The thick blue line corresponds to previous NNDC data for ^{106}Mo.

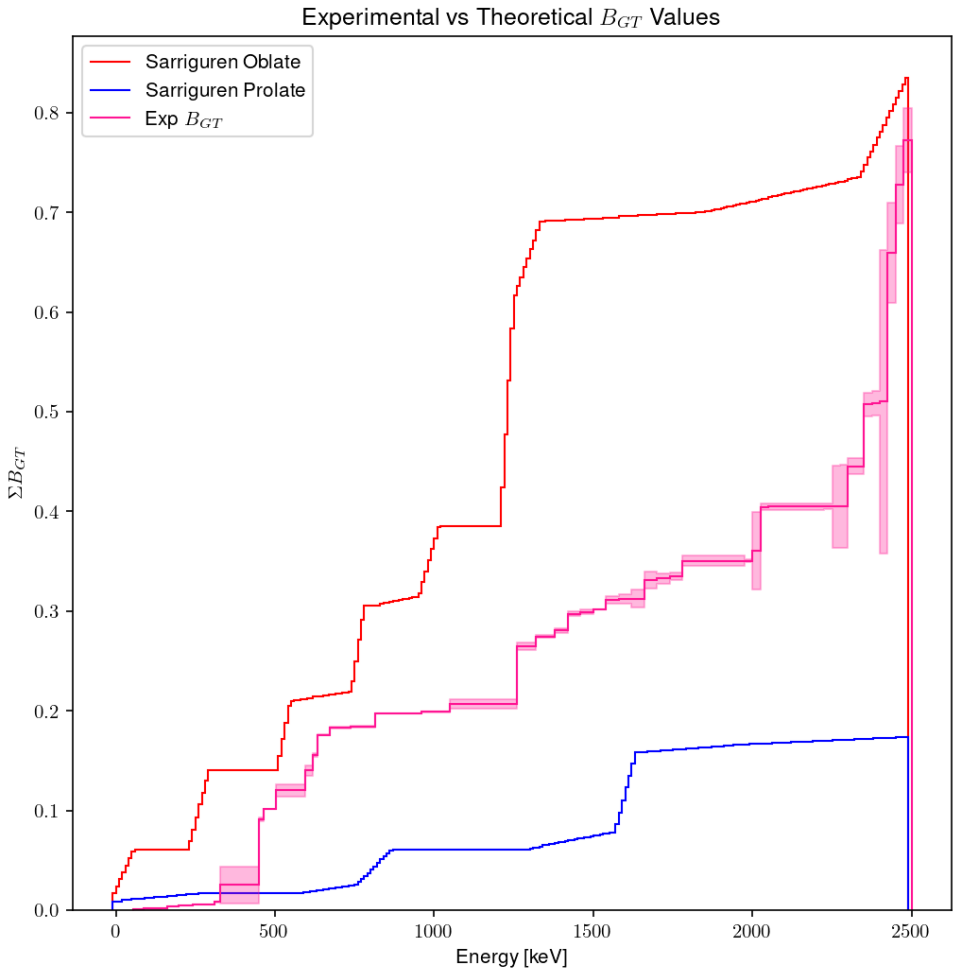

Figure 9.2: This figure shows work from Sarriguren regarding Mo isotopes and their Gamow-Teller strengths. The energy range selected by Sarriguren corresponds to the individual isotopes' Q_β values [36]. The summed Gamow-Teller strength distribution for ^{106}Mo is shown in dark pink. There is good agreement between the oblate shape distribution predicted by Sarriguren and the experimental data analyzed by this dissertation. Only B_{GT} up to 2500 keV is shown, due to very high uncertainties past this point.

value of around 0.8 at 2500 keV is in agreement, and the major peaks match for oblate deformation. This discovery may help to better understand nuclear deformation for neutron rich isotopes, and provide further validation of nuclear theory models.

Looking at figure 9.1, it is clear the advantage of using a TAS device such as MTAS. For even numbered Mo isotopes other than ^{106}Mo, the experimental data is either missing, or only covers a tiny fraction of the predicted range of values. The amount of information gleaned from the experimental campaign at ANL highlights the need for further TAS measurements of neutron rich fission fragments. If similar measurements were performed for the other isotopes of Mo, it would be possible to better validate theory models as shown by this PhD research.

9.3 Comparison of ^{106}Tc Average Gamma Energy to Previous Work

For the comparison of ^{106}Tc results, work by Algora et al will be discussed. Algora et al in their PRL publication calculate the average gamma energies for several isotopes using TAS methods. However, their TAS experimental setup is not identical to the MTAS device used for this research, and as such is suitable for comparison [41].

Table 9.1 is recreated from the aforementioned PRL and shows the ^{106}Tc average gamma energy. Algora et al calculate that the average gamma energy for ^{106}Tc is 3132(70) keV. Compared to this research's calculation result of 3239 $\pm$235 keV, the values are within uncertainty in agreement, validating Algorra et al's results. Algora et al's calculated value for the average beta energy of ^{106}Tc is 1457(30), compared to this research's value of 1397 $\pm$102 keV, again, within uncertainty in agreement. This research's higher gamma energy uncertainty is likely due to gamma rays above 5 MeV, which MTAS is able to detect, but the

Table 9.1: This table is a recreation from work by Algora et al. Listed are the nuclei that were studied by Algora et al, as well as the half-life, average gamma energies for ENDF and TAGS, and average beta energies for ENDF and TAGS.

Nuclide	$T_{1/2}$(s)	E_γ ENDF	E_γ TAGS	E_β ENDF	E_β TAGS
^{101}Nb	7.1(3)	270(22)	445(279)	1966(307)	1797(133)
^{105}Mo	35.6(16)	552(24)	2407(93)	1922(122)	1049(44)
^{102}Tc	5.28(15)	81(5)	106(23)	1945(16)	1935(11)
^{104}Tc	1098(18)	1890(31)	3229(24)	1595(75)	931(10)
^{105}Tc	456(6)	668(19)	1825(174)	1310(205)	764(81)
^{106}Tc	35.6(6)	2191(51)	3132(70)	1906(67)	1457(30)
^{107}Tc	21.2(2)	515(11)	1822(450)	2054(254)	1263(212)

statistics are relatively low. Thus, if there is high uncertainty in a high energy region, it will increase the overall average energy uncertainty.

These findings reaffirm the importance of TAS measurements of fission fragments, as TAS correctly calculates the average gamma and beta energies, allowing for more precise nuclear physics and engineering simulation codes.

9.4 Impacts of Increase to Decay Heat

For commercial nuclear reactor licensing and operation, correct knowledge of nuclear data is essential. An increase of ≈0.2% decay heat may seem to be a small change, but for licensing purposes, this change could result in millions of dollars in savings or extra expenditure. By having better understanding of nuclear fuel decay heat, it is possible to tighten tolerances on reactor fuel design, resulting in monetary savings. However, due to the increase of overall decay heat, it may be true that there is a need for slightly more heat dissipation, such as through higher flow volumes of liquid cooling.

Due to the relatively short half-lives of ^{106}Mo and ^{106}Tc, it is doubtful that the updated decay data would have an impact on long term storage, but it would be highly important for emergency reactor scenarios. Overall, this PhD research, along with previous work by Algora et al and other TAS work showcases the need for updates to older nuclear data sets. TAS measurements can provide higher quality data than was available in the 1960s and 1970s, when much of the current nuclear experimental data originated.

Chapter 10

Conclusions

This PhD research has resulted in multiple conclusions, ranging from nuclear physics information regarding two fission fragments with large cumulative fission yields, to the engineering impacts of those changes to nuclear decay data for ^{106}Mo and ^{106}Tc. Updated beta feeding intensities were determined for ^{106}Mo and ^{106}Tc, resulting in the discovery of multiple new levels for each isotope, among which are the 595, 618, 634, and 1318 keV levels for ^{106}Mo, and the 4276 and 4585 keV levels for ^{106}Tc, as well as many tightly spaced pseudolevels for both isotopes. B_{GT} values were calculated for ^{106}Mo and ^{106}Tc. Comparisons made to previous work by Sarriguren show that ^{106}Mo appears to be prolate in its deformation [36]. The average gamma energy for ^{106}Tc matches within uncertainty to previous work by Algora et al, confirming the updated beta feeding intensities for ^{106}Tc.

In terms of impacts to nuclear engineering, this PhD research showcases the need for more TAS measurements of nuclear fuel fission fragments. By applying the updated nuclear data for ^{106}Mo and ^{106}Tc to the ORNL SCALE reactor physics code, it was shown that there is a large shift to gamma-ray heating instead of beta particle heating, and there is an overall increase of $\approx$0.24% to total nuclear fuel decay heat immediately post-shutdown, owing to the shift of energy from the beta particles which share energy with the anti-neutrinos, to

gamma ray heating.

Chapter 11

My Contributions to This Research

- Participated in TAS experiments at Argonne National Laboratory in November 2019, February to March 2020, and June 2021, using the CARIBU facility and MTAS. Duties included performing data acquisition shifts, as well as general assistance to Dr. Rykaczewski and the ORNL team.
- Completed the MTAS PAASS data processor, including the implementation of ROOT output and linearly interpolated spectra calibration
- Cleaned and processed ^{106}Mo and ^{106}Tc data sets, using data from the 2020 experiments, as well as mass 105 data from 2019
- Worked on algorithm development for the prototype segmented plastic implant detector
- Developed GPU based deconvolution code based on previous work by P. Shuai and Cano-Ott [33, 30]
- Analyzed ^{106}Mo and ^{106}Tc data sets using Python3, PyROOT, and GEANT4. Identified multiple new levels for both isotopes, as well as changes to the decay paths. Updated beta feeding intensities were determined. ENSDF style level schemes can be seen in appendices A and B.

- Calculated Gamow-Teller strength distributions for ^{106}Mo and ^{106}Tc, as well as beta energy spectra. Compared the GT strength distribution of ^{106}Mo to the theoretical distribution calculated by Sarriguren [36].

- Implemented the nuclear decay data changes determined by this research into the ORNL SCALE code, and determined the impacts on nuclear reactor fuel caused by these data changes.

Bibliography

[1] D. de Frenne and A. Negret. Nuclear data sheets for a = 106. *Nuclear Data Sheets*, 109(4), 4 2008. 1

[2] Ian Gauld and J. Ryman. Nuclide importance to criticality safety, decay heating, and source terms related to transport and interim storage of high-burnup lwr fuel. 01 2001. 1

[3] J.C. Hardy, L.C. Carraz, B. Jonson, and P.G. Hansen. The essential decay of pandemonium: A demonstration of errors in complex beta-decay schemes. *Physics Letters B*, 71:307–310, 11 1977. 1, 13

[4] C. L. Duke, P. G. Hansen, O. B. Nielsen, G. Rudstam, and Switzerland Isolde Collaboration, Cern Geneva. Strength-function phenomena in electron-capture beta decay. *Nuclear Physics A*, 151(3):609–633, 1970. 3

[5] M Karny, J M Nitschke, L F Archambault, K H Burkard, D Cano-Ott, M Hellström, W Hüller, R Kirchner, S J Lewandowski, E Roeckl, and A Sulik. Coupling a total absorption spectrometer to the GSI on-line mass separator. page 14 p, Dec 1996. 3

[6] Richard C. Pardo, Guy Savard, and Robert V. F. Janssens. Atlas with caribu: A laboratory portrait. *Nuclear Physics News*, 26(1):5–11, 2016. 3, 24, 27

[7] Andreas Klöckner, Nicolas Pinto, Yunsup Lee, B. Catanzaro, Paul Ivanov, and Ahmed Fasih. PyCUDA and PyOpenCL: A Scripting-Based Approach to GPU Run-Time Code Generation. *Parallel Computing*, 38(3):157–174, 2012. 3

[8] W. A. Wieselquist, R. A. Lefebvre, and M. A. Jessee. *SCALE Code System, ORNL/TM-2005/39, Version 6.2.4*. Oak Ridge National Laboratory, 2020. 3, 56, 58

[9] A. Jokinen, T. Enqvist, P.P. Jauho, M. Leino, J.M. Parmonen, H. Penttilä, J. Äystö, and K. Eskola. Beta decay of 108mo and of neighbouring even mo-isotopes. *Nuclear Physics A*, 584(3):489–508, 1995. 6, 8, 68

[10] J. Stachel, N. Kaffrell, N. Trautmann, K. Broden, G. Skarnemark, and D. Eriksen. The collective structure of ^{106,108}ru. *Z.Phys.*, A316:105, 1984. 6, 9

[11] K. Sümmerer, N. Kaffrell, E. Stender, N. Trautmann, K. Brodén, G. Skarnemark, T. Björnstad, I. Haldorsen, and J.A. Maruhn. Levels in 106ru and 108ru. *Nuclear Physics A*, 339(1):74–88, 1980. 6, 7, 9

[12] G. Tittel. *Zerfallseigenschaften Kurzlebiger Neutronenreicher Molybdan-Isotope*. PhD thesis, Johannes Gutenberg-Universitat, Mainz, 1980. 6, 8

[13] J. Ärje, J. Äystö, H. Hyvönen, P. Taskinen, V. Koponen, J. Honkanen, K. Valli, A. Hautojärvi, and K. Vierinen. The ion guide isotope separator on-line, igisol. *Nuclear Instruments and Methods in Physics Research Section A: Accelerators, Spectrometers, Detectors and Associated Equipment*, 247(3):431–437, 1986. 6

[14] Kathleen Goetz. *Total Absorption Spectroscopy of Neutron Rich Nuclei Across the N=50 Neutron Shell Closure*. PhD thesis, University of Tennessee, 2017. 10, 11

[15] N. Tsoulfanidis and S. Landsberger. *Measurement and Detection of Radiation*. CRC Press, Taylor & Francis Group, 2015. 12, 13, 14

[16] E.J Morton, R.J Clark, and C Crowley. Factors affecting the spectral resolution of scintillation detectors. *Nuclear Instruments and Methods in Physics Research Section A: Accelerators, Spectrometers, Detectors and Associated Equipment*, 422(1):155–158, 1999. 13

[17] G.F. Knoll. *Radiation Detection and Measurement*. Wiley, 2010. 13

[18] B. C. Rasco. Total absorption spectroscopy and its influence on decay heat and predicted reactor ν e fluxes, 2016. 16, 19, 44, 48

[19] M. Karny, K. P. Rykaczewski, A. Fijalkowska, B. C. Rasco, M. Wolinska-Cichocka, R. K. Grzywacz, K. C. Goetz, D. Miller, and E. F. Zganjar. Modular total absorption spectrometer. *NUCLEAR INSTRUMENTS & METHODS IN PHYSICS RESEARCH SECTION A-ACCELERATORS SPECTROMETERS DETECTORS AND ASSOCIATED EQUIPMENT*, 836:83–90, NOV 11 2016. 16, 17, 20, 42

[20] B. C. Rasco, M. Wolinska-Cichocka, A. Fijalkowska, K. P. Rykaczewski, M. Karny, R. K. Grzywacz, K. C. Goetz, C. J. Gross, D. W. Stracener, E. F. Zganjar, J. C. Batchelder, J. C. Blackmon, N. T. Brewer, S. Go, B. Heffron, T. King, J. T. Matta, K. Miernik, C. D. Nesaraja, S. V. Paulauskas, M. M. Rajabali, E. H. Wang, J. A. Winger, Y. Xiao, and C. J. Zachary. Decays of the three top contributors to the reactor (nu)over-bar(e) high-energy spectrum, rb-92, (96)gsy, and cs-142, studied with total absorption spectroscopy. *PHYSICAL REVIEW LETTERS*, 117(9), AUG 22 2016. 19, 42

[21] K. Rykaczewski. Personal Communication, 2022. 24, 28

[22] XIA. *Pixie-16 User Manual*. 31057 Genstar Rd Hayward, CA 94544 USA, 2018 online. 24, 26

[23] D Santiago. ANL CARIBU Website and Rates. https://www.anl.gov/atlas/caribu-beams. Accessed: 2022-01-27. 27

[24] M. Wolińska-Cichocka, K.P. Rykaczewski, A. Fijałkowska, M. Karny, R.K. Grzywacz, C.J. Gross, J.W. Johnson, B.C. Rasco, and E.F. Zganjar. Modular total absorption spectrometer at the hribf (ornl, oak ridge). *Nuclear Data Sheets*, 120:22–25, 2014. 25

[25] University of Tennessee Knoxville, Low Energy Nuclear Physics Group. Pixie acquisition and analysis software suite PAASS, 2009. 31

[26] R. Brun, F. Rademakers, et al. Root - an object oriented data analysis framework. https://root.cern/releases/release-62206/, December 2020. 32

[27] A. Fijałkowska, M. Karny, K.P. Rykaczewski, M. Wolińska-Cichocka, R. Grzywacz, C.J. Gross, J.W. Johnson, B.C. Rasco, E.F. Zganjar, D.W. Stracener, C. Jost, K.C. Goetz, R. Goans, E. Spejewski, L. Cartegni, M. Madurga, K. Miernik, D. Miller, S.W. Padgett, S.V. Paulauskas, M. Al-Shudifat, J.H. Hamilton, and A.V. Ramayya. First results from the modular total absorption spectrometer at the hribf. *Nuclear Data Sheets*, 120:26–29, 2014. 42

[28] B.C. Rasco, A. Fijałkowska, M. Karny, K.P. Rykaczewski, M. Wolińska-Cichocka, R. Grzywacz, and K.C. Goetz. The nonlinear light output of nai(tl) detectors in the modular total absorption spectrometer. *Nuclear Instruments and Methods in Physics Research Section A: Accelerators, Spectrometers, Detectors and Associated Equipment*, 788:137–145, 2015. 42

[29] J. Hadamard. Sur les problemes aux derivees partielles et leur signification physique. pages 49–52, 1902. 46

[30] J.L. Tain and D. Cano-Ott. Algorithms for the analysis of β-decay total absorption spectra. *Nuclear Instruments and Methods in Physics Research Section A: Accelerators, Spectrometers, Detectors and Associated Equipment*, 571(3):728–738, 2007. 46, 49, 102

[31] LB LUCY. Iterative technique for rectification of observed distributions. *ASTRONOMICAL JOURNAL*, 79(6):745–754, 1974. 46, 48, 49

[32] P. Shuai, B. C. Rasco, K. P. Rykaczewski, A. Fijałkowska, M. Karny, M. Woli ńska Cichocka, R. K. Grzywacz, C. J. Gross, D. W. Stracener, E. F. Zganjar, J. C. Batchelder, J. C. Blackmon, N. T. Brewer, S. Go, M. Cooper, K. C. Goetz, J. W. Johnson, C. U. Jost, T. T. King, J. T. Matta, J. H. Hamilton, A. Laminack, K. Miernik, M. Madurga, D. Miller, C. D. Nesaraja, S. Padgett, S. V. Paulauskas, M. M. Rajabali, T. Ruland, M. Stepaniuk, E. H. Wang, and J. A. Winger. Determination of β-decay feeding patterns of ^{88}Rb and ^{88}Kr using the modular total absorption spectrometer at ornl hribf. *Phys. Rev. C*, 105:054312, May 2022. 46

[33] P. Shuai. Preliminary results of data analysis of ^{88}kr β-decay, 2021. 49, 102

[34] K.S. Krane. *Introductory Nuclear Physics*. Wiley, 1991. 51, 74

[35] NNDC. Logft utility code. https://github.com/IAEA-NSDDNetwork/LOGFT, 2016. 51

[36] P. Sarriguren and J. Pereira. β-decay properties of neutron-rich zr and mo isotopes. *Physical Review C*, 81(6), jun 2010. 51, 92, 94, 95, 96, 100, 103

[37] S.S.M. Wong. *Introductory Nuclear Physics*. A Wiley-Interscience publication. Wiley, 1998. 52

[38] Leendert Hayen, Nathal Severijns, Kazimierz Bodek, Dagmara Rozpedzik, and Xavier Mougeot. High precision analytical description of the allowed β spectrum shape. *Reviews of Modern Physics*, 90(1), mar 2018. 53

[39] L. Hayen and N. Severijns. Beta spectrum generator: High precision allowed β spectrum shapes. *Computer Physics Communications*, 240:152–164, jul 2019. 53, 79

[40] *Status and Advances in MOX Fuel Technology*. Number 415 in Technical Reports Series. INTERNATIONAL ATOMIC ENERGY AGENCY, Vienna, 2003. 57, 86

[41] A. Algora, D. Jordan, J. L. Taín, B. Rubio, J. Agramunt, A. B. Perez-Cerdan, F. Molina, L. Caballero, E. Nácher, A. Krasznahorkay, M. D. Hunyadi, J. Gulyás, A. Vitéz, M. Csatlós, L. Csige, J. Äysto, H. Penttilä, I. D. Moore, T. Eronen, A. Jokinen, A. Nieminen, J. Hakala, P. Karvonen, A. Kankainen, A. Saastamoinen, J. Rissanen, T. Kessler, C. Weber, J. Ronkainen, S. Rahaman, V. Elomaa, S. Rinta-Antila, U. Hager, T. Sonoda, K. Burkard, W. Hüller, L. Batist, W. Gelletly, A. L. Nichols, T. Yoshida, A. A. Sonzogni, and K. Peräjärvi. Reactor decay heat in ^{239}Pu: Solving the γ discrepancy in the 4–3000-s cooling period. *Phys. Rev. Lett.*, 105:202501, Nov 2010. 92, 97

Appendices

A Tc-106 Decay Scheme (ENSDF Style)

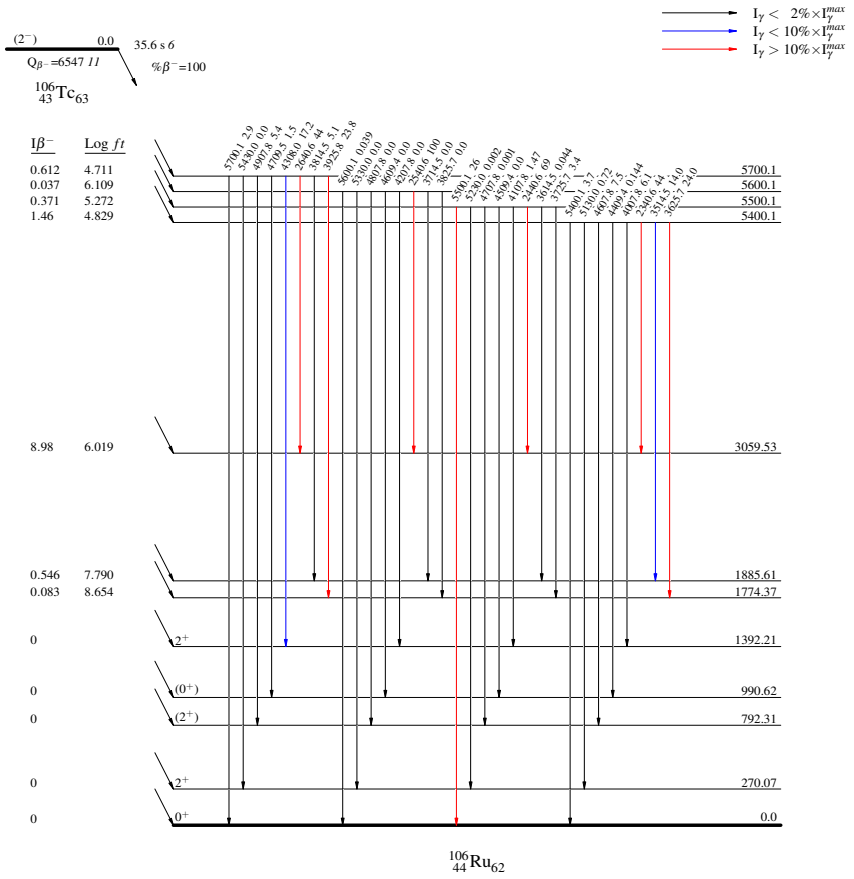

Figure 11.1: This figure shows the 1st part of the ^{106}Tc level scheme. Note that all gammas being emitted from levels are normalized to 100%.

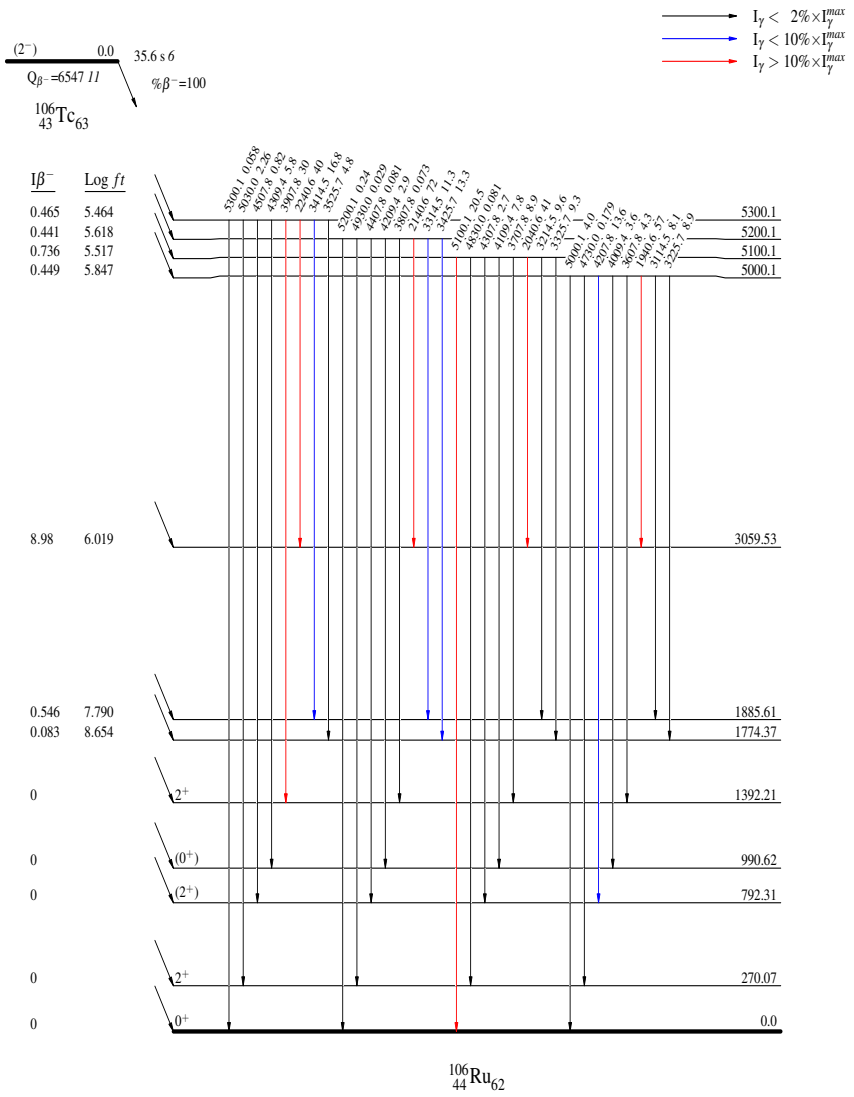

Figure 11.2: This figure shows the 2nd part of the ^{106}Tc level scheme. Note that all gammas being emitted from levels are normalized to 100%.

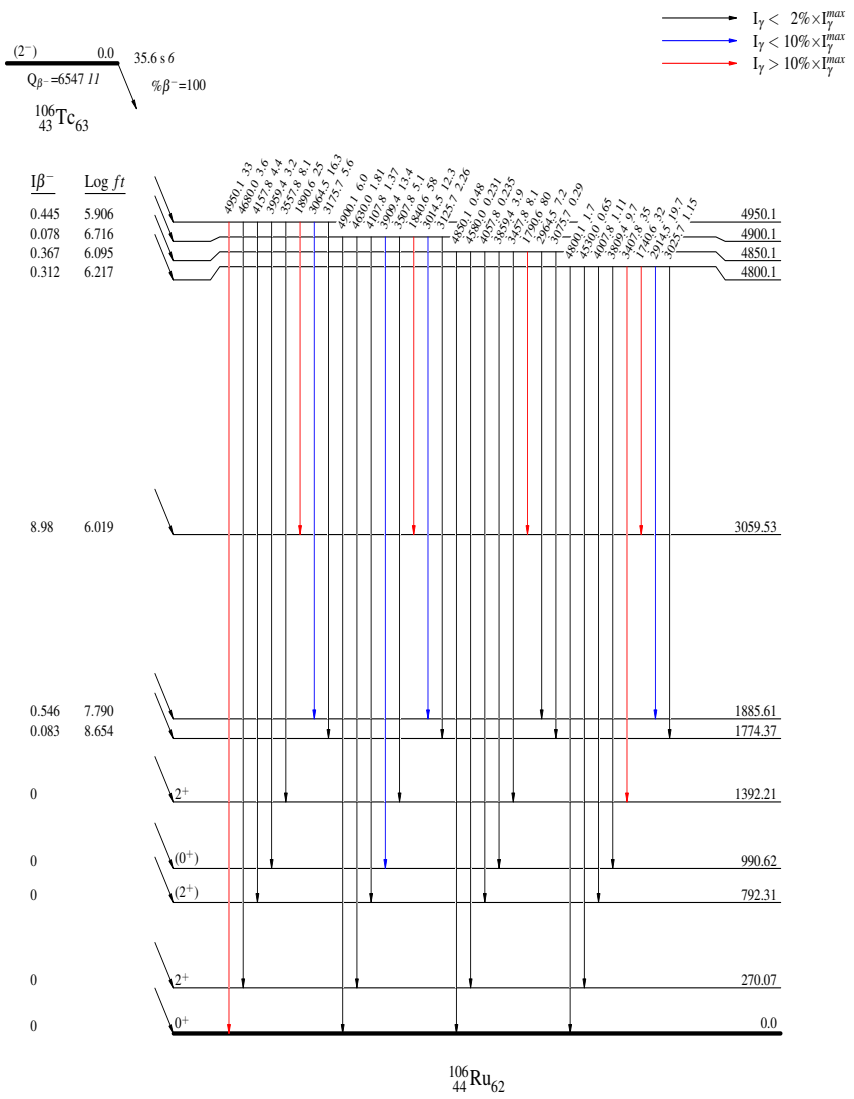

Figure 11.3: This figure shows the 3rd part of the ^{106}Tc level scheme. Note that all gammas being emitted from levels are normalized to 100%.

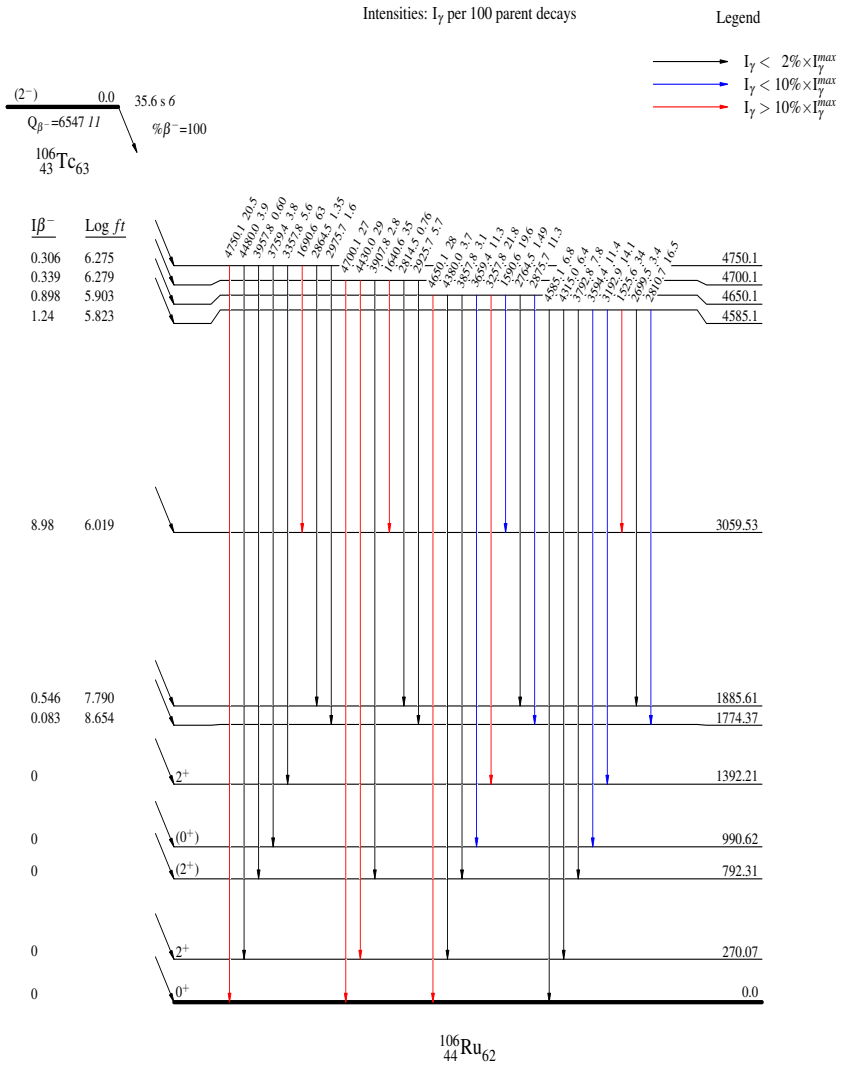

Figure 11.4: This figure shows the 4th part of the ^{106}Tc level scheme. Note that all gammas being emitted from levels are normalized to 100%.

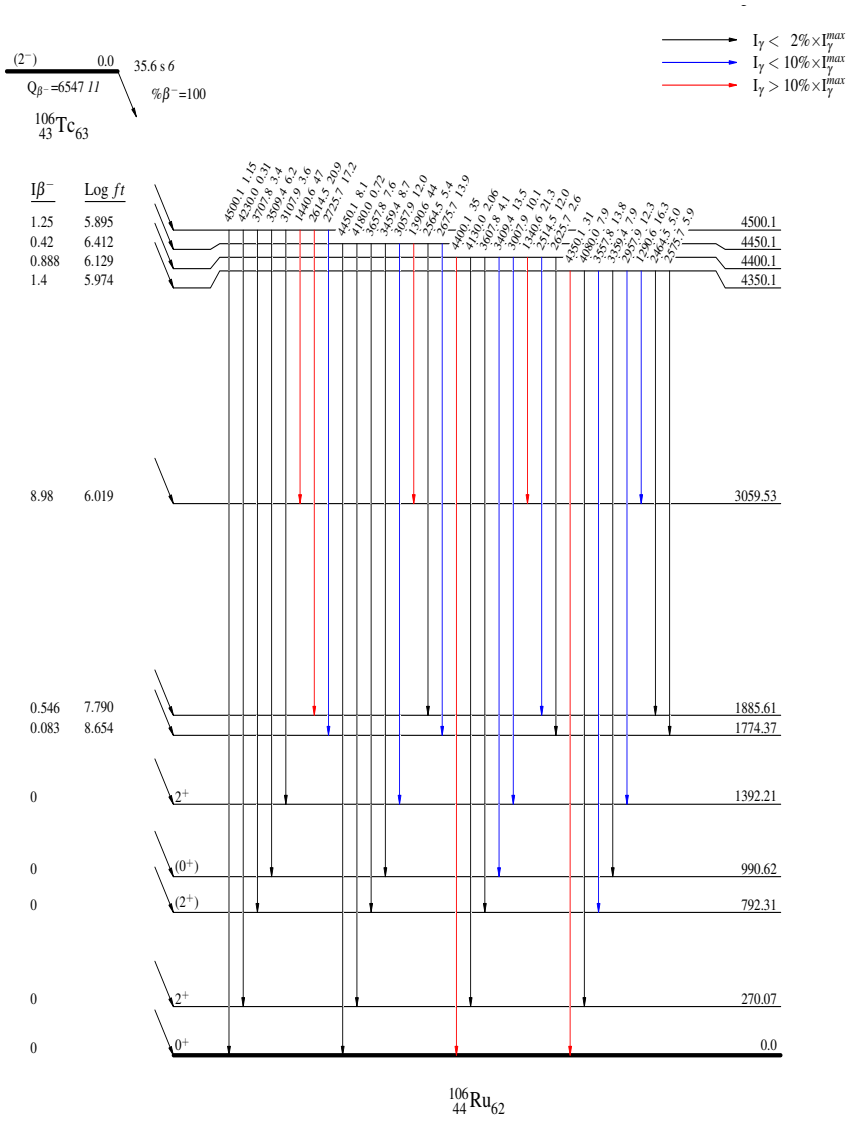

Figure 11.5: This figure shows the 5th part of the ^{106}Tc level scheme. Note that all gammas being emitted from levels are normalized to 100%.

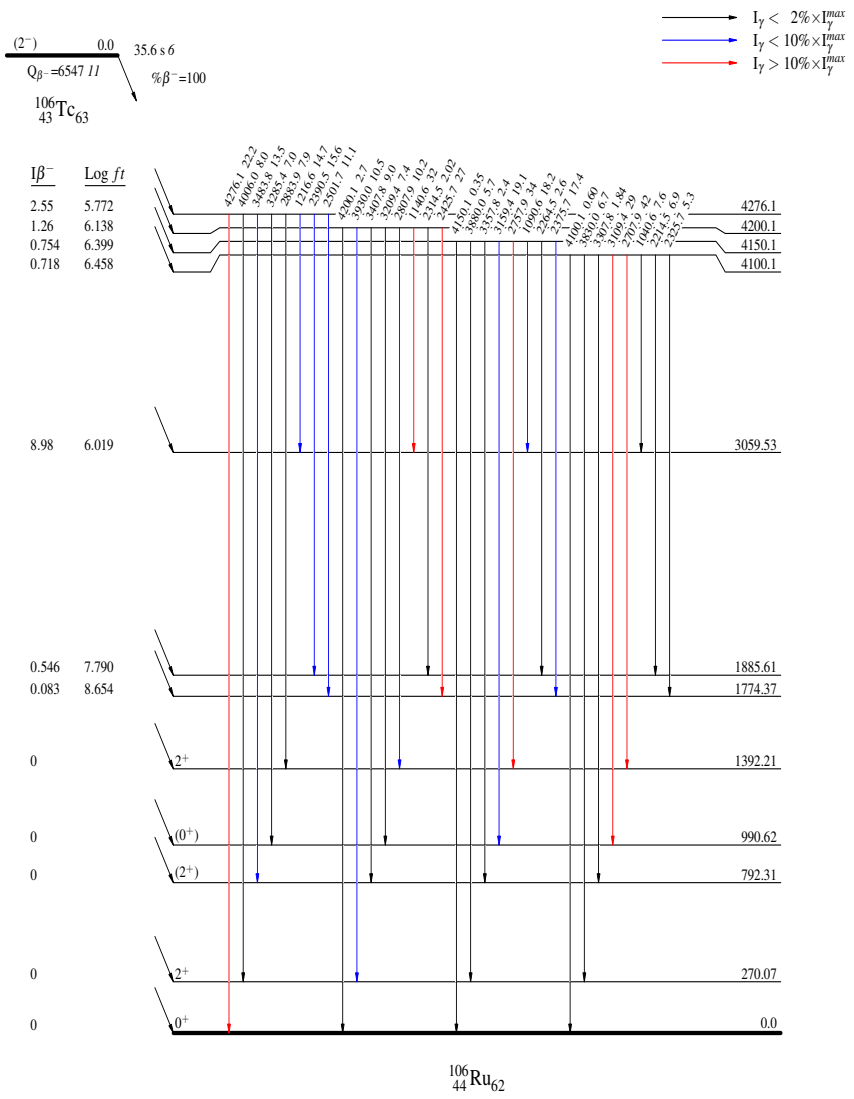

Figure 11.6: This figure shows the 6th part of the ^{106}Tc level scheme. Note that all gammas being emitted from levels are normalized to 100%.

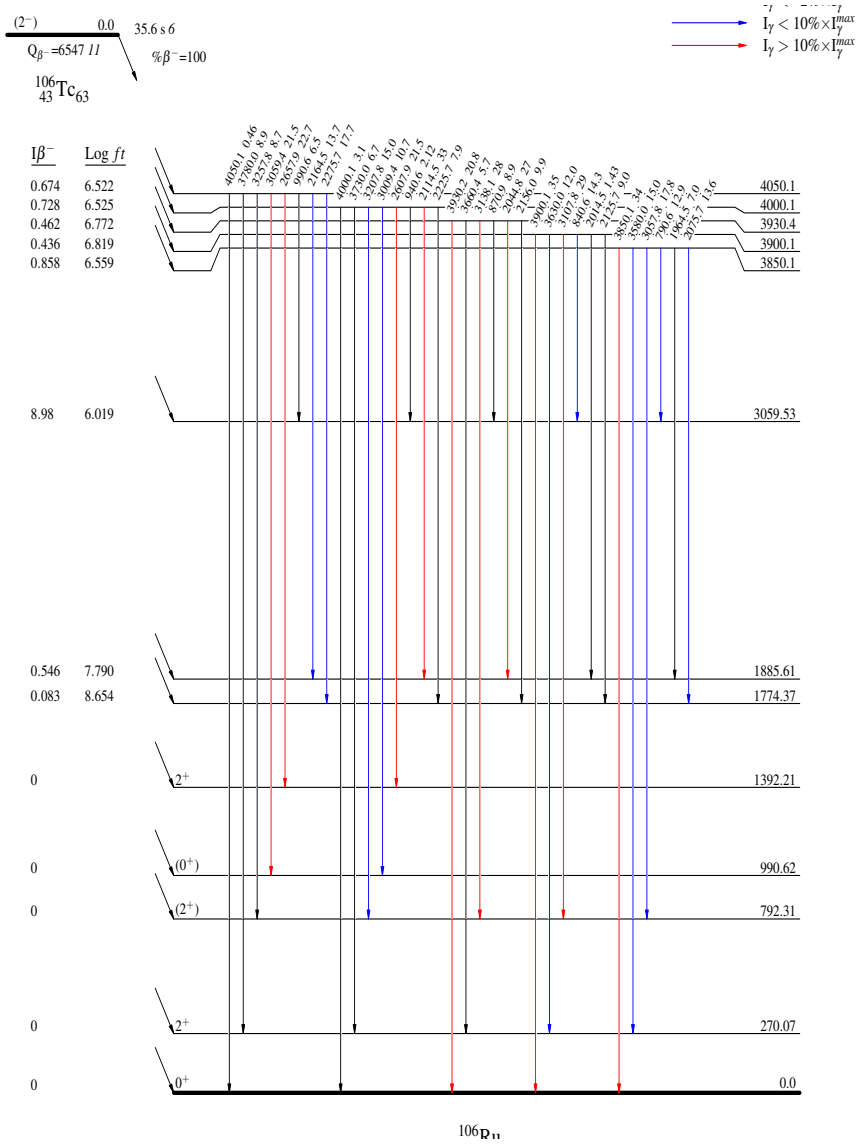

Figure 11.7: This figure shows the 7th part of the ^{106}Tc level scheme. Note that all gammas being emitted from levels are normalized to 100%.

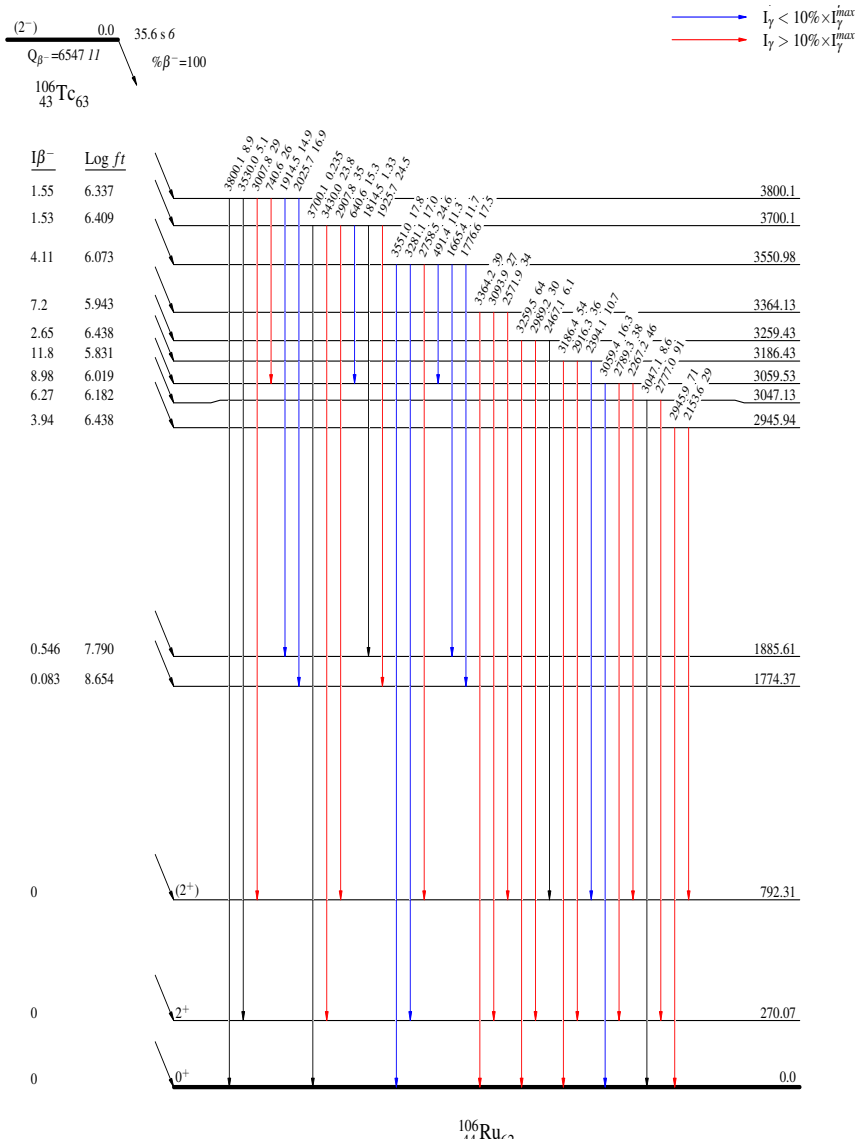

Figure 11.8: This figure shows the 8th part of the ^{106}Tc level scheme. Note that all gammas being emitted from levels are normalized to 100%.

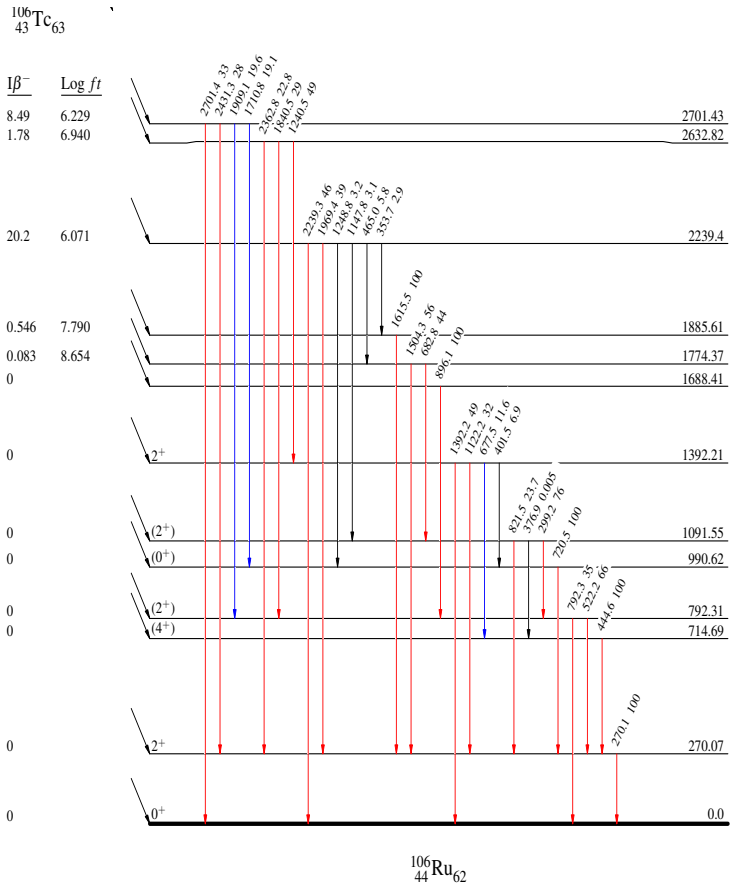

Figure 11.9: This figure shows the 9th part of the ^{106}Tc level scheme. Note that all gammas being emitted from levels are normalized to 100%.

B Mo-106 Decay Scheme (ENSDF Style)

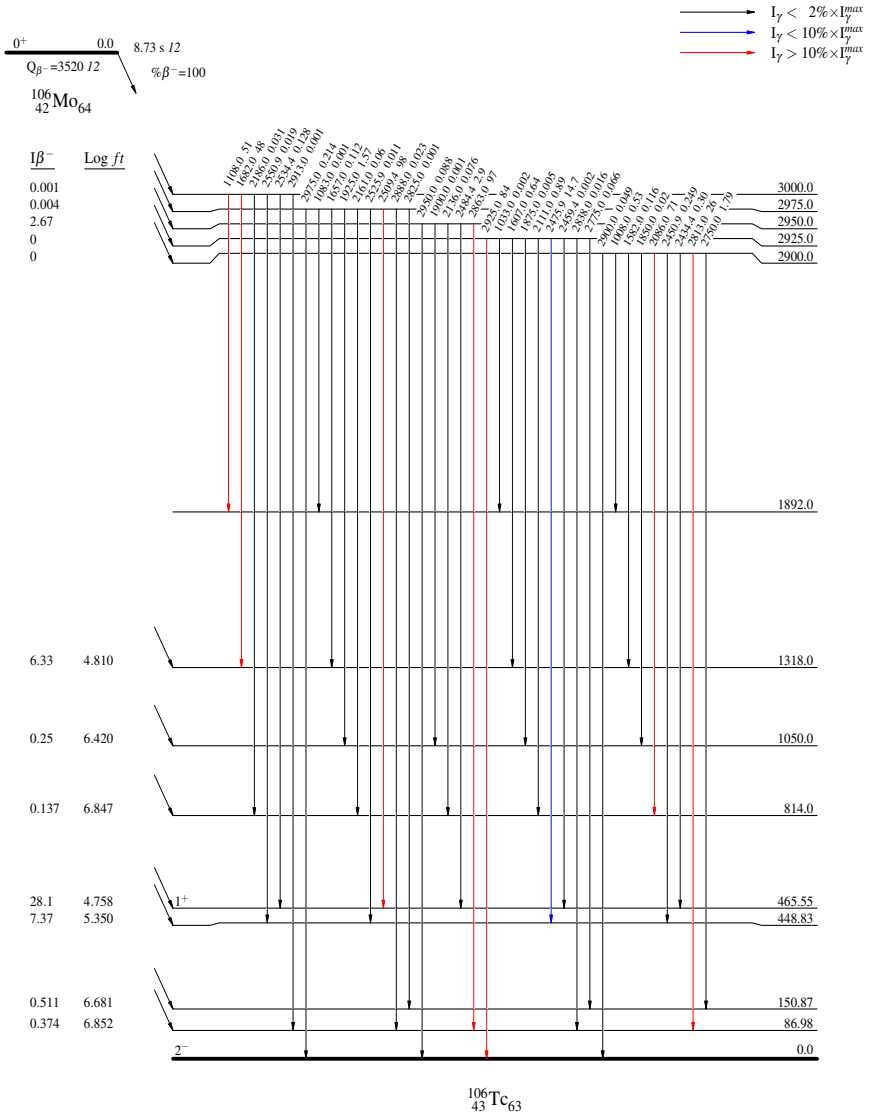

Figure 11.10: This figure shows the 2nd part of the ^{106}Mo level scheme. Note that all gammas being emitted from levels are normalized to 100%.

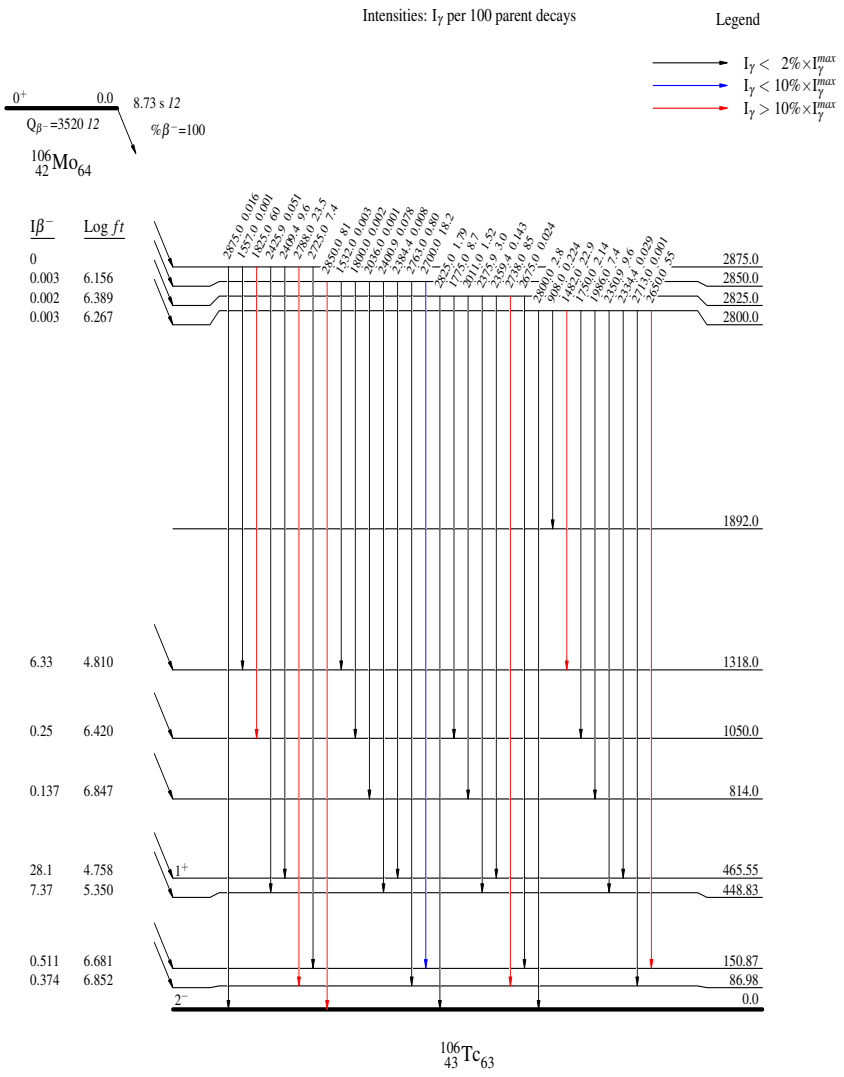

Figure 11.11: This figure shows the 2nd part of the ^{106}Mo level scheme. Note that all gammas being emitted from levels are normalized to 100%.

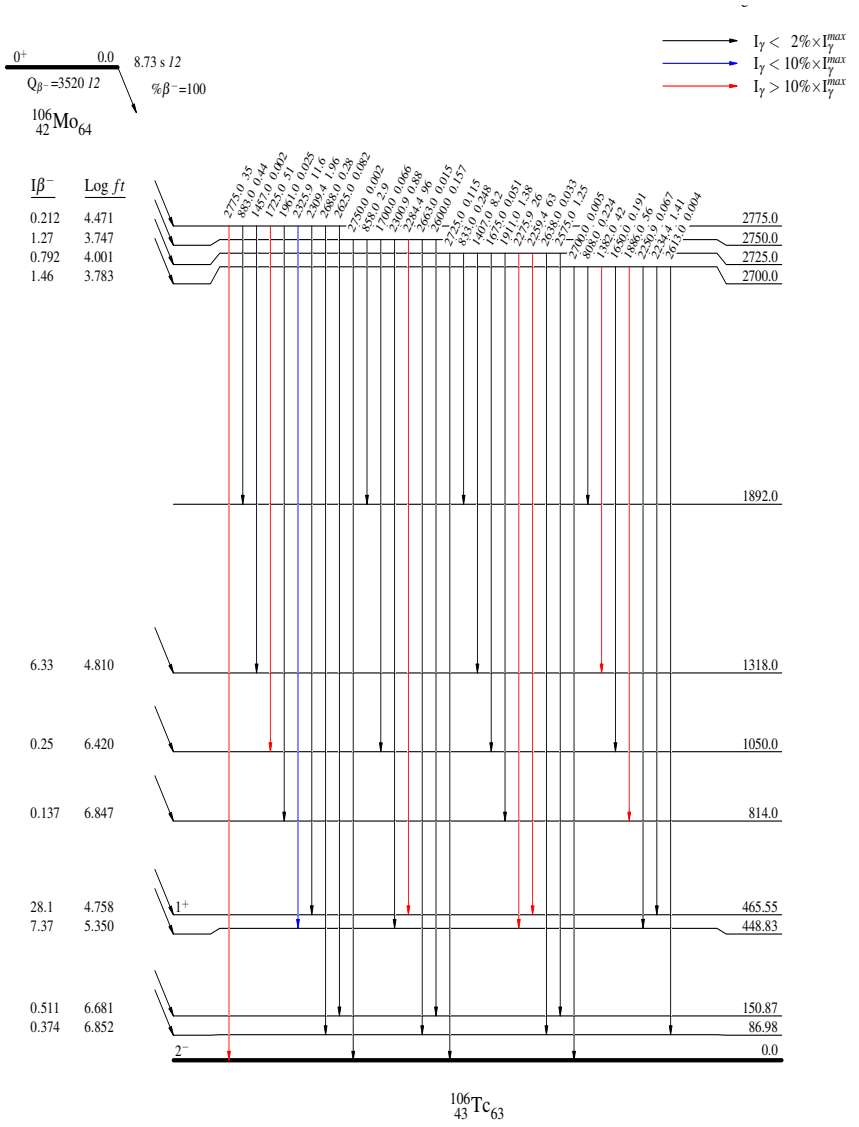

Figure 11.12: This figure shows the 3rd part of the ^{106}Mo level scheme. Note that all gammas being emitted from levels are normalized to 100%.

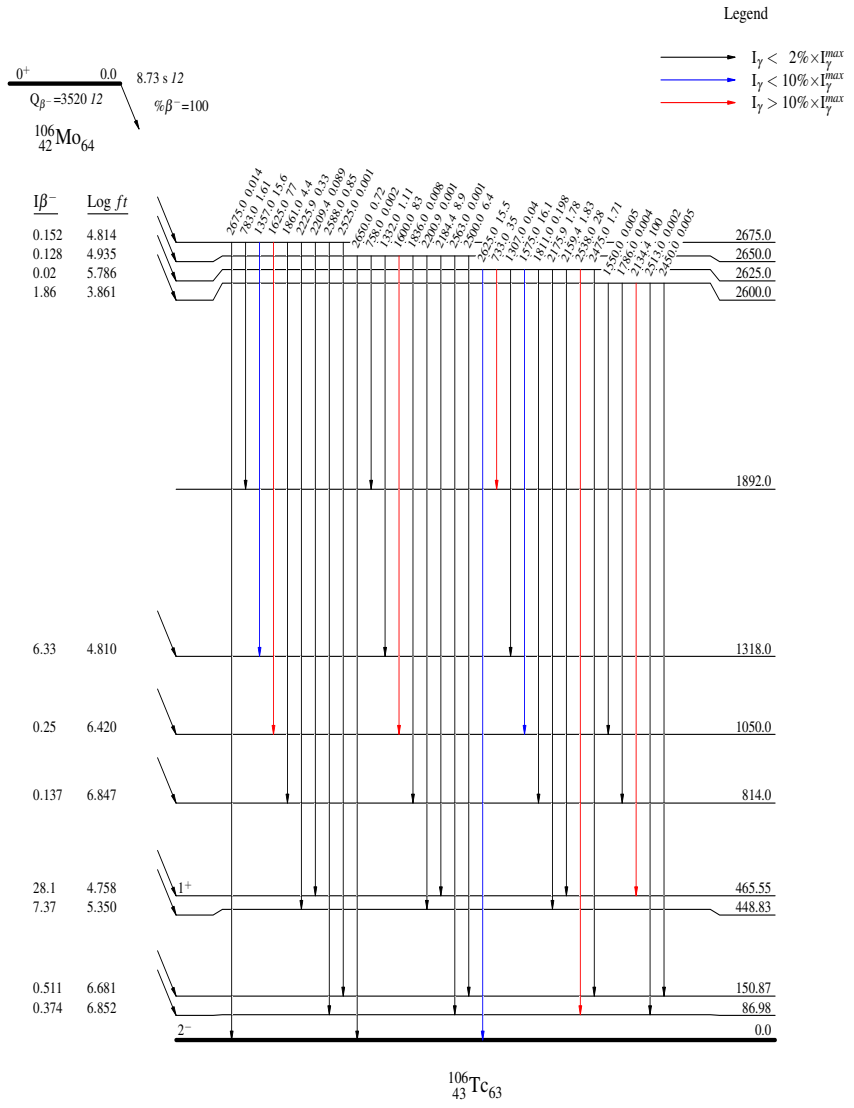

Figure 11.13: This figure shows the 4th part of the ^{106}Mo level scheme. Note that all gammas being emitted from levels are normalized to 100%.

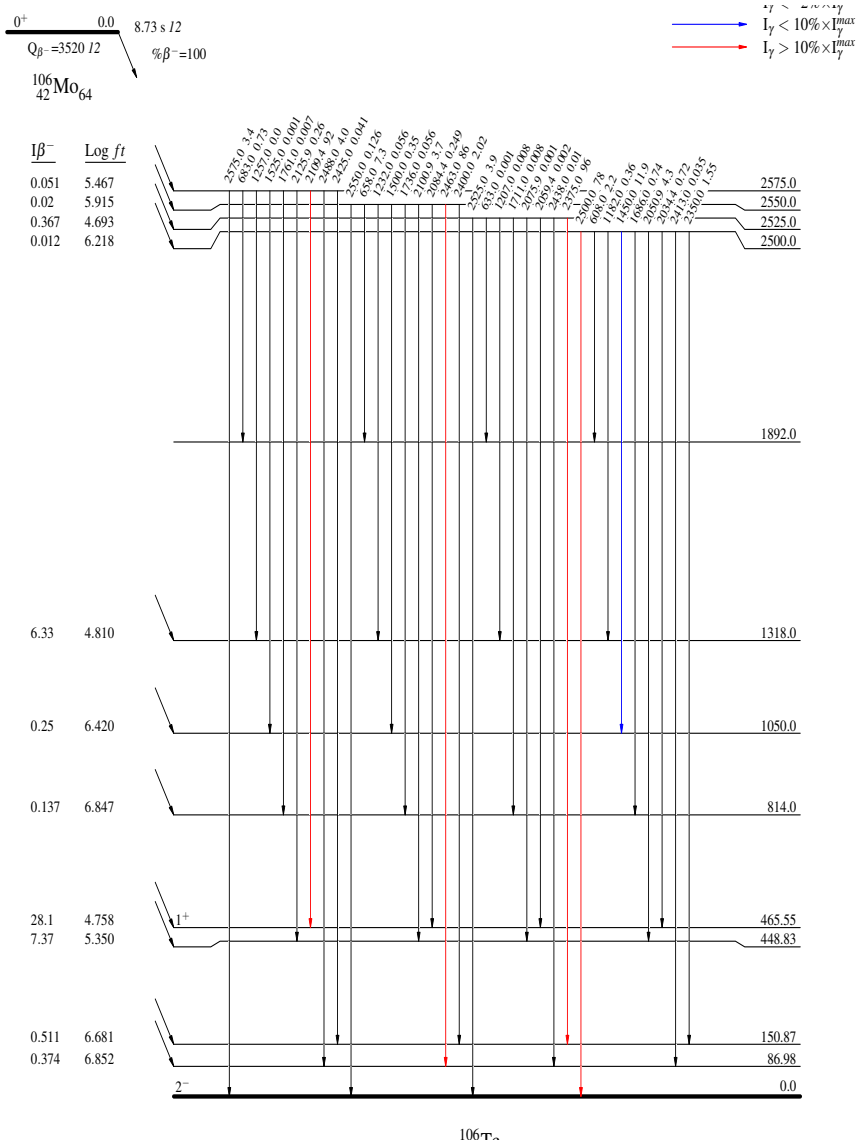

Figure 11.14: This figure shows the 5th part of the ^{106}Mo level scheme. Note that all gammas being emitted from levels are normalized to 100%.

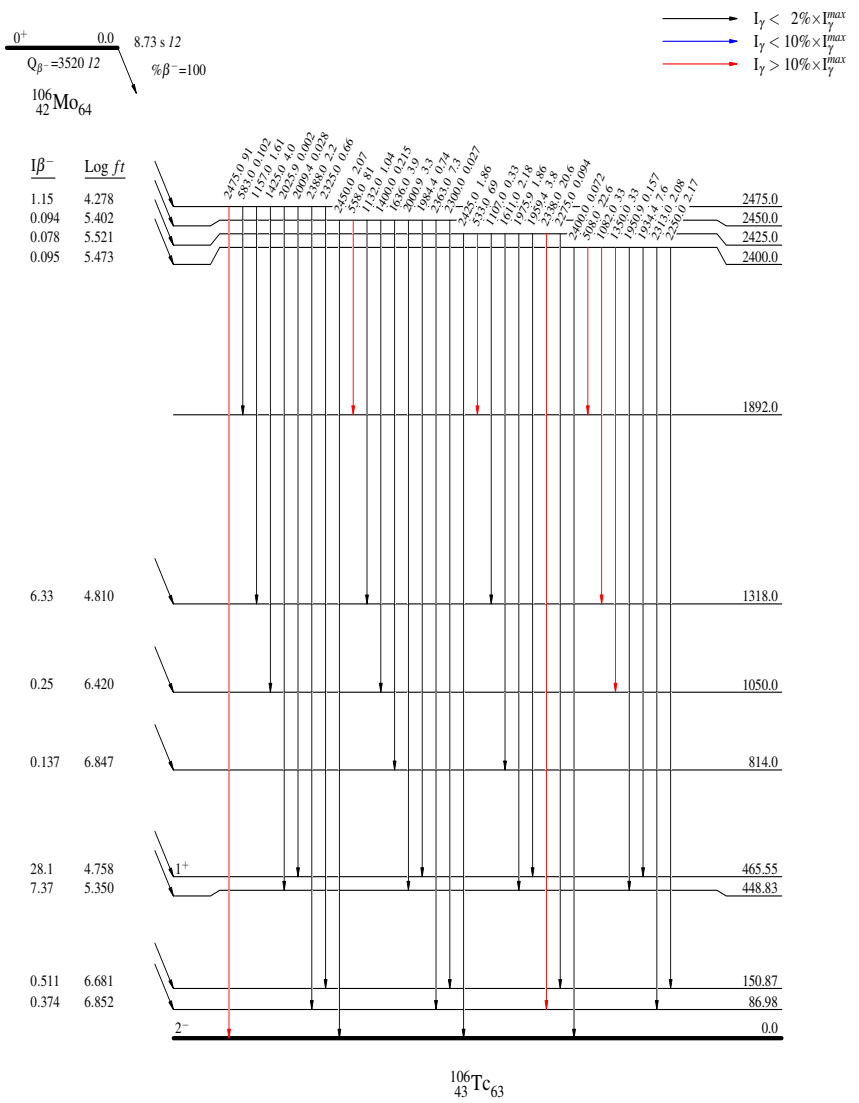

Figure 11.15: This figure shows the 6th part of the ^{106}Mo level scheme. Note that all gammas being emitted from levels are normalized to 100%.

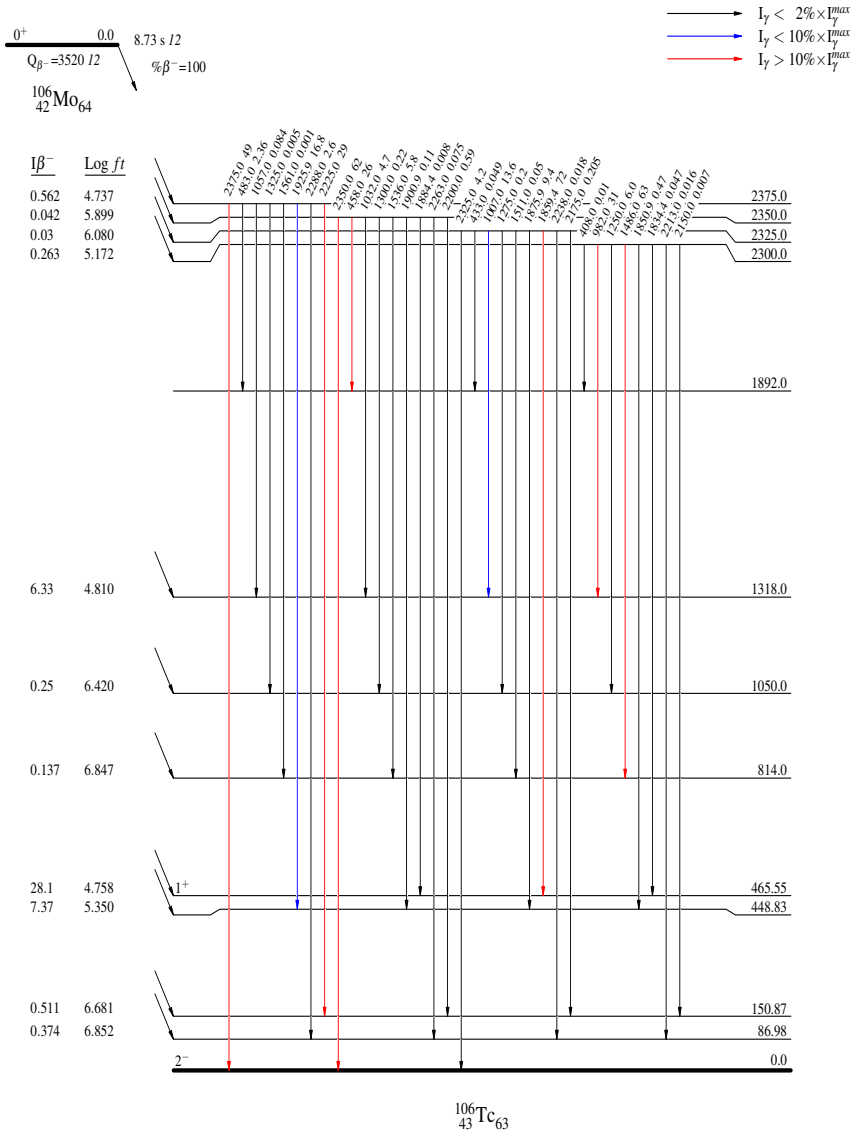

Figure 11.16: This figure shows the 7th part of the ^{106}Mo level scheme. Note that all gammas being emitted from levels are normalized to 100%.

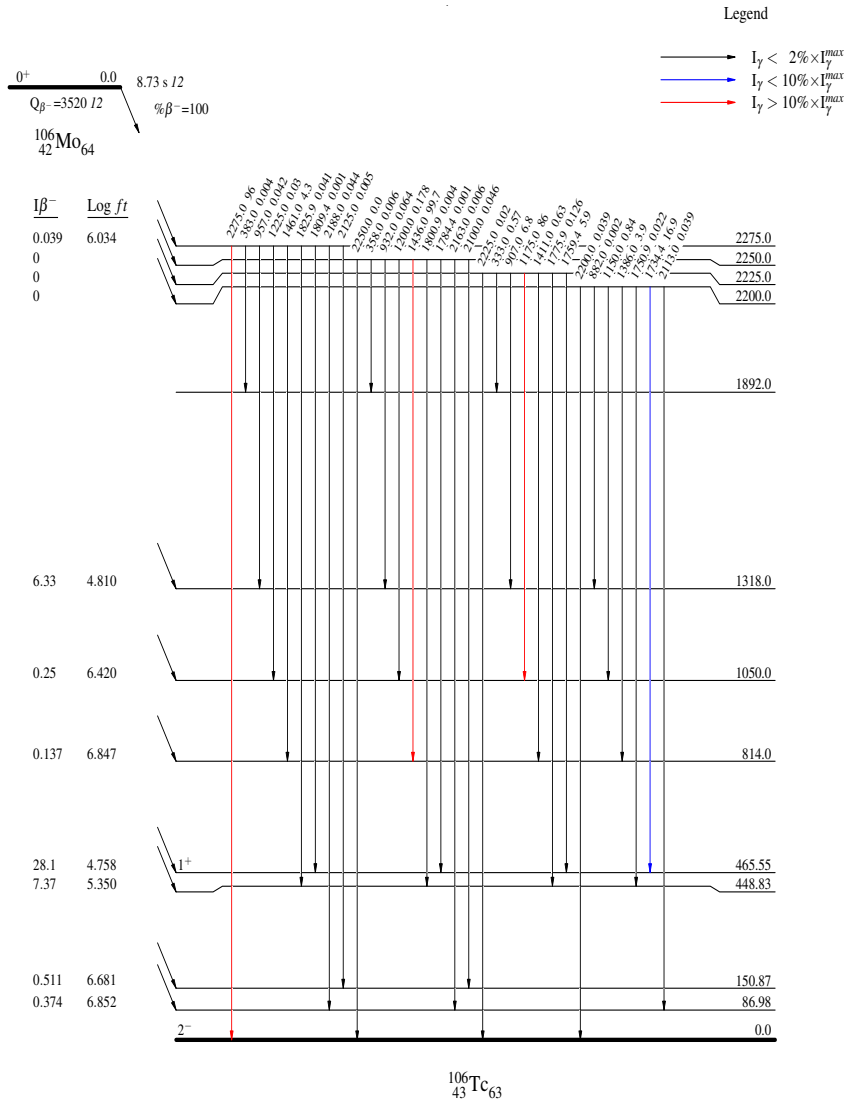

Figure 11.17: This figure shows the 8th part of the ^{106}Mo level scheme. Note that all gammas being emitted from levels are normalized to 100%.

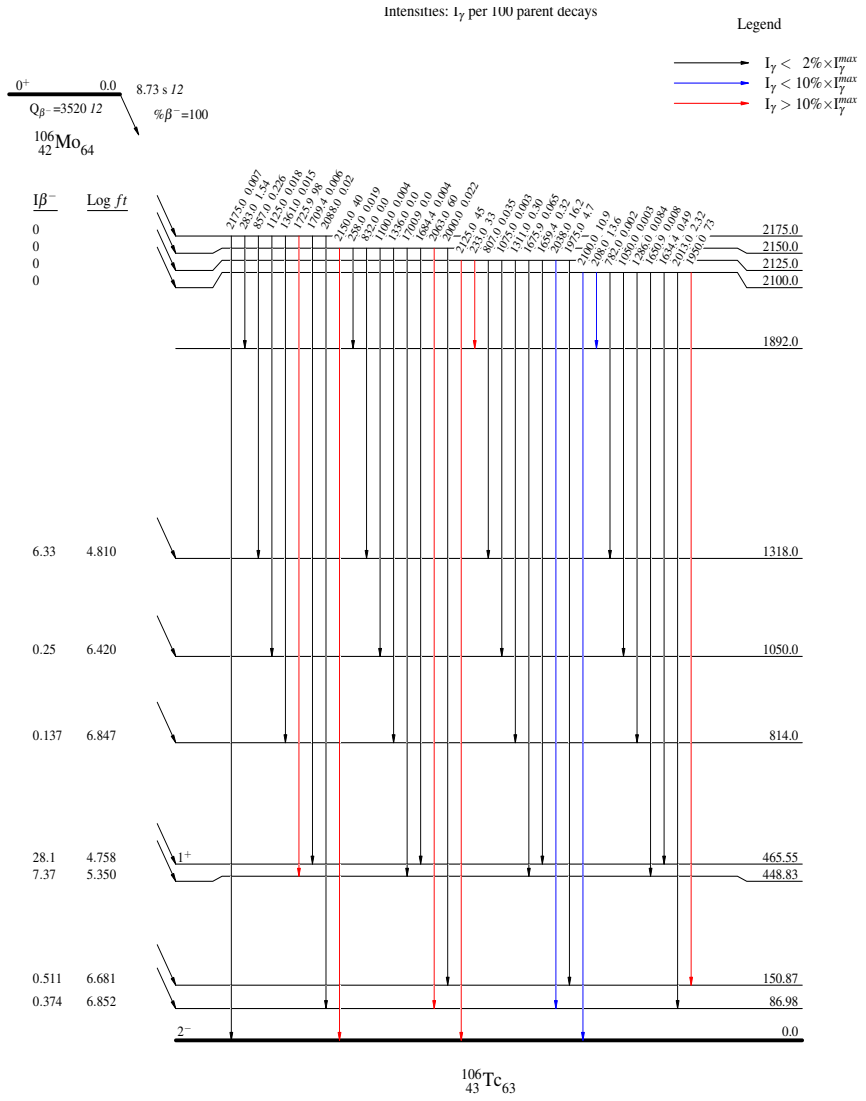

Figure 11.18: This figure shows the 9th part of the ^{106}Mo level scheme. Note that all gammas being emitted from levels are normalized to 100%.

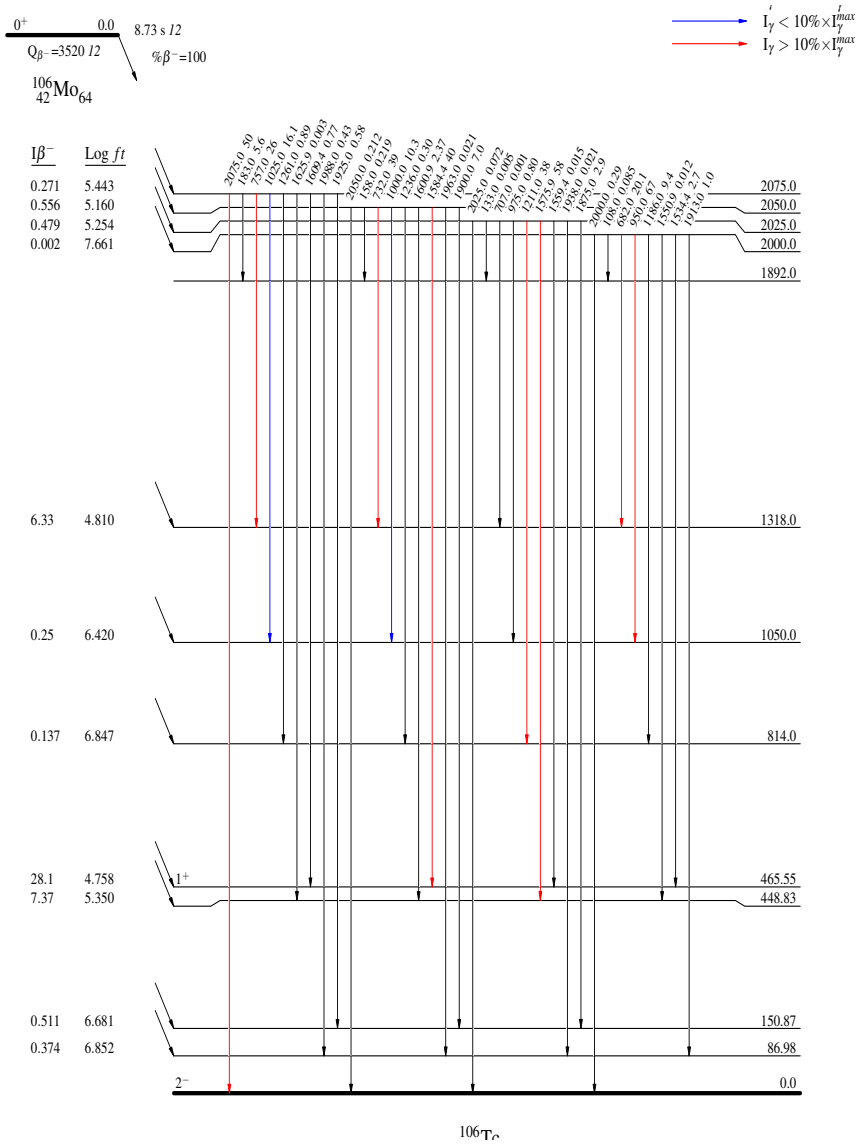

Figure 11.19: This figure shows the 10th part of the ^{106}Mo level scheme. Note that all gammas being emitted from levels are normalized to 100%.

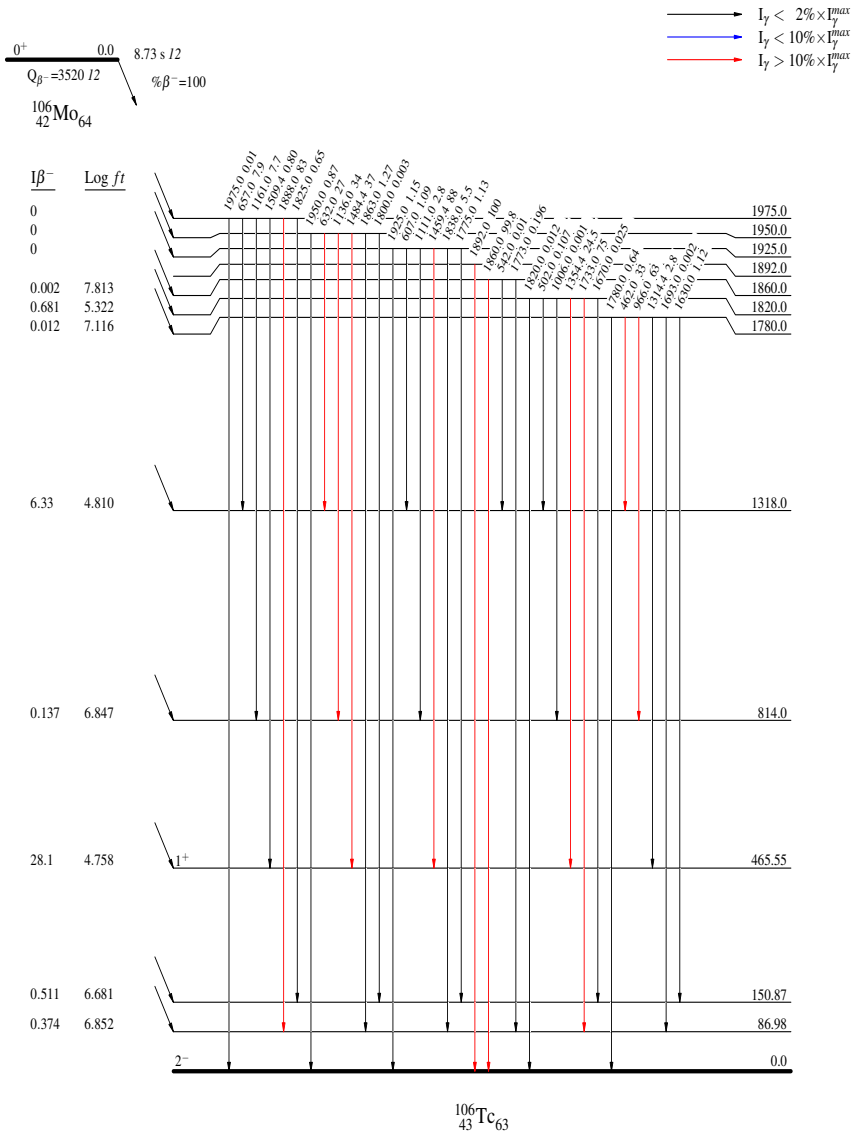

Figure 11.20: This figure shows the 11th part of the ^{106}Mo level scheme. Note that all gammas being emitted from levels are normalized to 100%.

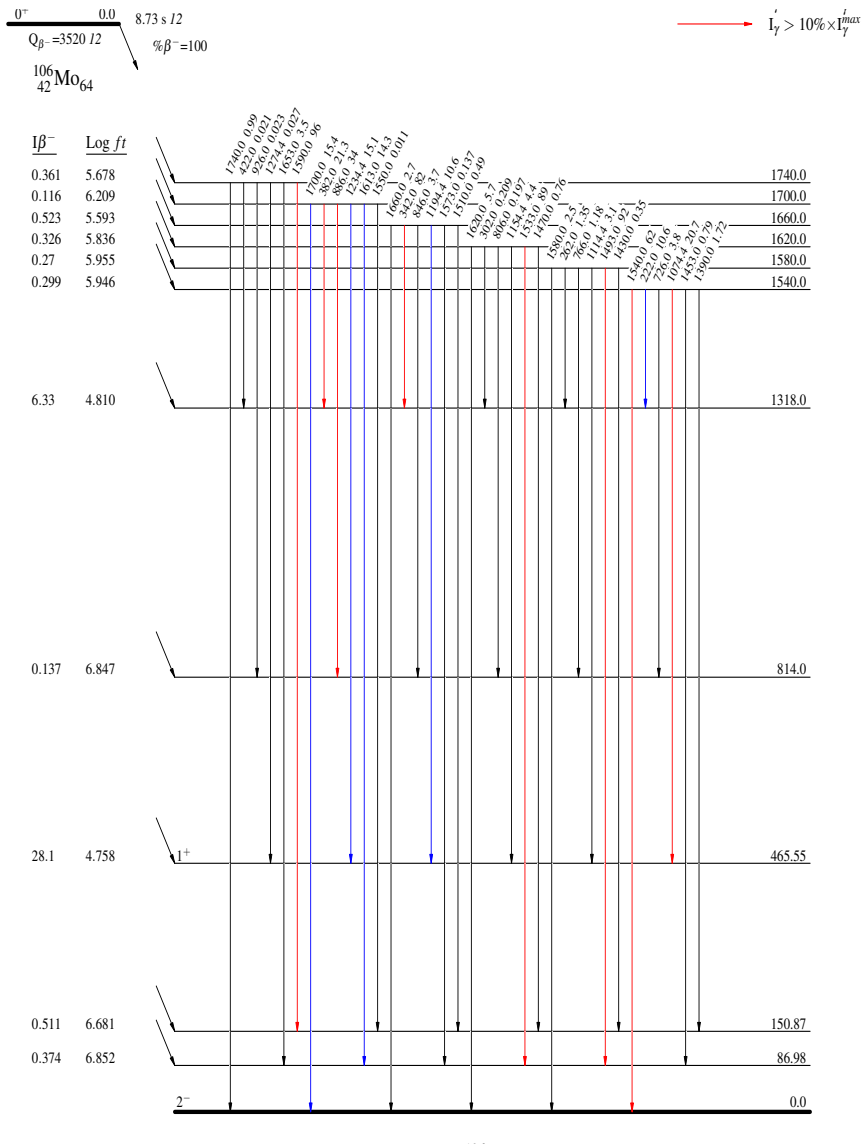

Figure 11.21: This figure shows the 12th part of the ^{106}Mo level scheme. Note that all gammas being emitted from levels are normalized to 100%.

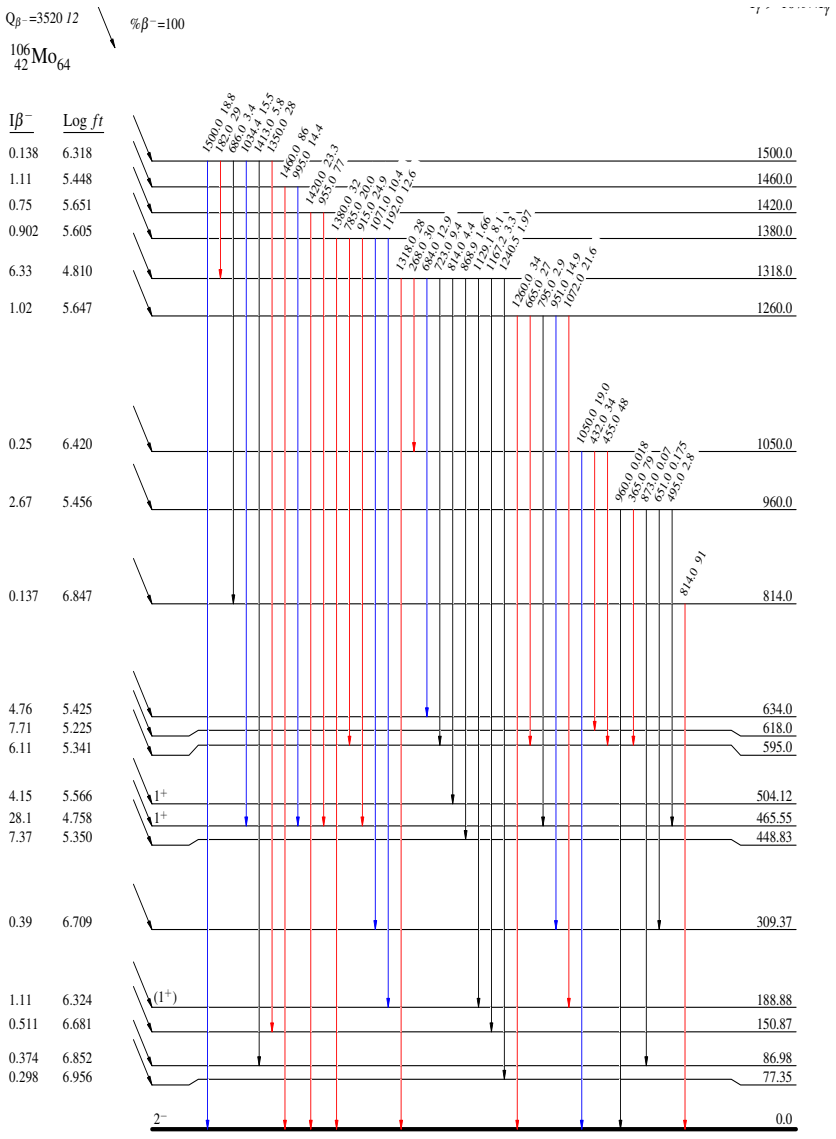

Figure 11.22: This figure shows the 13th part of the ^{106}Mo level scheme. Note that all gammas being emitted from levels are normalized to 100%.

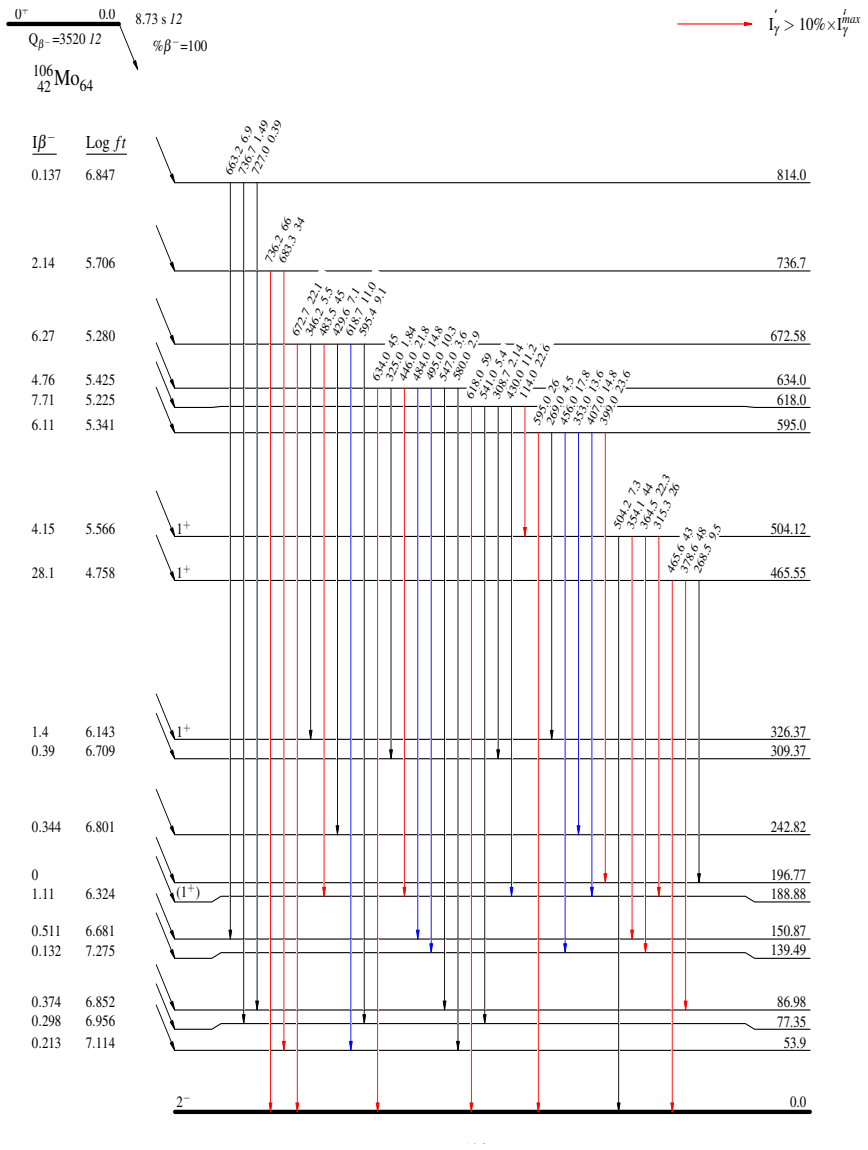

Figure 11.23: This figure shows the 14th part of the ^{106}Mo level scheme. Note that all gammas being emitted from levels are normalized to 100%.

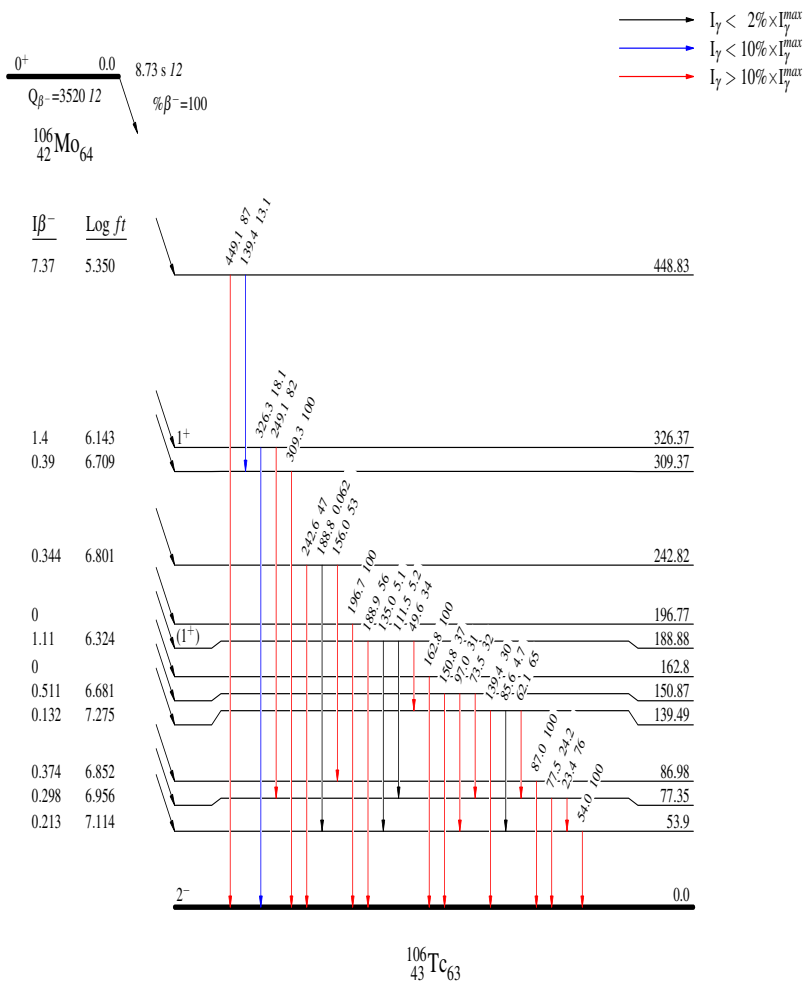

Figure 11.24: This figure shows the 15th part of the ^{106}Mo level scheme. Note that all gammas being emitted from levels are normalized to 100%.

Vita

Michael Cooper was born in Knoxville, TN to Kenneth Cooper and Lisa Cooper on November 10, 1992. As a child, Michael was always curious about science, mathematics, and computers. Of no doubt being around the area where Y-12 and ORNL are located had an effect on him, as did the fact that his father was a manager at Y-12. Michael was homeschooled as a child, and started college at Roane State Community college at age 16. Once Michael finished his homeschooling and dual enrollment at RSCC, Michael enrolled at the University of Tennessee for chemical engineering. Michael very quickly realized that he preferred nuclear engineering and physics to chemistry, and switched majors after his sophomore year. From the start at UT, Michael intended on pursuing a PhD in engineering. During his senior year of undergraduate studies, Michael discussed working on his master's degree with Dr. Steven Skutnik. Michael completed his master's degree with a thesis on hybrid k-edge densitometry modeling for nuclear safeguards. During his time completing his master's degree, Michael completed three successful internships, two at ORNL, and one at Lawrence Livermore. Michael found an interest in nuclear data from experience with nuclear engineering codes such as MCNP. Michael realized that much of the nuclear data used by MCNP is very old, and in need of newer experimental data. This lead Michael to work with Dr. Robert Grzywacz for his PhD, as Dr. Grzywacz is known for decay spectroscopy. An opportunity arose to work on the MTAS collaboration, and do analysis for ^{106}Mo and ^{106}Tc. Michael has always had a passion for nuclear defense, which only intensified after interning at LLNL. Michael is currently working at Y-12 National Security Complex as a computational nuclear engineer within the development division.